dc_242_11

DOCTORAL THESIS

HUNGARIAN ACADEMY OF SCIENCES

BLADE SWEEP APPLIED TO AXIAL FLOW FAN ROTORS OF CONTROLLED VORTEX DESIGN

János VAD

Budapest, 2011

CONTENTS

I. ACKNOWLEDGMENTS

I would like to thank my family with love – my wife Márta, my elder son Máté, my younger son Levente – for giving a helping hand during my research work and during the days of elaboration of the dissertation.

I would like to express my gratitude to Dr. Ferenc Bencze and Prof. Tamás Lajos for their support within the framework of the research projects coordinated by them, as well as for their paternal advice; to Dr. Alessandro Corsini and Prof. Franco Rispoli for their kind co-operation on behalf of the Department of Mechanics and Aeronautics, University of Rome "La Sapienza"; to Prof. Helmut Jaberg for his kind collaboration on behalf of the Institute for Hydraulic Fluid Machinery, Graz University of Technology; to Dr. Elemér Pap collaborating on behalf of the Institute for Fluid Mechanics and Thermodynamics, Otto-von-Guericke University of Magdeburg; to Dr. László Kullmann for his thorough review of the dissertation and valuable comments; and to the staff of the Department of Fluid Mechanics, Budapest University of Technology and Economics, for establishing a congenial work atmosphere.

The data of **TÁMOP** (TÁMOP-4.2.1/B-09/1/KMR-2010-0002), **OTKA** (Hungarian National Fund for Science and Research, K 83807, K 63704, T 043493, T 025361), **OM FKFP** (Ministry of Education, R&D Project of Higher Education, 0356/99), and **S&T (TéT)** (Scientific & Technological Bilateral Project, A-15/03, A-10/01, D-37/99, A-34/98, I-28/98) projects supporting the thesis work are listed in the **final Appendix**.

Budapest, September 2011

János Vad

II. ABSTRACT

The effects of forward blade sweep applied to low-speed axial flow fan rotors of controlled vortex design are discussed herein, at the design operational point, using experimental and Computational Fluid Dynamics (CFD) studies.

An analytical model has been elaborated for systematic investigation of the effects stimulating or retarding radial outward fluid migration in the rotor blade suction side boundary layer, contributing to increased near-tip loss and promoting tip stalling. Application of the model, supported by measurement data, has led to the conclusion that controlled vortex design tends to promote the outward migration and near-tip accumulation of fluid in the suction side boundary layer, resulting in increased endwall blockage. The increase in near-tip axial displacement thickness due to controlled vortex design was found approximately proportional to the spanwise gradient of designed blade circulation, for unswept blades. The purposeful use of the analytical model has led to the conclusion that forward blade sweep is especially beneficial for rotors of controlled vortex design in the *near-tip* region, in terms of moderating outward fluid migration and near-tip loss.

Literature data on diffuser flows of various levels of complexity – conical diffusers, linear as well as annular blade cascades – were post-processed and evaluated. The following common conclusion was drawn for each type of flow. For fixed inlet and outlet conditions, the consequence of decreasing the flow path length is to decrease the total pressure loss – due to moderating the effect of wall skin friction –, provided that the adverse streamwise pressure gradient remains below a subcritical value. Based on the studies by Lieblein, a method was elaborated for estimating the total pressure loss as well as its modification due to a change of flow path length in blade cascade flows. Based on a CFD study, the application of forward sweep has been judged especially beneficial to rotors of controlled vortex design in loss reduction also *away from the endwalls*. This is due to shortening of the flow paths on the blade suction side, which become elongated due to controlled vortex design in absence of forward sweep.

Supported by the aforementioned findings, a preliminary blade design method has been developed, incorporating forward sweep in controlled vortex design. Supplementing the traditional quasi-two-dimensional design technique with a quasi-three-dimensional approach, the method enables more accurate consideration and control of blade aerodynamics along the three-dimensional flow paths on the blade suction side. The design method relies on traditional two-dimensional cascade correlations. It serves with the sweep angle distribution as a *design output*, i.e. the blade stacking geometry, found beneficial from the aerodynamic point of view, is a *result* of the preliminary design process. A design case study revealed that the elaborated design method offers some potential for efficiency gain of percent order of magnitude.

III. LIST OF SYMBOLS AND ABBREVIATIONS

The units specified below for the quantities are SI units. In the thesis, data are occasionally specified in non-SI units corresponding better to industrial practice. However, all the data are to be converted to SI units for computation, unless other comments are provided.

Latin symbols

A	[*rad*]	flow angle in the core flow (Ch. 2)
A_{CL}, B_{CL}	[-]	empirical constants in estimation of C_{Lopt} (Ch. 4)
A_{s}	[m^2]	surface area (Ch. 4)
$d\underline{A}_{\mathrm{s}}$	[m^2]	surface element vector (Ch. 4)
AR	[-]	aspect ratio
a	[m/s^2]	fluid acceleration in the boundary layer (Ch. 2)
@	[m/s^2]	fluid acceleration in the core flow (Ch. 2)
C_{D}	[-]	blade section drag coefficient
C_{L}	[-]	blade section lift coefficient
C_p	[-]	static pressure coefficient (Ch. 3)
CR	[-]	Q3D-to-Q2D chord ratio (-) $= c_{\mathrm{opt\ Q3D}} / c_{\mathrm{opt\ Q2D}}$
c	[m]	blade chord length
D	[-]	Lieblein diffusion factor
D_{D}	[m]	diameter of conical diffuser (inlet, outlet) (Ch. 3)
E	[*rad*]	yaw angle of fluid in the core flow (Ch. 2)
e	[m]	streamwise tangential coordinate along relative streamline (Ch. 2)
dF	[N]	force acting on an elementary blade section (Ch. 4)
dF_{D}	[N]	drag force acting on an elementary blade section (Ch. 4)
dF_{L}	[N]	lift force acting on an elementary blade section (Ch. 4)
f_v	[m/s^2]	term manifesting the effects of Reynolds stresses (Ch. 2)
G	[Pa/m]	adverse streamwise pressure gradient averaged along the flow path (Ch. 3)
g	[$1/m$]	streamline curvature, i.e. the reciprocal value of the radius of the osculating circle related to the streamline (Ch. 2)
g_{Cor}	[m/s^2]	Coriolis force field intensity (Ch. 2)
g_p	[-]	local dimensionless streamwise pressure gradient (Ch. 3)
$\underline{h}$	[m]	derivative vector (Ch. 2)
$\underline{k}$	[m]	unit vector pointing toward the centre of osculating circle (Ch. 2)
L	[m]	flow path length (Ch. 3)
δL	[m]	increment in the streamwise length coordinate (Ch. 3)

ℓ	[m]	axial extension of diffuser (Ch. 3)
$d\underline{\ell}$	[m]	line element vector (Ch. 4)
M	[Nm]	torque applied to the rotor shaft (Ch. 4)
dM	[Nm]	torque reacting on an elementary rotor cascade (Ch. 4)
Ma	[-]	Mach number (Ch. 3)
m	[-]	power exponent in the spanwise prescribed isentropic total pressure rise distribution (Ch. 4)
N_{b}	[-]	blade count
N_{s}	[-]	number of cylindrical blade sections along the span (Ch. 4)
N	[m]	normal coordinate related to a streamline in the core flow (Ch. 2)
n	[$1/s$]	rotor speed; coordinate tangential to the cylindrical surface and normal to the blade section (Ch. 2)
P	[Pa]	static pressure in the core flow (Ch. 2)
dP	[W]	mechanical power input to the annular elementary cascade (Ch. 4)
p	[Pa]	static pressure; static pressure in the boundary layer (Ch. 2)
Δp	[Pa]	mass-averaged static pressure rise (Ch. 3)
Δp_{t}	[Pa]	pitchwise mass-averaged total pressure rise (Ch. 3)
$\overline{\Delta p_{\mathrm{t}}}$	[Pa]	annulus mass-averaged total pressure rise (Ch. 4)
$\Delta p_{\mathrm{t\,is}}$	[Pa]	$= \rho \hat{v}_{u2} u_2$ pitchwise mass-averaged isentropic total pressure rise, assuming swirl-free inlet (Ch. 3)
$\overline{\Delta p_{\mathrm{t\,is}}}$	[Pa]	annulus mass-averaged isentropic total pressure rise (Ch. 4)
$\Delta p'_{\mathrm{t}}$	[Pa]	mass-averaged total pressure loss (Ch. 3)
q_m	[kg/s]	mass flow rate (Ch. 4)
q_{V}	[m^3/s]	volume flow rate (Ch. 4)
R	[-]	$= r/r_{\mathrm{t}}$ dimensionless radius
ΔR	[-]	change in dimensionless radius in Q3D rotor approach (Ch. 4)
R_α	[m]	radius of curvature of projection of streamline onto the [n, s] plane (Ch. 2)
R_{C}	[m]	camber line radius (Ch. 2)
r_{c}	[-]	correlation index (Ch. 3)
Re	[-]	$= \mathrm{Re}_c = c\, w_\infty / \nu$ Reynolds number based on blade chord (Ch. 2, Ch. 3)
Re_L	[-]	Reynolds number based on true flow path length L (Ch. 3)
r	[m]	radius of rotor blade section; radial coordinate; spanwise coordinate for 2D flow (Ch. 4)
S	[m]	span. For an axial flow turbomachinery blade, $S = r_{\mathrm{t}} - r_{\mathrm{h}}$

S_δ slope of endwall blockage function wrt. various parameters at tip (D, γ, c/s_b) (Ch. 2)

$S_{\delta\,\mathrm{CVD}}$ [-] Slope of endwall blockage function with respect to $d\hat{\psi}_{2,\mathrm{D}}/dR$ (Ch. 2)

s [m] coordinate along the projection of streamline to the cylindrical surface (Ch. 2)

s_b [m] $= 2r\pi/N_b$ blade spacing (blade pitch)

ds_b [m] increment in pitchwise coordinate (Ch. 4)

t [rad] polar angle coordinate (Ch. 2)

u [m/s] $= 2r\pi n$ circumferential velocity

$\underline{u}$ [m] unit vector of length coordinate (Ch. 2, Ch. 4)

V [m/s] absolute velocity in the core flow (Ch. 2)

v [m/s] flow velocity in the absolute frame of reference; absolute velocity in the boundary layer (Ch. 2)

W [m/s] relative velocity in the core flow (Ch. 2)

w [m/s] relative velocity; relative velocity in the boundary layer (Ch. 2)

Δw [m/s] change in relative velocity through the cascade (Ch. 4)

X [-] fraction of axial chord (axial distance from the blade leading edge divided by axial projection of chord)

z [m] axial coordinate

Greek symbols

α [rad] local flow angle in the boundary layer, measured from axial direction (Ch. 2)

α_1 [rad] cascade inlet flow angle, measured from axial direction

α_2 [rad] cascade outlet flow angle, measured from axial direction

α_∞ [rad] free-stream (mean) flow angle, measured from axial direction (Ch. 3, Ch. 4)

β [rad] cone half-angle of elementary conical cascade in Q3D approach (Ch. 4)

Γ [m^2/s] blade circulation

γ [rad] stagger angle, measured at a cylindrical section from axial direction; local blade metal angle, measured from axial direction (Ch. 2). The mean representative value for the local blade metal angle is the stagger angle.

δ [rad] characteristic angle: tan $\delta = C_D/C_L$ (Ch. 4)

δ_x^* [m] axial displacement thickness

$\Delta\left(\delta_x^*/\tau\right)_{\mathrm{CVD}}$ [-] endwall blockage component related to $d\hat{\psi}_{2,\mathrm{D}}/dR$ (Ch. 2)

ε [rad] yaw angle of flow in the boundary layer (Ch. 2)

ε_L [rad] yaw angle related to a SS limiting streamline (Ch. 4)

$\tilde{\varepsilon}_{L}$ [*rad*] mean value of yaw angle along a SS limiting streamline (Ch. 4)

ζ [-] relative kinetic energy defect coefficient (Ch. 2)

η_{D} [-] diffuser efficiency (Ch. 3)

$\eta_{D\,end}$ [-] efficiency of end-diffuser (Ch. 3)

η_{t} [-] local total efficiency (Ch. 3, Ch. 4)

$\overline{\eta}_{t}$ [-] global total efficiency (Ch. 4)

ϑ [*rad*] diffuser cone half-angle (Ch. 3)

θ [*rad*] camber angle

θ^{*} [*m*] wake momentum thickness (Ch. 3)

κ [*rad*] dihedral angle (Ch. 4)

λ [*rad*] sweep angle. See the Terminology section for definition and sign convention.

λ* [*rad*] auxiliary angle (Ch. 4)

μ [1/*m*] radial migration parameter, i.e. increment of *s*–wise derivative of tangent of yaw angle of flow in the boundary layer (Ch. 2)

μ^{*} [-] $= \mu \cdot c$ dimensionless radial migration parameter (Ch. 2)

ν [m^2/s] kinematical viscosity

ν_{ht} [-] $= r_h / r_t$ hub-to-tip ratio

ξ [*m*] a specific value of the pitchwise coordinate (Ch. 4)

ρ [kg/m^3] fluid density

σ [-] $= c / s_b$ solidity

τ [*m*] tip clearance

$\underline{\tau}$ [*Pa*] shear stress (Ch. 4)

Φ [-] global flow coefficient (annulus area-averaged axial velocity divided by u_t)

$\hat{\varphi}$ [-] $= \hat{v}_z / u_t$ pitch-averaged axial flow coefficient

Ψ [-] global total pressure coefficient (annulus mass-averaged total pressure rise divided by $\rho\, u_t^2/2$)

$\hat{\psi}_2$ [-] $= \Delta p_{t\,is} / \left(\rho u_t^2/2\right) = \rho \hat{v}_{u2} u_2 / \left(\rho u_t^2/2\right) = 2R_2\, \hat{v}_{u2}/u_t$ pitch-averaged isentropic total pressure coefficient (also termed as outlet swirl coefficient for swirl-free inlet)

ω [*rad/s*] blade rotational (angular) speed

ϖ [-] mass-averaged total pressure loss coefficient (Ch. 3)

ϖ_{loc} [-] local total pressure loss coefficient (Ch. 3)

Subscripts and Superscripts

BSW backward-swept

cp centripetal (Ch. 2)

crit critical value (Ch. 3)

CVD related to the spanwise gradient of blade circulation, represented by $d\hat{\psi}_{2,\mathrm{D}}/dR$, due to controlled vortex design (Ch. 2)

D design; at the design flow rate

EWB at the edge of endwall blockage (Ch. 2)

e streamwise component in relative flow (Ch. 2)

FSW forward-swept

h hub

is isentropic

LE blade leading edge (Ch. 4)

mid relevant at midspan (mid-radius) (Ch. 3)

min minimum value (Ch. 3)

n,s local coordinates (Ch. 2)

opt optimum value (Ch. 3, Ch. 4)

P characteristics related to the investigated point P located in the boundary layer (Ch. 2)

RS radial blade stacking

r,t,z coordinates in the cylindrical coordinate system; *z*: axial coordinate (Ch. 2)

x,y,z Cartesian coordinates; *z*: axial coordinate (Ch. 2)

TE blade trailing edge (Ch. 4)

t blade tip

u tangential, circumferential coordinate; tangential component (of velocity); pitchwise coordinate for 2D flow (Ch. 4)

1 inlet (of rotor; used also for diffuser in Ch. 3); point located at rotor inlet (Ch. 4)

2 exit (of rotor; used also for diffuser in Ch. 3); point located at rotor outlet (Ch. 4)

12 inlet-to-outlet mean value

I, II two neighbouring surfaces of different spanwise location (Ch. 4)

^ pitchwise-averaged value (Appendix J)

' first derivative (Ch. 2)

' turbulent velocity fluctuation (appears with *w*) (Ch. 2)

" second derivative (Ch. 2)

— temporal mean value (of characteristics having turbulent fluctuations) (Ch. 2)

$\bar{}$ annular mass-averaged value, global value

∞ free-stream (mean) characteristics

Abbreviations

CFD	computational fluid dynamics
CVD	controlled vortex design
2D	two-dimensional
3D	three-dimensional
FSW	forward sweep, forward swept
LDA	laser Doppler anemometry
Q1D	quasi-one-dimensional
Q2D	quasi-two-dimensional
Q3D	quasi-three-dimensional
R&D	research and development
USW	unswept

IV. TERMINOLOGY

This section explains the terms used in the thesis, in alphabetical order. **Figure IV.1** represents each case of blade →*stacking* discussed herein.

Aerodynamic performance: the product of total pressure rise and volume flow rate through the blade cascade.

Annulus: the space bounded by the rotor →*hub* and →*casing*.

Aspect ratio, AR = $S/c_{\mathrm{b\ mid}}$: the ratio between the →*span* and the →*chord* length at midspan.

Backward skew: a version of →*skew (circumferential skew)*, incorporating →*backward sweep*, for which shifting of datum blade sections occurs against the direction of rotation.

Backward sweep: a version of →*sweep* for which shifting of datum blade sections occurs in such a way that a blade section under consideration is downstream of the neighbouring blade section at lower radius. A portion of an airfoil or a wing with one endwall is considered herein to be swept backward if a section under consideration is downstream of the neighbouring section that is closer to the endwall.

Blade circulation, Γ: the integral of relative velocity along a closed curve surrounding an elementary blade section at a given radius. The curve incorporates two periodic lines of pitchwise separation of s_{b} through the blade passage, as well as two pitchwise-directed lines of length of blade spacing s_{b}. For swirl-free inlet, the blade circulation can be expressed as ($s\,\hat{v}_{2u}$). Substituting $s_{\mathrm{b}} = 2r\pi/N_{\mathrm{b}} = u/(nN_{\mathrm{b}})$, it can be pointed out that the blade circulation is proportional to $\hat{\psi}_2$.

Blade correction: the procedure for retaining the blade →*load* and →*aerodynamic performance* of the →*straight* datum *blade* sections that are modified due to →*non-radial stacking*. The blade correction can be carried out by means of modifying the geometry – shape, size – of the blade sections and/or by altering the →*stagger angle*.

Camber angle, θ: the central angle related to a →*camber line* of circular arc shape.

Camber line: The contour curve (profile) of a blade section is considered that fits to a cylinder that is coaxial with the axis of rotation. The camber line is the line joining the centres of the circles enveloped by the contour curve. This reads that the camber line is the mean line (between pressure and suction surfaces) of the blade profile [**1**].

Cascade: a row of consecutive airfoils (linear cascade) or rotor blades (annular cascade).

Casing: the cylindrical duct enclosing the rotor.

Characteristic curve: the diagram representing the total pressure rise achieved by the turbomachine as a function of volume flow rate.

Chord, c: the straight line joining the endpoints of the →*camber line*. The length of the chord c is approximately equal to the linear distance between the leading edge and the trailing edge [**1**].

Circulation, Γ: the line integral of velocity over a closed curve surrounding an object (e.g. the elementary section of an airfoil, a blade, or a wing). See →*blade circulation*.

Continuity law: the law of conservation of fluid mass.

Controlled vortex design: a →*vortex design* concept prescribing spanwise increasing →*blade circulation*, and accordingly, spanwise increasing →*Euler work* and →*isentropic total pressure rise*, along the dominant part of the →*span*.

Diffusion: fluid deceleration through the blade passage.

Dihedral (also termed "lean"): a →*non-radial stacking* technique for which the cylindrical sections of a →*straight* datum *blade* are shifted normal to the blade chord.

Dihedral angle, κ: κ is the local angle between i) the radial direction and ii) the projection of the →*stacking line* to the plane determined by the radial direction and the direction normal to the chordline.

Elementary cascade: the series of blade sections within a →*cascade* that extend to a small fraction of span only. This fraction can be infinitesimally small, *dr*, in theoretical discussion.

Endwall: either of the annulus walls, i.e. either the hub wall or the casing (or shroud) wall.

Endwall blockage: attenuation of through-flow and blade working capability near the →*endwall.*

Euler work: the specific work done by the blading [*J/kg*]: the →*isentropic total pressure rise* divided by the fluid density: ($\hat{v}_{u2} u_2$) (expressed on the basis of the Euler equation for turbomachines, for swirl-free inlet).

Forward skew: a version of →*skew (circumferential skew)*, incorporating →*forward sweep*, for which shifting of datum blade sections occurs in the direction of rotation.

Forward sweep: a version of →*sweep* for which shifting of datum turbomachinery blade sections occurs in such a way that a blade section under consideration is upstream of the neighbouring blade section at lower radius. A portion of an airfoil or a wing with one endwall is considered herein to be swept forward if a section under consideration is upstream of the neighbouring section that is closer to the endwall.

Free vortex design: a →*vortex design* concept prescribing spanwise constant →*blade circulation*, and accordingly, constant →*Euler work* and →*isentropic total pressure rise*, along the →*span*.

Free vortex operation: an operational state in which (nearly) constant →*blade circulation* is realised along the →*span*, either due to the →*free vortex design* concept at the design flow rate or due to the off-design operation of a rotor of →*controlled vortex design*.

Hub (root): the innermost section of the blade [**1**], as well as the inner part of the rotor onto which the blades are mounted.

Hub-to-tip ratio: The ratio of the →*hub* radius to the →*tip* radius.

Isentropic process: an ideal process at which the entropy is constant. Since heat transfer is neglected herein, the term "isentropic" can be used as a synonym of "inviscid".

Isentropic total pressure rise: see the List of Symbols for $\Delta p_{\mathrm{t\,is}}$ (expressed on the basis of the Euler equation for turbomachines, for swirl-free inlet).

Isolated rotor: a rotor without guide vanes.

Leading edge: the front, or nose, of the blade [**1**].

Lean: see →*dihedral*.

Lift-to-drag ratio: the ratio C_L/C_D for a blade section.

Load (of blading): the measure of utilization of lifting capacity of blade sections, quantified herein by the lift coefficient C_L.

Negative dihedral: a version of →*dihedral* near the →*endwall* when the endwall makes an acute angle with the blade suction surface.

Negative sweep: a version of →*sweep* near the →*endwall* when a blade section under consideration is downstream of the adjacent inboard section.

Non-free vortex operation: an operational state in which changing →*blade circulation* is realised along the →*span*, either due to the →*controlled vortex design* concept at the design flow rate or due to the off-design operation of a rotor of →*free vortex design*.

Non-radial stacking: the realisation of blading of non-radially directed →*stacking line*.

Part load operational range: the operational range including flow rates lower than the design flow rate.

Pitch (of blading, blade pitch): see →*spacing*.

Positive dihedral: a version of →*dihedral* near the →*endwall* when the endwall makes an obtuse angle with the blade →suction surface.

Positive sweep: a version of →*sweep* near the →*endwall* when a blade section under consideration is upstream of the adjacent inboard section.

Pressure surface (side): The concave surface of the blade. Along this surface, pressures are highest [**1**].

Radial stacking: the realisation of →*straight blades* ("radially stacked blades").

Skew, circumferential skew: a special combination of →*sweep* and →*dihedral*, for which the sections of the →*straight* datum rotor *blade* are shifted in the circumferential direction.

Solidity, σ: the ratio of the →*chord* length to the →*spacing*.

Spacing, s_b (of blading), blade pitch: the distance in the direction of rotation between corresponding points on adjacent blades [**1**].

Span, S (of blading), blade height: the extension of the blade in the radial direction from hub to tip. See the List of Symbols for *S*. The span of an airfoil or a wing is considered herein as its projection normal to the incident relative flow.

Stacking (of blading): the manner of definition of blade →*stacking line* geometry.

Stacking line (of the blade of an axial flow turbomachine): the line joining the centres of gravity of the blade sections fitting to cylinders that are coaxial with the axis of rotation.

Stagger angle, γ: the angle between the →*chord* and the axial direction.

Stall: extensive flow separation occurring in the blade passages, resulting in breakdown – i.e. positive slope – of the →*characteristic curve* in the →*part load operational range*. The onset of stall is indicated by the point of → *stall margin*.

Stall margin: the point of the →*characteristic curve* where the peak value of total pressure rise occurs.

Straight blade, *blade of* →radial stacking: a blade realized with radially directed straight →*stacking line*.

Suction surface (side): The convex surface of the blade. Along this surface, pressures are lowest [**1**].

Sweep: a →*non-radial stacking* technique for which the cylindrical sections of a →*straight* datum *blade* are shifted parallel to the blade chord.

Sweep angle, λ: in the case of →*sweep* only, λ is the local angle between the →*stacking line* and the radial direction. In the case of a combination of →*sweep* and →*dihedral*, e.g. in circumferential →*forward skew*, λ is the local angle between i) the radial direction and ii) the projection of the →*stacking line* to the plane determined by the chordline and the radial direction. The sign convention for λ is in accordance with [**2**], i.e. $\lambda_{FSW} < 0$; $\lambda_{BSW} > 0$: see Fig. IV.1.

Throw: the throw of a jet produced by a jet fan is defined as the distance at which the peak jet velocity has fallen to 0.5 *m/s* [**3**].

Tip: the outermost section of the blade [**1**].

Trailing edge: the rear, or tail, of the blade [**1**].

Twist: a characteristic blade shape due to spanwise changing →*stagger angle* ("stagger gradient").

Vortex design: the manner of prescribing the →*blade circulation* distribution along the →*span*.

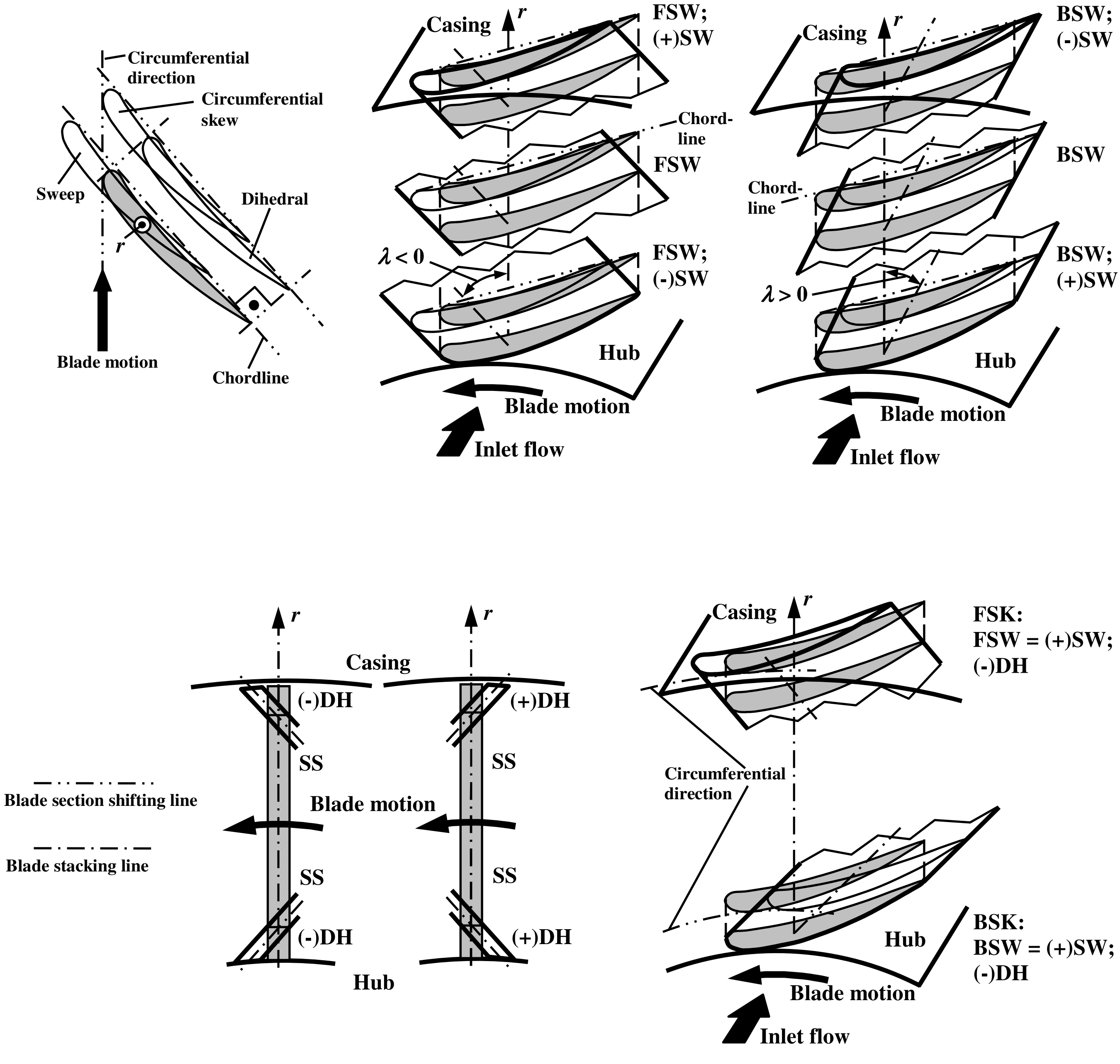

Figure IV.1 **[4].** *Representation of blade sweep, dihedral, and circumferential skew, on selected blade portions. Comments:* ***A)*** *Grey profiles: sections of a straight datum blading.* ***B)*** *Untwisted blades of spanwise constant blade sectional geometry are presented for simplicity and clarity.* ***C)*** *Abbreviations and symbols: FSW–forward sweep, BSW–backward sweep, (+)SW–positive sweep, (-)SW–negative sweep, FSK–forward skew, BSK–backward skew, (+)DH–positive dihedral, (-)DH–negative dihedral, r–radial coordinate*

1. INTRODUCTION AND OBJECTIVES

1.1. Axial flow fans vs. compressors

In recent decades, extreme computational and measurement technical efforts have been sacrificed to the aerodynamic design and optimisation of axial flow rotating blade rows operating in power generation as well as in civil and military aviation, with special regard to the multistage environment. Extensive knowledge has been gathered in these areas from the perspective of aerodynamics as well as design and optimisation methodology. However, there appears to have been some failure in transferring this knowledge to the field of axial flow fans used in building services engineering, industrial ventilation, and other air technical applications such as automotive engine cooling, although such fans also have a significant economical impact, given that they operate in an extremely large number in everyday use. Some of the possible reasons for such failure are given below. From this point onwards, the comparative discussion is confined to low-speed fans vs. low-speed compressors.

- *Absorbed power; design; research and development.* The absorbed power is usually orders of magnitudes lower for ventilating fans than for compressors. This appears to limit the amount invested in design as well as research and development (**R&D**) aimed at improving the aerodynamic efficiency of fans. An algorithmized, multi-objective design and optimization process applied to multistage compressors relies on expensive, high-power computational resources. In contrast, the single fan stage is often intended to be designed by simple means.
- *Layout.* Fans often operate as single-stage turbomachinery, and as isolated rotors in many applications. Their blade count is relatively low. Their hub-to-tip ratio is usually also moderate; the hub diameter, at least in direct-driven fans, is often set by the size of the incorporated electric motor. Simplified blade geometry is often applied to fans, e.g. plate blades, or moderately twisted blades.
- *Operation.* The rotor speed of fans is moderate, according to the features of the fan drive as well as to acoustical and/or mechanical limitations.

In order to contribute to moderating the above-mentioned deficiency of knowledge transfer, the compressor- and fan-related literature is overviewed and processed in a concerted manner.

1.2. Axial flow turbomachines: blade stacking

While classic axial flow turbomachines tended to incorporate radially stacked, straight blades, non-radial stacking techniques applied to axial flow blading – referring to Fig. IV.1 – have become widespread in recent decades. The concept of sweep was originally developed and investigated for wings applied in aeronautics, e.g. [**5**]. Various non-radial stacking styles such as blade sweep and skew are widely applied to axial flow turbomachines in cooling, climate control, and industrial air technology (fans, compressors) [**6-16**]. A comprehensive overview is given in [**4, 8, 17**] on non-radial stacking as a potentially useful supplement to blade improvement achievable with radial stacking techniques. Non-radial blade stacking offers increased capability for reduction of near-endwall and tip clearance losses as well as control of secondary flows and radial migration of high-loss fluid. On this basis, non-radial stacking has successfully been applied for improvement of aerodynamic performance and total efficiency in several cases, e.g. [**8, 17-29**]. The intention to investigate the applicability of non-radial stacking is strengthened by the fact that percents of gain in efficiency can be achieved by appropriate blade stacking, but the machine may suffer from efficiency deterioration in the same order of magnitude if the blade stacking is not favourable [**4**].

Simultaneous with the possible aerodynamic benefits, non-radial stacking provides a unique means for rotor noise reduction as well [**16, 21, 30-39**]. Although non-radial stacking raises rotor blade mechanical problems, especially at high speeds, such difficulties can be eliminated by use of appropriate blade materials [**35, 40**].

Non-radial stacking is usually confined to only a portion of span – e.g. to the near-endwall regions – in the case of compressor blades [**13-14, 16-17, 19, 22-24, 27-29**], for mechanical reasons, and may even be confined to the leading/trailing edge; but can be extended even to the entire span for ventilating fans [**7, 9-11, 18, 21, 25-26, 30-31, 37-38, 41-43**]. When applying circumferential skew to fans, the axial extension of the straight datum blading can be retained, the blade mechanics are expected to be more favourable than in the case of sweep alone, and the aerodynamic benefits, due to the incorporated blade sweep, can be utilised.

The discussion in the thesis

- will be confined to axial flow rotors of enthalpy-increasing, gas-handling turbomachinery,
- will consider an isolated rotor (rotor-only configuration), or a rotor without an inlet guide vane but followed by an outlet guide vane stator – accordingly, swirl-free inflow will be considered,
- will presume incompressible flow.

The above imply that ducted air technical (cooling, ventilating, etc.) fan rotors as well as rotors in blower and compressor stages of moderate pressure ratio will be herein under discussion. Fluid temperature change, heat transfer and gravity effects will be neglected.

The literature reflects a consensus that forward sweep (**FSW**) and forward skew offer the following possible benefits in the part load operational range: improvement of aerodynamic performance and total efficiency, increase of total pressure peak, and extension of stall-free operating range by shifting the stall margin toward lower flow rates [**8, 18, 21, 23-29, 31, 38, 44-47**]. Such advantageous effects are usually dedicated to the control of radially outward migration and near-tip accumulation of high-loss fluid in the suction side boundary layer. However, the research results are rather diversified from the perspective of performance- and loss-modifying effects due to FSW / forward skew near the design flow rate. In [**17**], it was pointed out that FSW near the tip – resulting in positive sweep – enables the reduction of near-tip losses. In contrast, no significant tip clearance loss reduction was observed for positive sweep in one of the case studies in [**8**], and the blade of negative sweep showed the best overall performance. Positive sweep was considered in [**17**] as a means of loss reduction, and this effect resulted in local gain of efficiency in the bladings of spanwise constant sweep in [**48**]. The "swept-back" blades proposed in [**49**], exhibiting efficiency gain due to loss reduction along the entire span, appear to incorporate positive sweep as well as positive dihedral at both endwalls. It is suggested by [**18, 21, 25-26, 38**] that FSW along the entire span is beneficial for loss reduction as well as performance and efficiency improvement. Based on [**19**], application of near-tip FSW can be recommended for efficiency improvement over the dominant part of the operational range, including the design point. FSW near the tip in [**28-29**] and forward skew in [**49-50**] resulted in efficiency and/or performance gain. Nevertheless, nearly unchanged efficiency was observed in [**21, 38**] when FSW was introduced to obtain the model fan AV30N. Furthermore, near-tip FSW reported in [**23, 27**] and forward skew in [**37, 50**] caused efficiency and performance deterioration. In [**45-46, 51**], efficiency deterioration was experienced for an FSW rotor over the dominant part of the stall-free operational range. Backward sweep was found to be optimal in [**52-53**] for efficiency gain. On the basis of [**54-56**], one may assume that non-radial stacking causes no reduction but spanwise redistribution of losses. The contradictory experiences outlined above appear to be in accordance with the comment in [**24**] that it is impossible to generalise how FSW (and similarly, circumferential forward skew) impacts performance for all blading types. This suggests that the aerodynamic impact of non-radial stacking on the three-dimensional (**3D**) blade passage flow, blade load, and loss is not yet fully explored.

1.3. Vortex design methods

Rotors of axial flow turbomachines are often of controlled vortex design (**CVD**) [**8**]. This means that in contrast to the classic free vortex design concept prescribing spanwise constant design blade circulation, the prescribed circulation – and thus, the Euler work as well as the isentropic total pressure rise – increases along the dominant part of the blade span in a prescribed manner, as e.g. in [**1, 26, 57, 72, 86, 95**]. As discussed in [**68, 139**], CVD offers the following potential benefits:

- CVD guarantees a better utilisation of blade sections at higher radii, i.e. it increases their contribution to the rotor performance. By this means, rotors of high specific performance can be realised, i.e. relatively high flow rate and/or total pressure rise can be obtained even with moderate diameter, blade count, and rotor speed [**3, 26, 58**].

- CVD gives a means for reduction of hub losses by unloading the blade root [**37**]. As Lakshminarayana commented on the CVD method versus the classic free vortex design concept in [**1**], from the point of view of loss reduction: „The myth that the free-vortex blading has the lowest losses has been replaced by a more systematic optimization (…)".
- CVD offers a means for improving static efficiency by reducing the hub diameter, and thus moderating the outlet loss [**59, 79**].
- CVD serves as a conceptual basis for obtainment of fan bladings of simple, easy-to-manufacture geometry, as e.g. in [**58-64**] – even with spanwise (nearly) constant stagger angle (avoiding highly twisted blades [**1**]) and/or chord length. The circumferential overlap of the blades can be avoided using CVD. This enables the application of low-cost casting or injection moulding techniques for rotors incorporating the rotor hub as well as the blades.
- In multistage machinery, CVD provides a useful strategy for realising a rotor exit flow angle distribution that is appropriate for inlet to the consecutive stage [**8**].
- By prescribing spanwise increasing blade circulation along the dominant portion of blade span, but moderating the blade circulation near the rotor blade tip, the outlet swirl can be moderated near the circumference. Thus, the stability and coherence of the air jet generated by jet fans designed using CVD can be improved [**65**].
- CVD offers a means for purposeful tuning the spanwise distribution of outlet flow rate, i.e. for customizing the outlet axial velocity profile. By such means, the axial flow fan can be aerodynamically customized to the particular equipment that it will serve. This fact can be utilised in industrial air technology, e.g. in the design of fans of long "throw" [**3**] applied (e.g.) in fog cannons [**66-67**] used e.g. for dust settling. Such fans must "throw" water spray emitted from an annular nozzle located at the circumference of the fan outlet. Therefore, it is of preliminary interest to produce high outlet axial velocity near the circumference, whereas the airflow at lower radii is less utilized [**68**]. As further example, for electric motor cooling fans, the cooling airflow should intensify at higher radii, given that the cooling ribs are located at the periphery of the electric motor, whereas realization of flow rate at lower radii is of secondary importance [**69**].

Beside the above-discussed advantages offered by CVD, the design difficulties and potential disadvantages related to spanwise changing blade circulation must be acknowledged. An unavoidable consequence of spanwise blade circulation gradient is that vortices are shed from the blade trailing edge [**1**]. Associated with the shed vortices, a characteristic 3D flow pattern fills the entire blade passage, manifesting itself in radially outward and inward flow on the suction side and on the pressure side, respectively. This "non-free vortex" nature of flow has been described in detail, e.g. in [**70-71**]. The stream sheet twisting associated with the 3D interblade flow makes the applicability of two-dimensional (**2D**) airfoil or cascade theory doubtful in preliminary blade design. CVD concepts based on 2D airfoil or cascade data are compelled to neglect the pitchwise variation of radial velocity [**72**], although such design simplification does not undermine the success of the design in certain cases [**74**].

1.4. Precedents

This thesis work aims at contributing to a more comprehensive understanding of aerodynamic effects described in the previous sections, as a continuation of axial flow fan R&D related in recent decades to the Department of Fluid Mechanics – termed herein **Department** –, Budapest University of Technology and Economics. The following section gives a brief literature overview of the most relevant historical precedents in Hungary from the viewpoint of the scope of the thesis, i.e. spanwise changing rotor blade circulation, and CVD.

Dating back to the middle of the last century, the spanwise change of total pressure rise was considered in the characteristic curve calculation already in the thesis work by Gruber [**75**]. The CVD concept dates back to the middle of the last century in the international literature, e.g. [**76-78**]. The starting point of systematic application of the CVD method in Hungary is dedicated to the activity by Somlyódy [**59, 79-81**]. In [**59**], referring to [**80**], a CVD method was proposed relying on a power function blade circulation distribution along the span. The 3D rotor flow related to non-free vortex operation was modelled by Nath in [**82-83**]. Bencze and Szlivka report in [**84**] on a CVD technique incorporating a spanwise blade circulation distribution expressed as the difference between two power functions. The applicability of the CVD methodology was tested experimentally in [**85-86**]. The design and operational experiences related to axial fans were summarised by Gruber and his departmental co-authors [**87**]. The gathered background knowledge has been expanded to mixed flow fans by Vajna [**88**]. In design, applications, R&D, and education related to turbomachinery, work represented by Czibere, Fáy, Fűzy, Kovács, Kullmann, and Nyíri, as well as by their co-workers, is additionally acknowledged herein, e.g. [**177, 192-195**].

Based on the CVD methodology elaborated at the Department, several axial fan types were designed and a large number of fans were manufactured for domestic applications as well as for exportation. These fans covered a wide range of application areas, such as especially silent industrial and building service engineering fans; roof ventilation units; single-stage reversible subway ventilation fans; flue gas extractor units; two-stage, swirl-controlled boiler combustion air fans for power plants; fan units for industrial chilling technology (e.g. for deep-freezing tunnels); counter-rotating fans; ventilating fans for mobile condensers; crop and forage drying equipments; fans for chemical industry applications.

Adopting the technique of laser Doppler anemometry (**LDA**) to turbomachinery, the author contributed to the departmental R&D programme by investigating the 3D flow field developing in axial flow fans of CVD, within the framework of his Ph.D. project [**89-91**] supervised by Bencze.

Previous departmental R&D activity on axial fans of CVD has had an effect up to now in practical applications in Hungary, e.g. in agricultural engineering. In this field, publications have been elaborated at Szent István University [**64, 92**].

At the Department, the author and the team supervised by him gathered experience in design, measurement, R&D, and expert activity related to fan rotors of non-radial stacking and/or CVD. **Figure 1.1** presents some examples on the fans designed by the author within a basic research project [**94-95**], designed under his supervision [**96**], and investigated by him and his team experimentally for industrial customers. The manufacturers/vendors of the latter fan group are non-disclosed herein for confidentiality reasons. However, representative photos for such fan types are available in [**97-100**]. **Figure 1.2** shows realized axial fans of CVD designed by the author for industrial firms and end-users in Hungary [**69, 99, 101-103**].

1.5. Objectives of the thesis work

Non-radial blade stacking and CVD often characterise the axial flow blade rows simultaneously in practical applications (see Figs. 1.1 and 1.2 for illustration). Some examples are as follows: low-pressure cooling and industrial ventilating fans [**18, 21, 37-38, 50, 74, 104**], automotive cooling fans [**6-7, 9-12, 15**], high-pressure industrial fans [**25-26**], low-speed compressors [**19, 43**]. The interpretation of effects of non-radial stacking applied to CVD rotors is challenging. Due to the formerly outlined 3D nature of blade passage flow in rotors of CVD, the exploration and aerodynamic judgment of 3D effects due to sweep and skew is especially complicated in the case of CVD bladings.

The objectives of the thesis are to: i) extend the knowledge published in the literature on the aerodynamic effects due to blade sweep and skew applied to axial fans; ii) achieve a more comprehensive understanding of fluid mechanical impact of sweep and skew applied to axial fan bladings of CVD; iii) contribute to guidelines for the improvement of preliminary blade design methods, on the basis of the above. Accordingly, the design operating point is under discussion. Off-design behaviour is out of the scope of the thesis.

The classical publications related to turbomachinery design, e.g. [**57, 72, 87, 105-110**], aim at providing theoretical and/or empirical relationships for approximate quantification of airfoil, blade cascade or rotor performance and losses, as an aid to preliminary rotor blade design disregarding non-radial stacking effects. For consideration of aerodynamic phenomena related to non-radial blade stacking, several publications propose quantitative empirical relationships in specific applications, e.g. [**21, 28, 74**], or provide approximate formulae with neglect of certain effects such as viscosity [**2, 13**] or wall proximity [**104, 111-112**]. The practical applicability of such approximations was proven in certain case studies, e.g. [**104**], and the technical merit of such approximate models must be acknowledged. However, it is beyond the expectations to elaborate generally applicable quantitative formulae taking the complex non-radial stacking effects exhaustively into account. Instead, the following work strategy can be tracked in the literature. Qualitative trends related to non-radial blade stacking have been under exploration until recently, e.g. [**17, 24, 26-27, 43, 45-46, 54-56, 113-115**], with extensive use of experimentation as well as Computational Fluid Dynamics (**CFD**). Considering the qualitative experiences, various versions of non-radially stacked blading geometry can be individually designed. Afterwards, finding the most favourable blading version(s) is expected from CFD studies coupled with experiments, as e.g. in [**21, 28-29, 38**], using "cut-and-try" approaches [**116**], occasionally in an iterative manner. Besides such methodology, a recent trend is the application of CFD-based, algorithmized optimisation techniques [**117**]. In these methods, the blading versions under CFD surveillance do not originate from individual design (i.e. necessitating human contribution) but are tailored systematically by appropriate algorithms. Such algorithmized optimisation techniques incorporate non-radial stacking with the capacity to systematically adjust the stacking line shape [**52-53, 118-123**], as well as blade section geometry [**50, 116, 124**] and stagger. The strategies to harmonise the parametrized adjustment of various blading characteristics are aided by the formerly explored qualitative trends related to non-radial stacking.

The above underline the importance of qualitative knowledge on non-radial stacking effects. Accordingly, a main objective of the present thesis is to establish novel qualitative – and, to a certain extent, quantitative – guidelines contributing to the design of axial flow blading of sweep or skew, with special regard to CVD. These guidelines can be incorporated in the preliminary design (first cut) of blade geometry, and support the elaboration of CFD-based design strategies as well. The corresponding studies have been strongly supported by the departmental CFD experience related to fluid machinery [**125-129**].

Initiated by the aforementioned practical demands, the guideline of the work presented herein is, although not limited to, the exploration of combined effects due to CVD and FSW. Accordingly, the thesis chapters have been organized to the following logical structure:

- Effects of CVD to the near-endwall – more specifically, near-tip – region, influenced by FSW (Chapter 2),
- Effects of CVD away from the endwalls, influenced by FSW (Chapter 3),
- Systematic incorporation of FSW in the preliminary CVD methodology, based on the conclusions drawn in the previous chapters (Chapter 4).

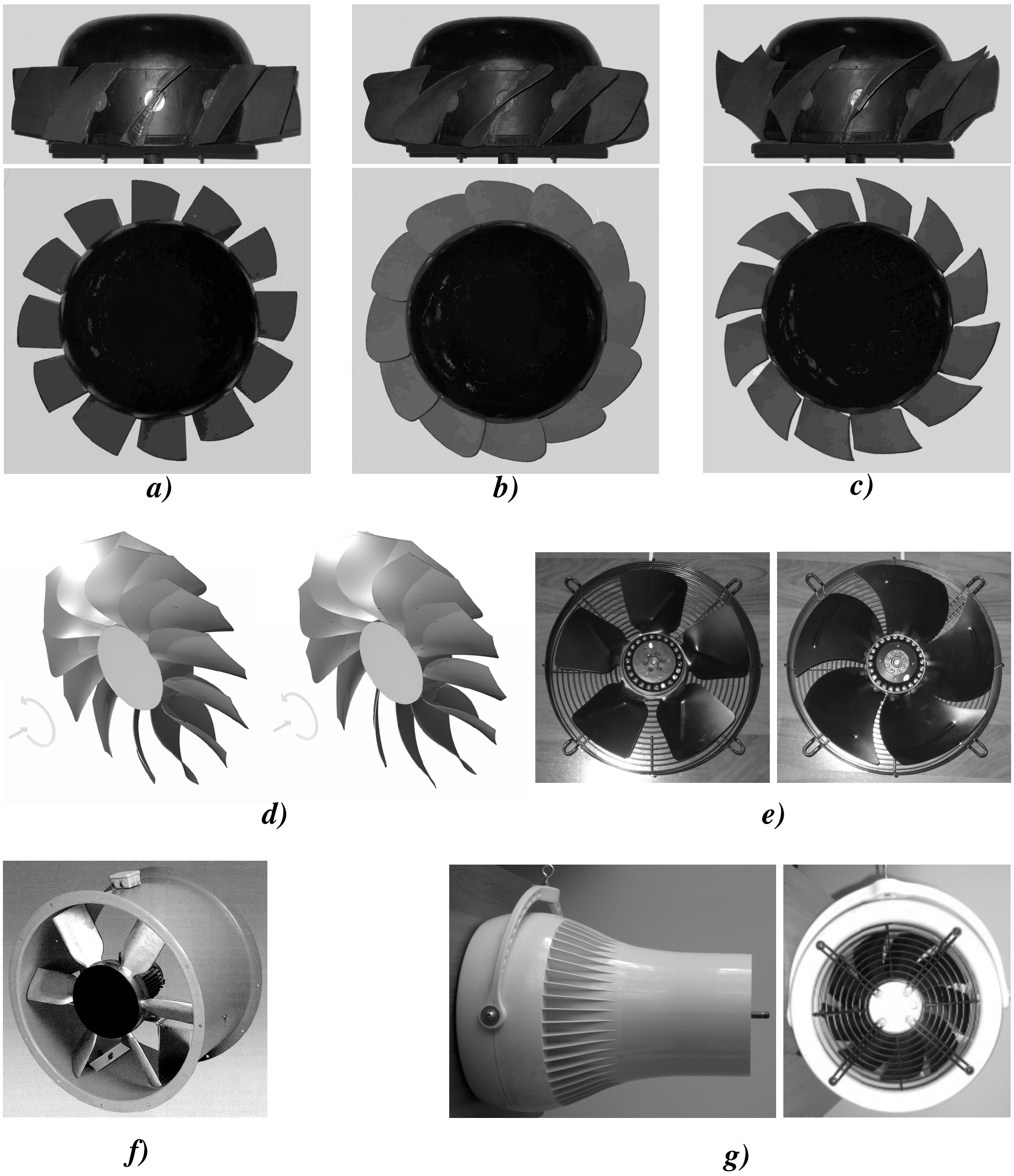

Figure 1.1. *Fan rotors designed and experimentally certified by the author in a basic R&D project [cases b), c)], designed under his supervision [case d)], and studied by him and his team within the framework of industrial projects* [*cases e), f), g)*]. ***a)*** *High-pressure ventilating fan of CVD with radially stacked blades* [**85, 93**]. ***b)*** *Redesign of case a) for modified spanwise blade circulation distribution* [**94**]. ***c)*** *Redesign of case a) incorporating FSW* [**95**]. ***d)*** *Sketch of a small-scale CVD industrial fan of high specific performance: Radially stacked (left) and slightly forward-skewed (right) versions* [**96**]. ***e)*** *CVD rotors of radially stacked and forward-skewed blades, applied in heat exchanger units* [**9, 97**]. ***f)*** *CVD industrial fan rotor of radial blade stacking and variable stagger* [**98-99**]. ***g)*** *Destratification jet fan of forward skewed blades* [**100**].

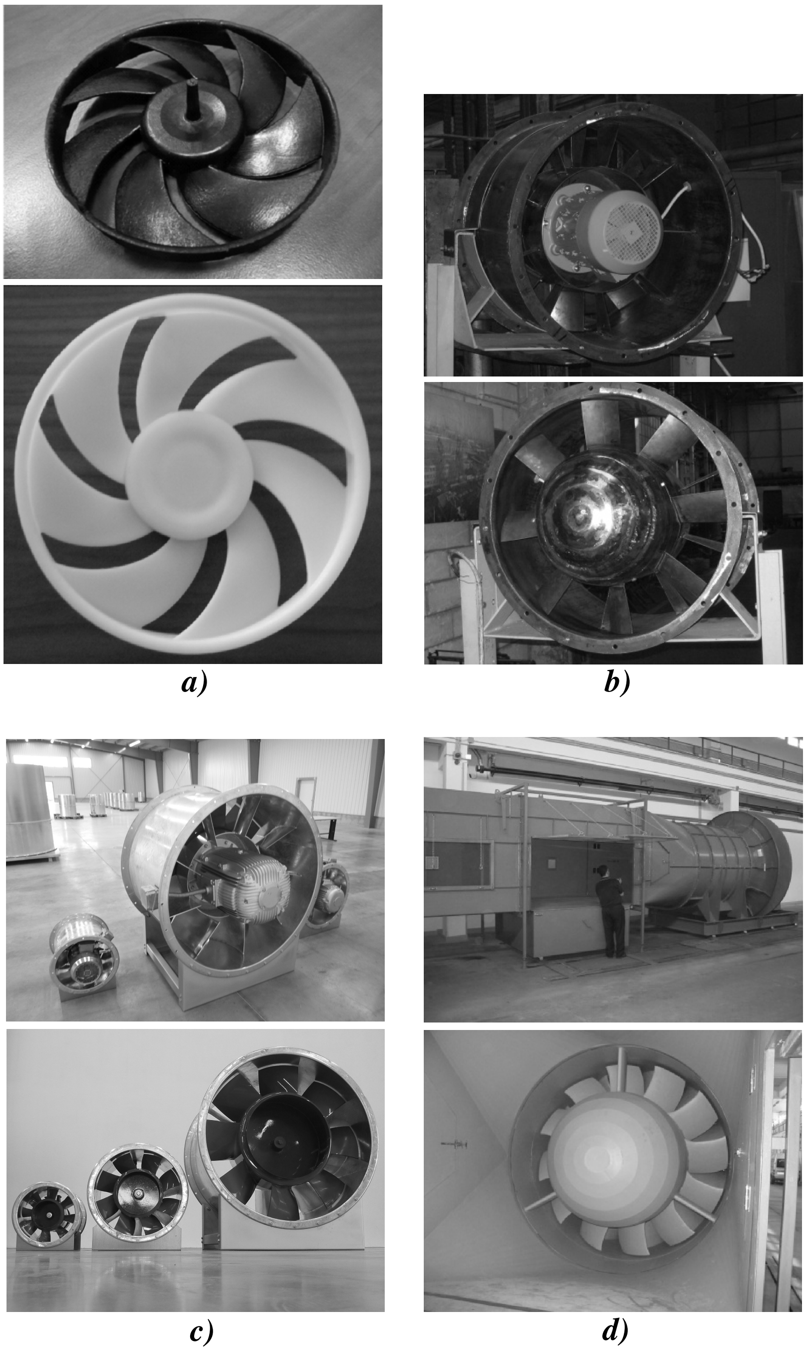

Figure 1.2. *Examples for axial fans of CVD designed by the author for industrial firms and end-users in Hungary, with specification of blade tip diameters.* ***a)*** *Electric motor cooling fans with forward-skewed blades, ∅ 110 mm, ∅ 124 mm* [**69**]. ***b)*** *Fan of long throw, with radially stacked blades, ∅ 710 mm* [**99, 101**]. ***c)*** *Flue gas extractor fans with radially stacked blades, ∅ 400 mm, ∅ 630 mm, ∅ 1250 mm* [**102**]. *Wind tunnel fan with forward-skewed blades, ∅ 2000 mm* [**103**].

2. RADIAL FLUID MIGRATION AND NEAR-TIP BLOCKAGE

2.1. Introduction

It is known that the fluid in the boundary layer of axial flow fan and compressor rotor blades migrates radially outward and accumulates near the tip [**19**], especially on the suction side, e.g. [**130-132**]. Based on e.g. [**1, 48, 133**], the present discussion focuses on the suction side of the blades, where the aerodynamic loss is expected to be more pronounced. The high-loss fluid stagnating near the tip contributes to increased local losses, and promotes "tip stalling" [**134**] at throttled conditions. It is also highlighted in [**1**] that the radial flows inside the blade profile boundary layer introduce spanwise gradients in blade circulation and losses, and increase the mixing loss. The undesired phenomenon of radial outward migration of high-loss fluid is generally interpreted as "outward centrifugation", as e.g. in [**19, 70, 135, 154, 191**], i.e. it is dedicated to the dominance of centrifugal force over the radial pressure gradient [**1**]. As a supplement to this simplified interpretation, it was aimed to elaborate and apply a model for comprehensive investigation of the factors influencing the radial outward migration of fluid, at the design flow rate. Up-to-date CFD techniques are available for the reliable prediction of 3D turbomachinery flow. It appears to be beneficial to supplement these techniques with analytical models for exploring the underlying physics of 3D flow effects. Lifelike simplified models (e.g. as in [**19, 136**]) may contribute to the elaboration of guidelines for controlling the related flow phenomena by design means.

Radial fluid motion is especially significant in the case of rotors of CVD. The aim of the present chapter is to explore the common aspects of radial outward migration, the related endwall blockage, and CVD. For this purpose, analytical modelling, evaluation of detailed flow measurement data, and quantitative analysis of endwall blockage have been carried out on comparative bladings of case study.

Studies in this subject performed by the author were preliminarily documented in [**4, 137-138, 144, 146**]. The author has summarized his new independent scientific results in [**139**].

2.2. Analytical modelling of radial fluid migration

2.2.1. Obtainment of radial acceleration

Let us consider a 3D streamline segment (**Figure 2.1**) fitting to point P where the geometrical and physical circumstances are under investigation. The radial coordinate is r. The r coordinate axis, characterised by unit vector $\underline{u}_r$, fits to P, intersects the z-axis of rotation (axial coordinate axis), and is normal to it. The projection of the streamline onto the cylindrical surface of radius r makes an angle α with the axis of rotation. The projection of the streamline onto the plane, being tangential to the streamline and containing the r axis, makes an angle ε with the cylindrical surface of radius r. An $[x, y, z]$ Cartesian coordinate system is introduced, for which z is the axis of rotation, the y-axis fits to the r axis, and $\underline{u}_x \times \underline{u}_y = \underline{u}_z$. The streamline is described parametrically with use of the $x(t)$, $y(t)$, $z(t)$ functions, for which the independent parameter t is the polar angle coordinate in the $[r, t, z]$ cylindrical coordinate system.

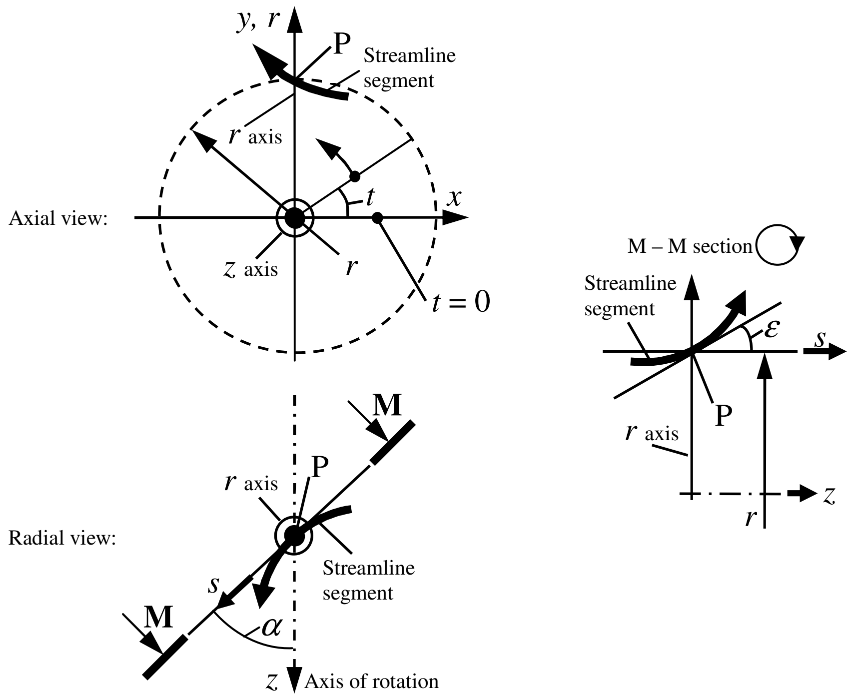

Figure 2.1. *Geometrical circumstances*

Derivative vectors $\underline{h}'_\mathrm{P}$ and $\underline{h}''_\mathrm{P}$ are obtained for P. $\underline{h}'_\mathrm{P}$ is composed by the first derivatives and $\underline{h}''_\mathrm{P}$ is composed by the second derivatives of the $x(t)$, $y(t)$, $z(t)$ functions with respect to t. See **Appendix A** for the details of $\underline{h}'_\mathrm{P}$ and $\underline{h}''_\mathrm{P}$, and for the definition of the $[r, n, s]$ coordinate system.

The centripetal acceleration of the fluid in the natural coordinate frame connected to point P can be expressed as follows. For explanation, see **Appendix B**.

$$\underline{a}_\mathrm{cp} = \frac{w^2}{\left|\underline{h}'_\mathrm{P}\right|^4}\left(\underline{h}'_\mathrm{P} \times \underline{h}''_\mathrm{P}\right) \times \underline{h}'_\mathrm{P} \tag{2.1}$$

The y-wise component of $\underline{a}_\mathrm{cp}$ in Eq. (2.1) is considered, being equal to the radial component of the centripetal acceleration (Fig. 2.1). It can be pointed out that

$$\left[\left(\underline{h}'_\mathrm{P} \times \underline{h}''_\mathrm{P}\right) \times \underline{h}'_\mathrm{P}\right]_y = \left[\left(x'^2 + z'^2\right) y'' - \left(x' x'' + z' z''\right) y'\right]_\mathrm{P} \tag{2.2}$$

The derivatives are to be substituted from Appendix A into Eq. (2.2). Using derivatives and trigonometric transformations yields

$$\left|\underline{h}'_\mathrm{P}\right|^4 = \left[\frac{r^2}{\sin^2\alpha}\left(1 + \tan^2\varepsilon\right)\right]^2 \tag{2.3}$$

Furthermore, $w = w_s / \cos\varepsilon$ is considered on the basis of Figure A1.d) in Appendix A.

Substitution of Eqs. (2.2) and (2.3) into Eq. (2.1) reads, after several steps, the following expression:

$$\left[\underline{a}_{\mathrm{cp}}\right]_y = \left[\underline{a}_{\mathrm{cp}}\right]_r = w_s^{\,2}\left[\frac{\partial\varepsilon}{\partial s} - \frac{\sin^2\alpha}{r}\right] \tag{2.4}$$

In the case of $\partial\varepsilon/\partial s = 0$, considering that $w_s \sin\alpha = w_u$, $[\underline{a}_{\mathrm{cp}}]_y = -\, w_u^{\,2}/r$. This corresponds to the classic view that, in the case of a cylindrical stream surface, the radial component of acceleration appears as the centripetal acceleration of fluid particles moving virtually at a tangential velocity w_u on a circle of radius r (conf. [**1**]).

The streamwise unit vector [tangential to the streamline, see Fig. A1.d) in Appendix A] in the natural coordinate frame connected to P is $\underline{u}_e = \underline{h}'_{\mathrm{p}} \big/ \left|\underline{h}'_{\mathrm{p}}\right|$. The streamwise acceleration of the fluid is

$$\underline{a}_e = w\frac{\partial w}{\partial e}\underline{u}_e \tag{2.5}$$

The radial component of the streamwise acceleration is obtained as follows, on the basis of Eq. (2.5). It is considered that $w = w_s/\cos\varepsilon$. Furthermore, $\partial w/\partial e = (\partial w/\partial s)\cdot(\partial s/\partial e)$, where $\partial s/\partial e = \cos\varepsilon$ [see Fig. A1.b) in Appendix A]. The y-wise component of $\underline{u}_e$, being equal to its radial component, is expressed using the derivatives in Appendix A, with the final result of $[\underline{u}_e]_r = \sin\varepsilon$. The above read, after several steps

$$\left[\underline{a}_e\right]_y = \left[\underline{a}_e\right]_r = w_s\left[\frac{\partial w_s}{\partial s}\tan\varepsilon + w_s\tan^2\varepsilon\frac{\partial\varepsilon}{\partial s}\right] \tag{2.6}$$

The sum of Eqs. (2.4) and (2.6) reads the radial component of fluid acceleration, considering intermediately that $(1+\tan^2\varepsilon)(\partial\varepsilon/\partial s) = \partial(\tan\varepsilon)/\partial s$:

$$a_r = w_s^{\,2}\frac{\partial(\tan\varepsilon)}{\partial s} + w_s\frac{\partial w_s}{\partial s}\tan\varepsilon - w_s^{\,2}\frac{\sin^2\alpha}{r} \tag{2.7}$$

Following the view in [**1**], two regions are distinguished in the vicinity of the blade: the boundary layer influenced by viscous effects, and the inviscid core flow. Let us study two neighbouring streamlines, as illustrated in **Figure 2.2**: one streamline in the suction side boundary layer of the blade, fitting point P; and the other one out of the boundary layer (in the core flow) near the boundary layer edge. Let us consider the characteristics a_r, w_s, ε, and α in Eq. (2.7), and also the local static pressure p and absolute velocity v, as the features of the fluid on the streamline in the boundary layer, in point P. On the streamline out of the boundary layer, the following characteristics are introduced, in analogy to the above ones: $a \rightarrow @$; $w \rightarrow W$; $v \rightarrow V$; $\varepsilon \rightarrow E$; $\alpha \rightarrow A$; $p \rightarrow P$. With these characteristics, the radial acceleration of the fluid out of the boundary layer is the following, in analogy to Eq. (2.7), taking equal r coordinates and approximating equal s coordinates for the two streamlines inside and outside the boundary layer (nearly parallel streamlines being close to each other):

$$@_r = W_s^2 \frac{\partial(\tan E)}{\partial s} + W_s \frac{\partial W_s}{\partial s} \tan E - W_s^2 \frac{\sin^2 A}{r} \tag{2.8}$$

2.2.2. *Equations of fluid motion*

The radial component of the Reynolds-averaged Navier-Stokes equation [**1**] in the boundary layer in the relative frame of reference is as follows:

$$a_r = -\frac{1}{\rho}\frac{\partial p}{\partial r} + g_{\mathrm{Cor}\,r} + r\omega^2 + f_{\nu\,r} \tag{2.9}$$

where $g_{\mathrm{Cor}\,r}$ is the radial component of the Coriolis force field, and $f_{\nu\,r}$ is the term manifesting the effect of Reynolds stresses in the radial direction. The present studies regard the turbulent boundary layer downstream of the laminar and transitional regions occurring near the leading edge of the blades [**1**]. As the measurements reported in [**1**] (e. g. Fig. 5.16 in [**1**]) suggest, the majority of radial outward flow occurs in the turbulent boundary layer, approx. 1 to 2 percent chord away from the blade surface. Away from the wall, one can neglect the molecular stresses, on the basis of [**140**]. Therefore, the effect of molecular viscosity is neglected herein, in comparison to Reynolds stress effects.

As Fig. 2.2 suggests, the blade rotational speed is $\underline{\omega} = 0 \cdot \underline{u}_r + \omega \sin\alpha\, \underline{u}_n - \omega \cos\alpha\, \underline{u}_s$. Furthermore, $\underline{w} = w_r\, \underline{u}_r + 0 \cdot \underline{u}_n + w_s\, \underline{u}_s$. This reads $g_{\mathrm{Cor}\,r}$, to be substituted into Eq. (2.9):

$$g_{\mathrm{Cor}\,r} = \left[2\underline{w} \times \underline{\omega}\right]_r = -2 w_s \omega \sin\alpha \tag{2.10}$$

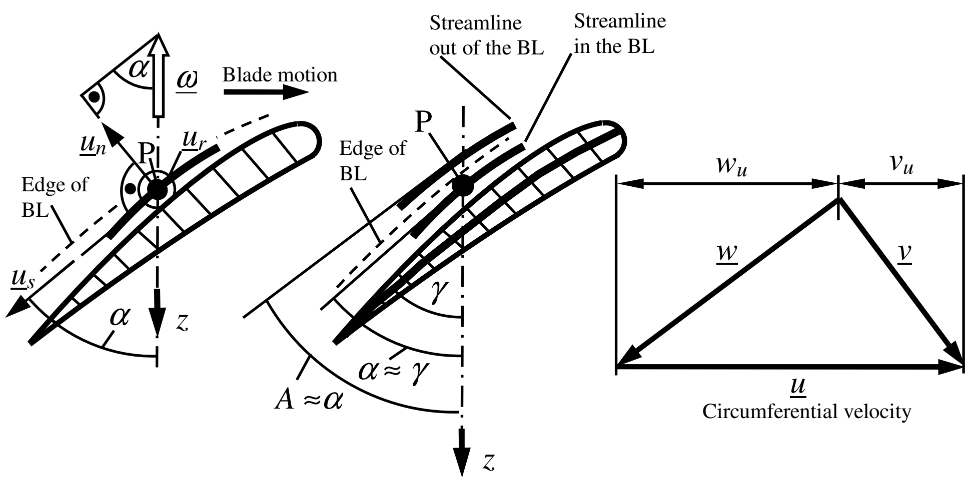

Figure 2.2. *Explanation of Coriolis force, angles, and velocity vector diagram. BL: boundary layer.*

By analogy with Eqs. (2.9) and (2.10), the radial component of equation of motion out of the boundary layer is as follows, neglecting shear forces related to both molecular and turbulent viscosity in the core flow (rotor blading without upstream objects is considered):

$$@_r = -\frac{1}{\rho}\frac{\partial P}{\partial r} - 2\,W_s\omega\ \sin A + r\omega^2 \qquad (2.11)$$

For the blade parts farther downstream of the leading edge, the approximation $A \approx \alpha \approx \gamma$ is applied from this point onwards, as illustrated in Fig. 2.2. As supported by [**1**], this assumption is reasonable for thin blades of moderate camber line curvature, at the design point, without drastic boundary layer thickening or separation.

It has been pointed out in references [**130, 132**] that for the blade region downstream of the leading edge, e. g. near the trailing edge, the boundary layer is characterised by a pronounced radial outward flow, especially on the suction side, being stronger than the radial fluid motion in the core flow.

At the entrance of fluid to the blade passage, it is assumed that the fluid moves along streamlines fitting to axisymmetric stream surfaces both in the vicinity of the leading edge and in the core flow. This yields the inlet condition $\varepsilon \approx E$. These angles are zero in the case of a perfect axial inlet condition (cylindrical inlet stream surfaces), but can be non-zero in mixed-flow turbomachinery or even in axial-flow machinery, due to the effect of the inlet nose cone. Further downstream of the leading edge, as the radial outward fluid migration in the boundary layer dominates over that in the core flow, $\varepsilon > E$ is generally valid [**130, 132**].

According to the experiences in [**130, 132**], it is assumed that

$$\frac{\partial(\tan\varepsilon)}{\partial s} \neq \frac{\partial(\tan E)}{\partial s}\ ;\ \frac{\partial(\tan\varepsilon)}{\partial s} = \frac{\partial(\tan E)}{\partial s} + \mu \qquad (2.12)$$

where the Greek symbol μ stands for the radial **M**igration ("mu") parameter, i.e. increment of s-wise derivative of tangent of yaw angle. Effects increasing μ stimulate the radial outward inclination of the streamline in the boundary layer with respect to the core flow. In contrast, effects reducing μ retard the outward boundary layer flow.

Subtracting Eq. (2.8) from Eq. (2.7) and Eq. (2.11) from Eq. (2.9) and combining the two resultant equations reads

$$w_s^{\,2}\mu = \left(W_s^{\,2} - w_s^{\,2}\right)\frac{\partial(\tan E)}{\partial s} + \left(W_s\frac{\partial W_s}{\partial s} - w_s\frac{\partial w_s}{\partial s}\right)\tan E - \frac{1}{2}\frac{\partial\left(w_s^2\right)}{\partial s}(\tan\varepsilon - \tan E) + \frac{\sin^2\gamma}{r}\left(w_s^{\,2} - W_s^{\,2}\right) +$$

$$+\frac{1}{\rho}\left[\frac{\partial P}{\partial r} - \frac{\partial p}{\partial r}\right] + 2\,\omega\sin\gamma\left(W_s - w_s\right) + f_{vr} \qquad (2.13)$$

It must be considered that $w_s \sin\gamma = w_u$ and $W_s \sin\gamma = W_u$, where u is the circumferential direction. This yields in Eq. (2.13) that $(\sin^2\gamma /r)(w_s^2 - W_s^2) = (1/r)(w_u^2 - W_u^2)$. Furthermore, $2\omega\sin\gamma(W_S - w_s) = (2u/r)(v_u - V_u)$ is applied, since $(W_u - w_u) = (v_u - V_u)$. Considering that $w_u = u - v_u$ and $W_u = u - V_u$ (see the velocity vector diagram in Fig. 2.2 for explanation), certain terms in Eq. (2.13) can be associated and simplified as follows:

$$\frac{\sin^2\gamma}{r}\left(w_s^2 - W_s^2\right) + 2\omega\sin\gamma\left(W_S - w_s\right) = \frac{1}{r}\left(v_u^2 - V_u^2\right) \tag{2.14}$$

Substitution of Eq. (2.14) into Eq. (2.13) reads

$$w_s^2\mu = \left(W_s^2 - w_s^2\right)\frac{\partial(\tan E)}{\partial s} + \left(W_s\frac{\partial W_s}{\partial s} - w_s\frac{\partial w_s}{\partial s}\right)\tan E - \frac{1}{2}\frac{\partial\left(w_s^2\right)}{\partial s}\left(\tan\varepsilon - \tan E\right) +$$

$$+\frac{1}{r}\left(v_u^2 - V_u^2\right) + f_{vr} + \frac{1}{\rho}\left[\frac{\partial P}{\partial r} - \frac{\partial p}{\partial r}\right] \tag{2.15}$$

Eq. (2.15) incorporates the simplified classic view of "outward centrifugation" [**1, 19, 31, 70, 135, 154, 191**], as detailed in **Appendix C**. The last term on the right-hand side of Eq. (2.15) could be neglected on the basis of Prandtl's boundary layer hypothesis (see Appendix C). However, it is retained herein, for a more detailed investigation.

2.2.3. Normal-wise coupling of equations of motion

This section discusses how to approximate the last term on the right-hand side of Eq. (2.15). The enlarged section in **Figure 2.3** presents the n-wise location of the two streamlines under discussion inside and outside the boundary layer, characterised by n coordinates 0 and N, respectively. n = 0 is assigned to the streamline inside the boundary layer, fitting point P. Point P has formerly been illustrated in Figs. 2.1 and 2.2. As suggested by Fig. 2.3 and explained in **Appendix D**, the following transformation can be applied:

$$\frac{1}{\rho}\left[\frac{\partial P}{\partial r} - \frac{\partial p}{\partial r}\right] = \frac{1}{\rho}\int_0^N\left[\frac{\partial}{\partial r}\left(\frac{\partial p}{\partial n}\right)\right]dn \tag{2.16}$$

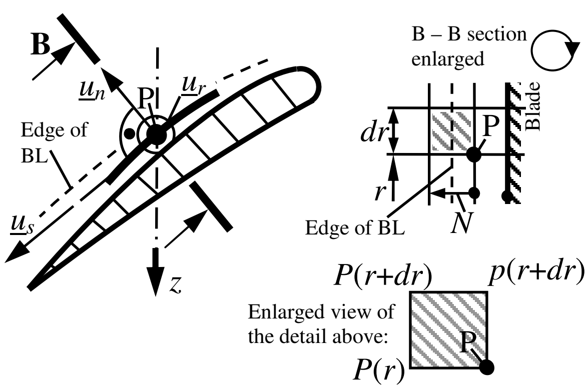

Figure 2.3. *Pressure characteristics*

For expression of $(1/\rho)(\partial p/\partial n)$ in Eq. (2.16), the n-wise component of the Reynolds-averaged Navier-Stokes equation is applied:

$$a_n = -\frac{1}{\rho}\frac{\partial p}{\partial n} + g_{\mathrm{Cor}\,n} + f_{v\,n} \tag{2.17}$$

where $g_{\mathrm{Cor}\,n}$ is the n-wise component of the Coriolis force field, and $f_{v\,n}$ is the term manifesting the effect of Reynolds stresses in the n direction (the effect of molecular viscosity is neglected again). Considering the explanation for Eq. (2.10), it can be pointed out that

$$g_{\mathrm{Cor}\,n} = [2\underline{w}\times\underline{\omega}]_n = 2w_r\omega\,\cos\alpha \tag{2.18}$$

As explained in **Appendix E**, the n-wise acceleration is

$$a_n = -\frac{w_s^{\,2}}{R_\alpha} + \frac{w_u^{\,2}}{r}\frac{\tan\varepsilon}{\tan\alpha} \tag{2.19}$$

Eqs. (2.18) and (2.19) are to be substituted into Eq. (2.17). $(1/\rho)(\partial p/\partial n)$ is to be expressed from Eq. (2.17) and is to be substituted into Eq. (2.16). This implies

$$\frac{1}{\rho}\left[\frac{\partial P}{\partial r} - \frac{\partial p}{\partial r}\right] = \int_0^N \left[\frac{\partial}{\partial r}\left(\frac{w_s^{\,2}}{R_\alpha} - \frac{w_u^{\,2}}{r}\frac{\tan\varepsilon}{\tan\alpha} + 2w_r\omega\,\cos\alpha + f_{v\,n}\right)\right]dn \tag{2.20}$$

2.2.4. Turbulence properties

$f_{v\,r}$ appearing in Eq. (2.9) is

$$f_{v\,r} = -\frac{\partial\left(\overline{w'_r\,w'_s}\right)}{\partial s} - \frac{\partial\left(\overline{w'_r\,w'_n}\right)}{\partial n} - \frac{\partial\left(\overline{w'^2_r}\right)}{\partial r} \tag{2.21}$$

f_{vn} appearing in Eq. (2.20) is

$$f_{v\,n} = -\frac{\partial\left(\overline{w'_n\,w'_s}\right)}{\partial s} - \frac{\partial\left(\overline{w'^2_n}\right)}{\partial n} - \frac{\partial\left(\overline{w'_n\,w'_r}\right)}{\partial r} \tag{2.22}$$

Detailed turbulence measurements reported in [**130, 141**] suggest that the changes of the temporal mean values of products of fluctuating velocity components are considerably smaller in s and r directions than their change in wall-normal direction. Therefore, $\partial/\partial s \ll \partial/\partial n$ and $\partial/\partial r \ll \partial/\partial n$ are briefly assumed. Accordingly, the first and third terms on the right-hand side of Eq. (2.22) are neglected. This yields in Eq. (2.20), with change of sequence of derivations with respect to r and n, and neglecting turbulence outside the boundary layer:

$$\int_0^N \frac{\partial f_{v\,n}}{\partial r}dn \approx -\int_0^N \frac{\partial}{\partial r}\left[\frac{\partial\left(\overline{w'^2_n}\right)}{\partial n}\right]dn \approx -\frac{\partial}{\partial r}\int_0^N d\left(\overline{w'^2_n}\right) \approx -\frac{\partial}{\partial r}\left[\overline{w'^2_n}\right]_0^N \approx \frac{\partial\left(\overline{w'^2_n}\right)}{\partial r} \tag{2.23}$$

Subtracting the final term in Eq. (23) from Eq. (2.20) yields

$$\frac{1}{\rho}\left[\frac{\partial P}{\partial r}-\frac{\partial p}{\partial r}\right]-\frac{\partial\left(\overline{w'^2_n}\right)}{\partial r}=\frac{1}{\rho}\left[\frac{\partial P}{\partial r}-\frac{\partial}{\partial r}\left(p+\rho\,\overline{w'^2_n}\right)\right] \tag{2.24}$$

This is a lifelike interpretation of the virtual increase of pressure in the boundary layer due to turbulent velocity fluctuations, represented by the Reynolds stress $\rho\,\overline{w'^2_n}$.

The final result in Eq. (2.23) is added to Eq. (2.21), yielding

$$\Sigma f_v = f_{v\,r} + \int_0^N \frac{\partial f_{v\,n}}{\partial r} dn = -\left[\frac{\partial\left(\overline{w'_r\,w'_s}\right)}{\partial s}+\frac{\partial\left(\overline{w'_r\,w'_n}\right)}{\partial n}\right]+\frac{\partial}{\partial r}\left(\overline{w'^2_n}-\overline{w'^2_r}\right) \tag{2.25}$$

2.2.5. Discussion on the effects influencing radial outward fluid migration in the suction side boundary layer

Eq. (2.20) is substituted into Eq. (2.15), and Eq. (2.25) is considered, giving the final result in Eq. (2.26). The derivatives of products and quotients in the integral in Eq. (2.20) are expressed in detail. Certain terms are transformed herein into a modified form, if such modifications are found beneficial from the viewpoint of interpretation. For a lifelike interpretation of results in terms of blade geometry, the formerly explained approximation $\alpha \approx \gamma$ has been applied. Furthermore, it has been presumed that $R_\alpha \approx R_C$, being reasonable again for thin blades at the design flow rate, without drastic boundary layer thickening or separation. These conditions mean that the shape of the boundary layer streamline is principally determined by the camber line geometry (local stagger angle, local camber radius).

Based on detailed measurement data in [**1**] (e.g. Fig. 5.16), the relative discrepancy $(R_\alpha - R_C)/R_C$ is estimated in the percent order of magnitude. This relatively small error propagates in Terms VII and VIII, being the most significant among the terms derived from Eq. (2.20) (see the data in Table 2.2 later). Therefore, the error introduced by the assumption $R_\alpha \approx R_C$ is found negligible in comparison to the effects related to the condition $\frac{\partial P}{\partial r} \neq \frac{\partial p}{\partial r}$.

Eq. (2.26) is presented in table format with Roman numerals referencing the individual terms, in order to make possible a systematic interpretation. The items in the table are to be summed to result in $w_s^2\mu$.

$w_s{}^2\mu =$ (2.26)

I	$\left(W_s{}^2 - w_s{}^2\right)\dfrac{\partial(\tan E)}{\partial s}$	**VIII**	$-\dfrac{1}{R_C^2}\displaystyle\int_0^N w_s{}^2\,\dfrac{\partial R_C}{\partial r}dn$
II	$\dfrac{1}{2}\dfrac{\partial}{\partial s}\left(W_s{}^2 - w_s{}^2\right)\tan E$	**IX**	$-\dfrac{2}{r\tan\gamma}\displaystyle\int_0^N w_u \tan\varepsilon \dfrac{\partial w_u}{\partial r}\,dn$
III	$-\dfrac{1}{2}\dfrac{\partial\left(w_s^2\right)}{\partial s}\left(\tan\varepsilon - \tan E\right)$	**X**	$\dfrac{1}{r^2\tan\gamma}\displaystyle\int_0^N w_u{}^2\tan\varepsilon\,dn$
IV	$\dfrac{1}{r}\left(v_u{}^2 - V_u{}^2\right)$	**XI**	$-\dfrac{1}{r\tan\gamma}\displaystyle\int_0^N w_u{}^2\,\dfrac{\partial(\tan\varepsilon)}{\partial r}dn$
V	$-\left[\dfrac{\partial\left(\overline{w'_r\,w'_s}\right)}{\partial s} + \dfrac{\partial\left(\overline{w'_r\,w'_n}\right)}{\partial n}\right]$	**XII**	$\dfrac{1}{r\sin^2\gamma}\displaystyle\int_0^N \tan\varepsilon\; w_u{}^2\,\dfrac{\partial\gamma}{\partial r}dn$
VI	$\dfrac{\partial}{\partial r}\left(\overline{w'^2_n} - \overline{w'^2_r}\right)$	**XIII**	$2\omega\cos\gamma\displaystyle\int_0^N \dfrac{\partial w_r}{\partial r}dn$
VII	$\dfrac{2}{R_C}\displaystyle\int_0^N w_s\,\dfrac{\partial w_s}{\partial r}dn$	**XIV**	$-2\omega\sin\gamma\displaystyle\int_0^N w_r\,\dfrac{\partial\gamma}{\partial r}dn$

In the present discussion, the data related to a blade section located at radius r are organized into groups as follows:

Group 1: R_C, γ, ω

Group 2: W_s, $\partial W_s/\partial s$, V_u

Group 3: w_s, $\partial w_s/\partial s$, v_u (and consequently, $w_u = r\omega - v_u$)

Group 4: $\tan E$, $\partial(\tan E)/\partial s$

As a brief approximation, the role of these groups can be interpreted in the following manner. The user demand is a prescribed fluid mechanical performance. This is presumed to necessitate certain velocity and acceleration conditions in the core flow (Group 2) and in the boundary layer (Group 3), to be realised by means of geometrical and operational characteristics (Group 1) prescribed in turbomachinery design.

The angle E and its s-wise change (Group 4) are considered as characteristics of the core flow determined by the geometry of the rotor environment and by the rotor design style. In the case of a rotor with no inlet guide vane, E>0 is realised if the rotor is of mixed-flow type with blade leading edges built on the inlet nose cone, or if it is of axial-flow type with a nose cone generating radial outward flow at the inlet. If the rotor is of free vortex operation, with a perfect axial inlet condition, the stream surfaces can be assumed to be cylindrical in the core flow, yielding $E \equiv 0$ and $\partial(\tan E)/\partial s \equiv 0$ (as demonstrated e.g. in [**130**]).

As pointed out in the literature survey in [**138**], the increase of specific rotor performance – a primary goal of CVD – generally tends to require an increased solidity as well as an increased spanwise gradient of blade circulation. The effect of increasing $d\hat{\psi}_{2,\mathrm{D}}/dR$ is twofold: i) the performance of the blade sections at higher radii can be enhanced – by increasing the blade load and/or the solidity –, thus increasing the overall specific performance of the rotor; ii) parallel to this, overloading of the blade sections near the hub can be avoided, by moderating the blade load. The higher the $d\hat{\psi}_{2,\mathrm{D}}/dR$, the more intense the vortices shed from the blade along the dominant part of the span (conf. [**1**]). Such effect is illustrated in a substantially simplified manner in **Figure 2.4**. If an elementary blade circulation increment $+d\Gamma$ is to be performed along the radius from r to $(r+dr)$, an elementary bound vortex of $d\Gamma$ is to be added to the vortex system bound to the blade at r. According to Helmholtz's theorem [**142-143**] (inviscid approach), the vortex filament corresponding to this elementary bound vortex is not interrupted at r but extends continuously toward the trailing edge and is shed from the blade. The sense of rotation of this elementary shed vortex corresponds to radial outward and inward flows on the suction side and pressure side, respectively. Up to the spanwise position of maximum circulation, such vortices are shed from the blade, forming a trailing vortex sheet. Near the blade tip, where the blade circulation decreases, the elementary circulation deficit $-d\Gamma$ corresponds to the moderation of bound vorticity. Accordingly, the other branch of the previously mentioned vortex filament is shed from the blade near the tip, with the sense of rotation being opposite to the other branch shed at lower radius. The effect of the multitude of vortices shed near the tip can be interpreted as flow by-passing the tip from pressure side to suction side, i.e. tip leakage flow.

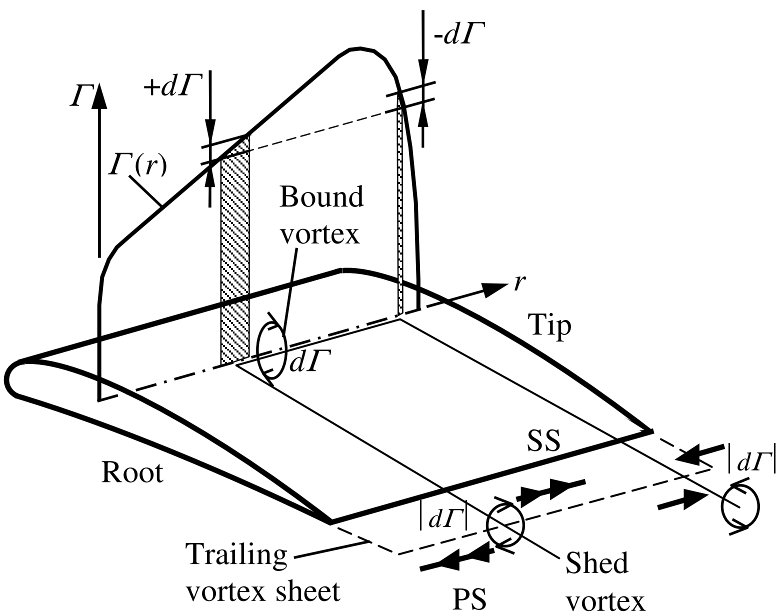

Figure 2.4. *Sketch for explaining vortex shedding corresponding to CVD*

Associated with the vortices shed from the blade due to increasing blade circulation along the dominant portion of span, rotors of non-free vortex operation, e.g. of CVD, exhibit radial outward and inward flows on the suction side and pressure side, respectively, corresponding to interblade stream sheet twisting [**144-145**]. **Figure 2.5** provides a CFD example, carried out by Dr. A. Corsini (Department of Mechanics and Aeronautics, University of Rome "La Sapienza"), for the development of such 3D flow, in the CVD rotor BUP-29 discussed later. Therefore, $E > 0$ is valid on the suction side for a blade of CVD. As Fig. 2.5 suggests, $\partial(\tan E)/\partial s > 0$ can be assumed near the LE, taking the axial inlet condition (E=0 at inlet). As the CFD studies in [**146**] demonstrate, $\partial(\tan E)/\partial s \approx 0$ can be assumed approximately further downstream.

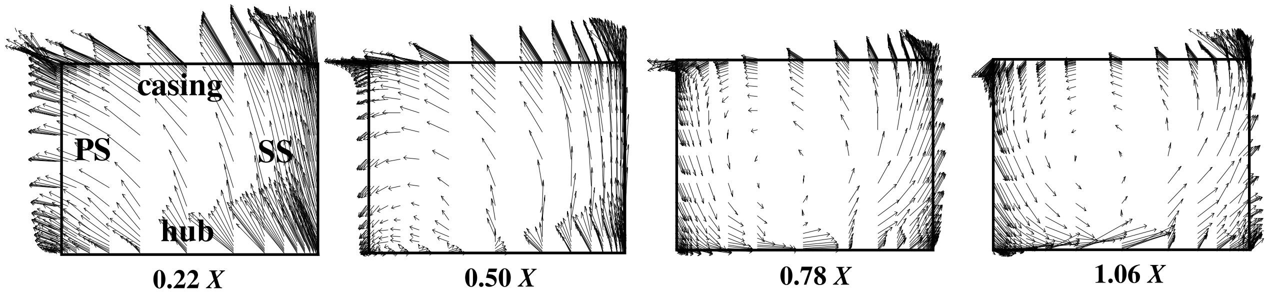

Figure 2.5. *Development of 3D flow in the blade passage of CVD rotor BUP-29. Secondary flow vector diagrams on planes normal to the axis of rotation. X: fraction of axial chord. X = 0: leading edge. X = 1: trailing edge. PS: pressure side. SS: suction side.*

In the following section, it is investigated 1) whether the terms in Eq. (2.26) stimulate the radial outward flow in the suction side boundary layer with respect to the core flow (indicated by increasing $w_s^2\ \mu$) or retard it (reducing $w_s^2\ \mu$), 2) what are the physical causes of radial outward migration of suction side boundary layer fluid, 3) and what engineering guidelines are suggested for its attenuation. For simplicity in formulation, the effects increasing or reducing $w_s^2\ \mu$ are termed briefly as "stimulating" or "retarding", respectively. The terms are referenced using the Roman numerals.

Term I Since the relative velocity is reduced due to viscous effects in the boundary layer, $(W_s^2 - w_s^2) > 0$. $\partial(\tan E)/\partial s > 0$ generally occurs, especially at the front part of the blade, if the rotor is of CVD (conf. Fig. 2.5 and [**26, 145**]). Therefore, viscosity, if it is coupled with CVD, tends to have a "stimulating" effect.

Term II As an example, detailed boundary layer studies presented in [**147**] show that downstream of the suction peak, the streamwise deceleration is more pronounced in the suction side boundary layer than in the core flow. This is due to the wall friction and the adverse pressure gradient. This yields $\partial(W_s^2 - w_s^2)/\partial s > 0$. $\tan E > 0$ occurs if the rotor is of CVD, and/or is of axial- or mixed-flow type with non-axial inlet condition due to the inlet nose cone. Therefore, the wall friction and adverse pressure gradient, if they are coupled with stream surface inclination in the core flow due to spanwise changing blade circulation and/or the effect of nose cone, tend to have "stimulating" effects.

Term III In the decelerating region downstream of the suction peak, $\partial(w_s^2)/\partial s < 0$. Once the radial outward fluid migration in the boundary layer starts to dominate over that in the core flow, as shown in [**130, 132**], $\varepsilon > E$. If the above trends dominate the blade passage, this term represents a “stimulating” effect.

Term IV The blade performs a solid body rotation. According to the no-slip condition and the effect of viscosity, the tangential absolute velocity of the fluid in the boundary layer approaches the circumferential velocity of the blade, and is always higher than the tangential velocity in the core flow: $v_u > V_u$. This yields $(1/r)(v_u^2 - V_u^2) > 0$ in each case. Therefore, viscosity in the suction side boundary layer has in itself a "stimulating" effect. Considering the left-hand side term in expression (C.4) in Appendix C, comparing the "centrifugal forces" in the boundary layer as well as in the core flow, Term IV may be regarded as representing the "centrifuging outward" effect according to the classic view [**1**].

Term V The Reynolds stresses related to $\overline{w'_r w'_s}$ and $\overline{w'_r w'_n}$ are zero if the fluctuations w'_s and w'_n are considered to be statistically symmetrical [**148**] about the given radial location. This assumption appears to be not far from reality for a turbomachine blade section being sufficiently far from the annulus walls, and yields that the effect of turbulent shear stresses is of moderate significance in radial boundary layer fluid migration. However, experiments provide more convincing information for judging the role of Term V. The measurements reported in [**130**] suggest that, except for the vicinity of the annulus walls,

$$\frac{\partial\left(\overline{w'_r w'_s}\right)}{\partial s} \approx 0, \quad \frac{\partial\left(\overline{w'_r w'_n}\right)}{\partial n} < 0 \tag{2.27}$$

This implies that spatial change of turbulent shear stresses tends to represent a “stimulating” effect.

Term VI If isotropic turbulence could be assumed, then $\overline{w'^2_n} = \overline{w'^2_r}$ could be applied, and therefore, the effects of this term were considered negligible. Since no evidence was found to confirm that this assumption is reasonable, the author surveyed the literature for experimental data. The measurements reported in [**141**] suggest that

$$\frac{\partial \overline{w'^2_n}}{\partial r} \geq 0, \qquad \frac{\partial \overline{w'^2_r}}{\partial r} \approx 0 \tag{2.28}$$

This yields that the spanwise change of virtual increase of pressure due to turbulent velocity fluctuations tends to represent a "stimulating" effect.

Term VII If the blade is of radial stacking, the neighbouring blade sections are displaced neither in the chordwise direction nor normal to the chord. For such cases, according to the radially increasing circumferential velocity of the blading, the relative mean velocity is likely to increase along the radial coordinate r, and so do the local relative velocity values. Therefore, $\partial w_s/\partial r > 0$ can be accepted in most cases as a brief approximation for rotor blades with radial stacking line, representing a "stimulating" effect.

Term VIII The curvature of the blade camber line usually decreases along the span (e.g. [**70, 130, 144**]), and therefore, $\partial R_C/\partial r > 0$. Considering the negative sign in the term, this tends to represent a "retarding" effect. The less the radial gradient of camber radius, the weaker the retardation.

Term IX It is considered that $\partial w_u/\partial r = \partial(u - v_u)/\partial r = \omega - \partial v_u/\partial r$.

Except for the extreme and unfavourable case of "forced vortex design" [**1**] in which solid body rotation is prescribed for the fluid, $\omega > \partial v_u/\partial r$, and, therefore, $\partial w_u/\partial r$ is positive. In fact, $\partial v_u/\partial r$ can be negative in many cases. For example, in the case of free vortex design, the spanwise constant Euler work necessitates that the pitchwise-averaged absolute tangential velocity of the fluid decreases hyperbolically along the radius. Considering the negative sign in the term, if $\tan\varepsilon > 0$ applies (nose cone and/or CVD design), $\partial w_u/\partial r > 0$ tends to represent a "retarding" effect. The higher the value of $\partial v_u/\partial r$, the weaker the retardation.

Term X This term tends to represent a "stimulating" effect if $\tan\varepsilon > 0$, i.e. if the fluid in the boundary layer already started to migrate outward.

Term XI This term can be neglected with the assumption of $\partial(\tan\varepsilon)/\partial r \approx 0$, i.e. assuming inclined but nearly parallel streamlines in the boundary layer at a given distance from the suction surface. This assumption appears to be reasonable farther from the annulus walls [**133, 145**].

Term XII According to the blade twist, $\partial\gamma/\partial r > 0$ is generally valid (e.g. [**70, 130, 144**]). However, this causes a "stimulating" effect only if $\tan\varepsilon > 0$.

Term XIII This term can be neglected with the assumption of $\partial(w_r)/\partial r \approx 0$. This assumption appears to be reasonable farther from the annulus walls [**145**].

Term XIV As explained for Term XII, $\partial\gamma/\partial r > 0$ is usually valid. Considering the negative sign in the term, this tends to represent a "retarding" effect.

2.3. Comparative case studies

2.3.1. Components of radial fluid migration: μ_i^* parameters

The measurement-based comparative case studies presented herein incorporate a rotor of free vortex design reported in [**131**] – labelled herein **INO** rotor – as well as the three CVD rotors discussed in [**144**], labelled as **BUP-26**, **BUP-29** and **BUP-103** rotors. **Table 2.1** summarises the overall geometrical and operational characteristics of the rotors, supplemented with data related to the tip as well as to endwall blockage (discussed later), at the design flow rate. The INO rotor has NACA 65 blade profiles – NACA 65(3.2A$_{10}$)06 at the tip section [**149**] –, and the BUP rotors have cambered plate blades with rounded leading edge and trailing edge. The spanwise variance of blade circulation prescribed in design has been characterised by a single representative $d\hat{\psi}_{2,\mathrm{D}}/dR$ value for each rotor. All the rotors in the table were designed for an axial inlet condition (swirl-free inlet), assuming cylindrical stream tubes through the blading. The flow has been considered incompressible. All of the rotors in Table 2.1 are radially stacked, i.e. no blade sweep, dihedral, or skew [**4**] have been applied.

The Lieblein diffusion factor [**110**], characterising suction side diffusion, and hence local blade loading (as referred to e.g. in [**1, 24**]), is specified in Eq. (2.29), and is given in Table 2.1 for the studied rotors:

$$D=\left(1-\frac{\cos\alpha_1}{\cos\alpha_2}\right)+\frac{\cos\alpha_1}{2\left(c/s_\mathrm{b}\right)}\left(\tan\alpha_1-\tan\alpha_2\right) \tag{2.29}$$

In order to make possible a comparison between the rotors from the perspective of radial fluid migration, Eq. (2.26) has been modified as follows:

- The equation has been divided by w_s^2.
- For estimating the magnitude of "stimulating" or "retarding" effects, it is important to consider the chord length, along which "stimulation" or "retardation" comes into effect. Even moderate μ may cause considerable radial migration and near-tip accumulation of high-loss fluid, if the particles are allowed to migrate along a blade passage of longer chord. In contrast, even higher μ can be less crucial if the high-loss fluid can evacuate from the blade passage of shorter chord, before reaching the near-tip zone. To account for such effects, μ has been multiplied by c, thus introducing a dimensionless migration parameter μ^* {according to Eq. (2.12), μ has a dimension of 1/[s] = 1/m}:

$$\mu^*=\mu\cdot c=\left[\frac{\partial(\tan\varepsilon)}{\partial s}-\frac{\partial(\tan E)}{\partial s}\right]\cdot c=\frac{\partial}{\partial(s/c)}\left(\tan\varepsilon-\tan E\right) \tag{2.30}$$

Table 2.1. *Rotor geometrical characteristics and flow data at the design flow rate*

Rotor	INO	BUP-26	BUP-29	BUP-103
N_b	12	12	12	12
ν_{ht}	0.60	0.68	0.68	0.68
$(c/s_b)_t$	1.00	0.83	1.05	1.25
γ_t [*deg*]	56.2	53.8	51.7	49.5
τ [*mm*]	3	3	3	3
τ/c_t %	2.6	2.2	1.7	1.5
τ/S %	3.3	2.9	2.9	2.9
Φ_D	0.50	0.50	0.50	0.50
Ψ_D	0.36	0.40	0.49	0.52
$Re_t/10^5$	2.39	3.31	4.18	4.98
$d\hat{\psi}_{2,D}/dR$	0 (FVD)	0.77	1.04	1.34
R_{EWB}	0.95	0.94	0.92	0.91
$(c/s_b)_{EWB}$	1.05	0.88	1.13	1.37
α_{1EWB}	62.2°	62.0°	61.5°	61.2°
α_{2EWB}	54.0°	50.0°	45.5°	43.0°
D_{EWB}	0.32	0.45	0.49	0.50
δ_x^*/τ	1.56	1.62	1.86	1.90

In the following section, the indices i correspond to the Roman numerals identifying the terms in Eq. (2.26). The case studies related to the components of μ^*, based on the μ_i terms detailed in Eq. (2.26), have been confined to midspan radius, at the design flow rate, near the suction side. For these regions, chordwise-averaged representative μ_i^* values were briefly estimated, for the range spanning from blade passage inlet to outlet. In the estimation, the geometrical and operational parameters as well as the detailed 3D velocimetry databases reported in [**131**] (hot-wire data) and in [**91, 144**] (LDA data) were used. The μ_i^* values are used herein as quantitative indicators for judgement of significance of effects influencing radially outward fluid migration. **Table 2.2** presents the most significant μ_i^* data. **Table 2.3** contains data on the estimated orders of magnitudes of the μ_i^* terms not included in Table 2.2. These data were approximated on the basis of detailed measurement or CFD results for typical rotor configurations in the open literature, referred to in

Table 2.3. As the data in Table 2.3 demonstrate, the related terms are mostly of lower order of magnitude than the terms in Table 2.2. The lowermost row in Table 2.2 presents the sum of all of the estimated μ_i^* values for each rotor.

Terms V to XIV were derived from Eq. (2.20). Out of them, data for Terms VII and VIII are presented in Table 2.2. These data demonstrate that it was worthwhile to consider $\left[\frac{\partial P}{\partial r}-\frac{\partial p}{\partial r}\right]$ in the present analysis, instead of neglecting it on the basis of Prandtl's boundary layer hypothesis.

Table 2.2. *Computed μ_i^* data*

Rotor	INO	BUP-26	BUP-29	BUP-103
μ_{I}^*	≈ 0	0.017	0.065	0.067
μ_{II}^*	≈ 0	0.009	0.032	0.033
μ_{III}^*	0.034	-0.006	-0.060	0.077
μ_{IV}^*	0.034	0.038	0.358	0.624
μ_{VII}^*	0.016	0.015	0.013	-0.019
μ_{VIII}^*	-0.014	-0.008	-0.007	-0.005
$\Sigma\mu^*$	0.069	0.065	0.402	0.778

Table 2.3. *Estimated ranges for μ_i^* data excluded from Table 2.2*

Term	Estimated value	Source
μ_{V}^*	$1\cdot10^{-2}$	[**130**]
μ_{VI}^*	$(1\div3)\cdot10^{-3}$	[**141**]
μ_{IX}^*	$-(1\div4)\cdot10^{-3}$	[**131, 144**]
μ_{X}^*	$(1\div10)\cdot10^{-4}$	[**131, 144**]
μ_{XI}^*	$(1\div3)\cdot10^{-3}$	[**131, 144-145**]
μ_{XII}^*	$(1\div10)\cdot10^{-4}$	[**131, 144**]
μ_{XIII}^*	$1\cdot10^{-3}$	[**131, 144-145**]
μ_{XIV}^*	$-(1\div4)\cdot10^{-3}$	[**131, 144**]

Exploring the main trends being consequently present in the data in Table 2.2, the following observations have been made for the reported comparative case studies.

- CVD tends to promote the radial outward migration in the boundary layer. This is indicated by the values of μ_{I}^* and μ_{II}^*, increasing as $d\hat{\psi}_{2,\mathrm{D}}/dR$ increases, i.e. as the shed vortices are expected to be stronger. This trend appears also in the $\Sigma\,\mu^*$ data related to the CVD rotors.
- The "centrifuging outward" effect dominates as the cause of radial outward migration in the boundary layer. This is indicated by the largest value of μ_{IV}^* for each rotor.
- Increasing the radial gradient of blade circulation, i.e. increasing $d\hat{\psi}_{2,\mathrm{D}}/dR$ by CVD, results in moderation of $\partial R_{\mathrm{C}}/\partial r$, weakening the retarding effect related to μ_{VIII}^* (data of decreasing absolute values as $d\hat{\psi}_{2,\mathrm{D}}/dR$ increases). However, the effect related to μ_{VIII}^* is generally weaker, especially for higher specific performance (represented by higher Ψ_{D}), than the effects discussed previously.

2.3.2. Detailed flow measurement data

Detailed experimental data are presented herein for supporting the view that CVD promotes the radial outward migration of high-loss fluid on the suction side. Following the methodology in [**131, 133**], plots of secondary-flow velocity vectors and relative kinetic energy defect coefficient maps were prepared for the exit of the BUP rotors, by processing the LDA data. The experimental technique and estimation of measurement uncertainty are summarised in [**138**]. The BUP rotor measurement data are shown in **Figure 2.6** for the design flow rate, while also including plots for the INO rotor. Enlarged diagrams are presented on the fraction of span above R=0.85 for better visibility, following the method applied in [**131**]. For this region, the average axial distance between the trailing edge of the BUP rotors and the LDA plane was approximately 8% of tip chord. The comparative data taken from [**131**] for the INO rotor was obtained at the downstream location of 7% of tip chord. The secondary flow velocity was obtained as a velocity component perpendicular to the design relative flow direction. The relative kinetic energy defect coefficient, suggesting the local loss, was defined as

$$\zeta_2 = \left(\hat{w}_{2,\mathrm{D}}^2 - w_2^2\right)/\hat{w}_{2,\mathrm{D}}^2 \qquad (2.31)$$

The data regions under discussion have been transformed into identical rectangular domains in the figure, to simplify comparison of the results. The plots are extended to a pitchwise range of 4/3 blade passage, in order to obtain a better view of the flow structure. Short vertical segments below the figures are drawn every 20% of blade pitch. The suction side and pressure side regions are labelled in the figures. The midline of the blade wake, characterised by a local maximum of relative kinetic energy defect, is approximated by a vertical solid line. For the ζ_2 plots, dashed contour lines indicate zero values.

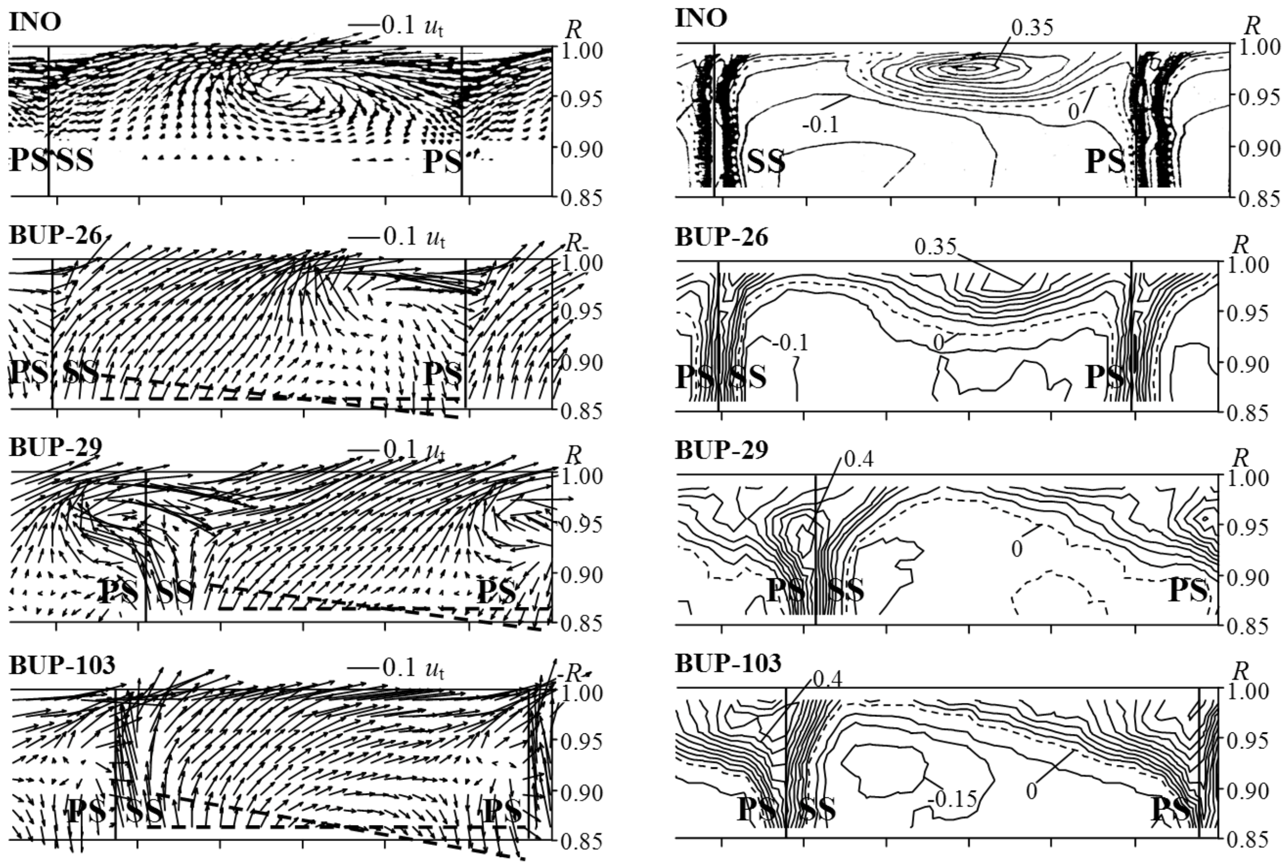

Figure 2.6. *Processed velocity measurement data. Left column: secondary flow vector plots for rotor exit planes. Right column: plots of rotor exit relative kinetic energy defect coefficient* ζ_2 *; increment: 0.05.*

Fig. 2.6 illustrates that the radial fluid motion is negligible farther from the casing wall for rotors of free vortex design, such as the INO type, since principally no vortices are shed from the blade using the free vortex design concept [**1**]. Considerable radial fluid motion can be observed only near the casing wall of INO, showing the pattern of tip leakage vortex roll-up. The limiting streamlines on the suction side, obtained from the CFD studies performed at the design point for a rotor of free vortex design in [**133**], also indicate that the radial velocity is negligible for the flow region farther from the endwalls. Some radial outward fluid motion is confined to the near-endwall regions, including the tip leakage flow. In contrast, the CFD simulation presented in [**26**] on BUP-29 (labelled in [**26**] as **USW** for „unswept") demonstrates that radial outward flow is dominant over the entire suction surface, at the design flow rate, for rotors of CVD. As Fig. 2.6 shows, the radial velocity varies approximately linearly in the pitchwise direction for the CVD rotors, as found also in [**70**], being inward on the pressure side and outward on the suction side. As pointed out in [**144**], the magnitude of the radial velocity is approximately proportional to the spanwise gradient of the blade circulation prescribed in design near midspan, characterised by $d\hat{\psi}_{2,\mathrm{D}}/dR$ in Table 2.1. This is illustrated by the angle between the dashed lines aligned with the starting and ending points of the secondary flow velocity vectors. This angle increases slightly in the sequence of BUP 26 → 29 → 103. As Fig. 2.6 illustrates, the tip leakage vortex roll-up also appears in the case of BUP-26, resulting in a secondary flow pattern similar to that of INO. However, the radially outward suction side flow appears to be combined with the rolling-up of the tip leakage vortex for BUP-26.

In the case of rotor INO of free vortex design, the zones of high relative kinetic energy defect are confined to the wake, the leakage flow, and the tip leakage vortex. The wake loss pattern is narrow near the tip radius, and is clearly isolated from the loss core of the leakage vortex. The zero ζ_2 contour line (dashed line) is characterised by an acute angle between the near-casing wall and the tip leakage vortex flow zone for rotor INO, suggesting that the vortex roll-up and the associated loss are of minor dependence on the 3D flow features at lower radii, farther from the tip, on the suction side. The narrowness of the wake loss pattern correlates with the computations in [**133**], indicating moderate loss over the entire suction surface of a free vortex designed rotor. In contrast, the zone of increased loss is continuous across the blade wake, the near-casing wall flow and the vortex core for BUP-26 of CVD. Compared to INO, increased loss can be observed for BUP-26 between the blade wake and the vortex core, overlapping with the zone of maximum intensity of radially outward velocity. Based on the above, it can be assumed that radial outward flow on the suction side due to CVD contributes to the near-tip losses, also generated in the loss core of the tip leakage vortex. This assumption is supported by [**26**]. The computational results reported on BUP-29 in [**26**] indicate a total pressure loss core near the suction side of the tip close to the trailing edge. This loss core appears in addition to the one corresponding to the leakage vortex. The additional loss core can be dedicated to the high-loss fluid moving radially outward along the suction side, the outward migration of which is intensified by the CVD concept.

As the plots in Fig. 2.6 suggest, the kinetic energy defect and the related near-tip endwall flow blockage are increased for each rotor of CVD, with an increased contribution by the near-tip suction side outward flow to the losses.

The conclusion that CVD promotes the outward migration and near-tip accumulation of suction side boundary layer fluid adds to the literature reporting on CVD rotors, e.g. [**1, 8, 26, 37, 61-63, 70-73**].

2.3.3. Endwall blockage studies

The stagnation of high-loss fluid near the casing causes substantial defect in relative velocity, i.e. endwall blockage [**150**], quantified by the displacement thickness [**1**]. In [**150**], when computing the blockage parameter, the blockage area – calculated from the velocity component resolved in the relative mainflow direction – was multiplied by the cosine of the relative flow angle (measured from the axial direction), in order to remove dependence of the blockage area on mainflow orientation. On this basis, the *axial* displacement thickness δ_x^* has been used herein, supported also by the methodology in [**26, 131, 145**], in the following dimensionless form:

$$\frac{\delta_x^*}{\tau} = \frac{1}{\tau/r_\mathrm{t}} \int_{R_\mathrm{EWB}}^{1} \left[1 - \frac{\hat{\varphi}(R)}{\hat{\varphi}_\mathrm{EWB}}\right] R\, dR \qquad (2.32)$$

For calculation of δ_x^*/τ, the edge of endwall blockage was defined as a radial location R_EWB at which the spanwise distribution of pitchwise-averaged relative exit flow angle starts to depart from the trend prescribed by design [**138**]. In the cases investigated, this location coincides fairly well with the radius of peak of pitchwise-averaged axial velocity.

The δ_x^*/τ values calculated from the measured velocity data are included in Table 2.1. The data suggest that the blockage becomes more pronounced, as the intensity of shed vorticity, represented by $d\hat{\psi}_{2,\mathrm{D}}/dR$, increases.

Reference [**150**] considers the following characteristics influencing the endwall blockage: blade loading, inlet boundary layer, clearance height, stagger angle, solidity, and blade loading profile. In what follows, the estimated effects of the aforementioned characteristics on δ_x^*/τ variations are discussed. Providing a fairly good fit to the parametric database in [**150**], BUP-29 was chosen as datum rotor, and modifications of blockage due to parameter changes were estimated on the basis of [**150**]. Only the three BUP rotors are considered at this point, since the INO rotor data do not correspond with the database in [**150**].

Inlet boundary layer. Since each BUP rotor is without inlet guide vane, with thin inlet boundary layer developed naturally along the duct located upstream, the variation of δ_x^*/τ due to inlet boundary layer effects is assumed to be insignificant.

Clearance height. It is stated in [**150**] that the endwall blockage is approximately proportional to the clearance height. Since τ is equal for each BUP rotor, the clearance height effect is excluded from the studies presented herein. It must be noted that the radial fluid migration is intensified by the presence of the tip gap. Reference [**131**] serves with measurement data on the radial fluid motion as function of tip gap size. Fig. 2.6 and data in [**131**] demonstrate that, even in the vicinity of tip radius, the radial fluid motion due to tip leakage is one order of magnitude weaker than that due to CVD, for the studied τ (up to 5 *mm* in [**131**]) as well as the reported $d\hat{\psi}_{2,\mathrm{D}}/dR$ parameters.

Blade loading profile. Reference [**150**] suggests that this feature is less significant in determining endwall blockage, and thus, it is neglected herein.

Loading. The D_{EWB} values in Table 2.1 are considerably lower than the limiting value of 0.6 proposed in [**74**] for moderation of loss in axial fans. Therefore, the slight variance in tip loading level of the BUP rotors is assumed to have only a weak effect on the variation of endwall blockage. This view has been confirmed by analysing the comparative experimental results in [**24**] on two rotor configurations near the design point. The rotating rig experiments in [**150**] also show that at moderate loading (near the design point), increase of loading results in only a slight increase of blockage. A significant increase was observed only as the stalled state was approached. By processing the data in [**24, 150**], the slope $S_{\delta D} = \partial(\delta_x^*/\tau)/\partial D_{\mathrm{EWB}} = 0.45$ was estimated for approximation of the δ_x^*/τ variation due to changes of D_{EWB}.

Stagger angle. Based on the quantitative data reported in [**150**], reflecting the trend that endwall blockage decreases with increasing γ, the slope $S_{\delta\gamma} = \partial(\delta_x^*/\tau)/\partial\gamma_t = -0.012$ was estimated to consider this effect. The change in γ_t is to be substituted in *deg*.

Solidity. As reported in [**150**], increasing the solidity decreases the blade loading for the same overall pressure rise, and this tends to reduce the blockage. This effect is considered herein by the slope $S_{\delta(c/s)} = \partial(\delta_x^*/\tau)/\partial(c/s_{\mathrm{b}})_{\mathrm{t}} = -0.40$, estimated on the basis of [**150**]. It must be added that if "double leakage" occurs, it acts against the aforementioned blockage-reducing effect [**24, 150**]. Double leakage means that the tip leakage flow intersects the pressure surface of the adjacent blade, and leaks across again. The LDA data presented for BUP-26 in Fig. 2.6 reveal that this rotor is free from double leakage. A highly efficient CFD technique has been elaborated by Corsini et al. [**26, 145**], with special emphasis on tracing the tip leakage vortex trajectory, also reported in more recent references [**63, 151-152**]. In Fig. 2.6, for BUP-29, the leakage vortex appears to interact with the wake at the measurement plane. However, the CFD data in [**26, 145**] justify that the trajectory of leakage vortex has not reached the adjacent blade inside the passage of BUP-29. For BUP-103, the occurrence of double leakage cannot be judged using the presented LDA data. However, it is assumed that even if double leakage occurs for this rotor, it is confined to the vicinity of the trailing edge, and therefore, it does not affect significantly the development of endwall blockage. This assumption is supported by the following comparison. The CFD results presented in [**24, 150**] focus on investigating double leakage. In the double-leaking cascade reported in [**24, 150**], the leakage/freestream interface intersects the adjacent blade at approximately mid-chord under the following circumstances: near-stall throttling condition; $(c/s_{\mathrm{b}})_{\mathrm{t}} = 1.35$. For BUP-103, the design operational state results in considerably lower blade loading, and the solidity is also moderate. These features attenuate the inclination for double-leakage. In addition to the above, if double-leakage would occur in BUP-103, the additional blockage effect presented later in Fig. 2.7 would be overestimated for BUP-103. As the figure shows, this is not the case (the data point related to BUP-103 remains below the linear trend line). Based on the above, double-leakage is neglected herein for each BUP blading.

The change in blockage for rotors BUP-26 and BUP-103, relative to the datum rotor BUP-29, has been approximated as a linear combination of partial changes due to the modification of various parameters. The partial changes have been estimated to be proportional to the parameter modifications. As pointed out formerly, the blade parameters influencing the blockage changes of the BUP rotors and reported in [**150**] are the following: loading – represented herein by D_{EWB} –; stagger angle γ_t; and solidity $(c/s_{\mathrm{b}})_{\mathrm{t}}$. This parameter set has been supplemented herein by $d\hat{\psi}_{2,\mathrm{D}}/dR$ as a new parameter, representing the spanwise blade circulation gradient prescribed in CVD.

The endwall blockage component due to spanwise changing circulation is approximated for each rotor as

$$\Delta\left(\delta_x^*/\tau\right)_{\mathrm{CVD}} = S_{\delta\mathrm{CVD}} \cdot \frac{d\hat{\psi}_{2,\mathrm{D}}}{dR} \tag{2.33}$$

Where $S_{\delta\,\mathrm{CVD}}$ is the slope of endwall blockage function with respect to $d\hat{\psi}_{2,\mathrm{D}}/dR$. This equation has been constructed by such means that the influence of the spanwise circulation gradient on endwall blockage must diminish if $d\hat{\psi}_{2,\mathrm{D}}/dR \to 0$, i.e. in the free vortex design case.

Utilising Eq. (2.32), the blockage for the datum rotor BUP-29 is expressed as

$$\left(\delta_x^*/\tau\right)_{\mathrm{BUP-29}} = \left(\delta_x^*/\tau\right)_0 + S_{\delta\,\mathrm{CVD}} \cdot \left(\frac{d\hat{\psi}_{2,\mathrm{D}}}{dR}\right)_{\mathrm{BUP-29}} \tag{2.34}$$

where the first term on the right-hand side expresses the blockage component of BUP-29 being independent of the spanwise circulation gradient.

The blockage is expressed for rotors BUP-26 and BUP-103 using the following function:

$$\left(\delta_x^*/\tau\right) = \left(\delta_x^*/\tau\right)_{\mathrm{BUP-29}} + \Delta\left(\delta_x^*/\tau\right) \tag{2.35}$$

where

$$\Delta\left(\delta_x^*/\tau\right) = S_{\delta D} \cdot \Delta D_{\mathrm{EWB}} + S_{\delta\gamma} \cdot \Delta\gamma_{\mathrm{t}} + S_{\delta(c/s)} \cdot \Delta\left(c/s_{\mathrm{b}}\right)_{\mathrm{t}} + S_{\delta\mathrm{CVD}} \cdot \Delta\left(\frac{d\hat{\psi}_{2,\mathrm{D}}}{dR}\right) \tag{2.36}$$

Each term indicated by Δ expresses the quantity related to the rotor under consideration minus the quantity related to the datum rotor BUP-29.

The combination of Eqs. (2.33) to (2.36), substitution of the formerly specified, known S_δ values as well as the data from Table 2.1, and a linear regression using the least squares method result in the approximation of Eq. (2.33), presented in **Figure 2.7** as a solid line. The three data points related to the unswept CVD rotors are also shown (from left to right: BUP-26, BUP-29, BUP-103). The figure confirms that endwall blockage increases nearly proportionally to the spanwise circulation gradient, in the case of no sweep. The relatively large values of $\Delta(\delta_x^*/\tau)_{\mathrm{CVD}}$ with respect to the total blockage (δ_x^*/τ) underline the importance of considering the effect of spanwise blade circulation gradient in endwall blockage.

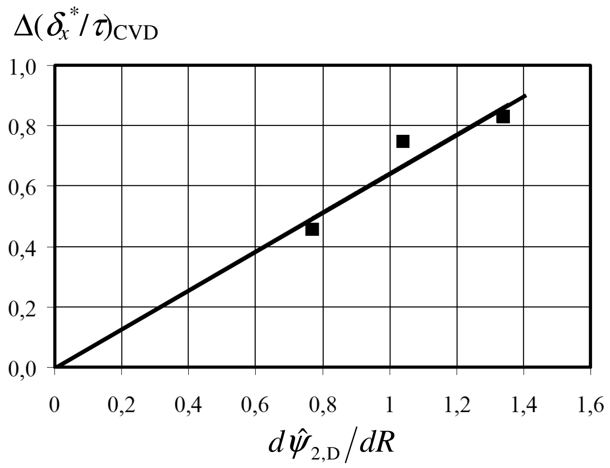

Figure 2.7. *Contribution of effect of spanwise changing blade circulation to endwall blockage*

2.4. Moderation of radial outward fluid migration in the suction side boundary layer

In the following section, it is discussed systematically how the radial outward fluid migration can be moderated by rotor and blade design means.

Out of the terms found to be significant and thus presented in Table 2.2, μ_{II}^* suggests that realisation of inlet condition possibly the closest to axial inflow helps to moderate the radial outward flow in the suction side boundary layer, via the reduction of tan E. This can be achieved by means of an appropriately shaped inlet cone. However, this requires a nose cone of extended axial size. This is a disadvantage from the ergonomic point of view in many industrial fan applications (increased space demand). The unfavourable effect of adverse pressure gradient established for μ_{II}^* can be moderated by applying controlled diffusion blade profiles, e.g. [**1, 153**].

μ_{VII}^* offers a guideline for moderation of radial outward suction side boundary layer flow, via reduction of $\partial w_s/\partial r$. In order to give a lifelike interpretation, the term is transformed as follows:

$$\frac{2}{R_{\mathrm{C}}}\int_0^N w_s \frac{\partial w_s}{\partial r} dn = \frac{1}{R_{\mathrm{C}}}\int_0^N \frac{\partial\left(w_s^{\,2}\right)}{\partial r} dn \tag{2.37}$$

In a simplified approach, $\partial(w_s^2)/\partial r$ represents the radial gradient of the relative dynamic pressure. With its reduction, in accordance with the simplified Bernoulli equation, the radial gradient of the static pressure can be increased, representing increased force acting against the radial outward migration of the suction side boundary layer fluid.

A means for reducing $\partial w_s/\partial r$ is FSW, as illustrated in **Figure 2.8**. In the case of radially stacked blades, the centres of gravity of the individual blade sections are stacked on a radial line. In contrast, a blade is of FSW if the sections of a radially stacked datum blade are shifted parallel to their chord in such a way that a blade section under consideration is upstream of the neighbouring blade section at lower radius [**4**]. Since the high-loss suction side boundary layer fluid appears to accumulate near the blade tip in the vicinity of the trailing edge [**19**], it is intended to reduce $\partial w_s/\partial r$ downstream of the suction peak. Referring to the points under investigation illustrated in Fig. 2.8, the following velocity conditions are established for the radially stacked blade – here, subscripts A, B, C, and D refer to the points in Fig. 2.8:

$$w_{s\,\mathrm{A}} := w_s \tag{2.38a}$$

$$w_{s\,\mathrm{B}} = w_s + \left(\frac{\partial w_s}{\partial s}\right)_{\mathrm{RS}} ds \tag{2.38b}$$

$$w_{s\,\mathrm{C}} = w_s + \left(\frac{\partial w_s}{\partial r}\right)_{\mathrm{RS}} dr \tag{2.38c}$$

$$w_{s\,\mathrm{D}} = w_s + \left(\frac{\partial w_s}{\partial r}\right)_{\mathrm{RS}} dr + \left(\frac{\partial w_s}{\partial s}\right)_{\mathrm{RS}} ds \tag{2.38d}$$

Let us assume that even if the blade section at the radius $r+dr$ is shifted in the upstream direction, the blade sections at both r and $r+dr$ preserve the original velocity and static pressure distribution in their vicinity. Although this assumption is not perfectly realistic, studies, e.g. in [**19, 26, 103**], suggest that if the blade is swept forward, the static pressure isolines are inclined a slightly greater degree "more forward" than in the case of an unswept blade, i.e. the local velocity and static pressure circumstances tend to follow the geometry of the stacking line. The assumption yields, as illustrated by Fig. 2.8, that

$$w_{s\,\mathrm{A\,FSW}} = w_{s\,\mathrm{A}} \tag{2.39a}$$

$$w_{s\,\mathrm{D\,FSW}} = w_{s\,\mathrm{D}} \tag{2.39b}$$

The combination of Eqs. (2.38a), (2.38d), (2.39a), and (2.39b) yield that

$$\left(\frac{\partial w_s}{\partial r}\right)_{\mathrm{FSW}} = \frac{w_{s\,\mathrm{DFSW}} - w_{s\,\mathrm{AFSW}}}{dr} = \left(\frac{\partial w_s}{\partial r}\right)_{\mathrm{RS}} + \left(\frac{\partial w_s}{\partial s}\right)_{\mathrm{RS}} \cdot \frac{ds}{dr} \tag{2.40}$$

Considering that ds/dr = -tan λ, (Fig. 2.8), Eq. (2.40) yields

$$\left(\frac{\partial w_s}{\partial r}\right)_{\mathrm{FSW}} - \left(\frac{\partial w_s}{\partial r}\right)_{\mathrm{RS}} = -\left(\frac{\partial w_s}{\partial s}\right)_{\mathrm{RS}} \tan\lambda \tag{2.41}$$

Since $(\partial w_s/\partial s)_{RS} < 0$ is valid in the decelerating flow downstream of the suction peak, and it has been assumed that the flow circumstances are preserved for a given blade section even if sweep is applied, i.e. $(\partial w_s/\partial s)_{RS} = (\partial w_s/\partial s)_{FSW}$, Eq. (2.41) suggests that the radial outward migration of suction side boundary layer fluid can be retarded by application of $\tan \lambda < 0$, i.e. forward sweep [**4**]. This conclusion confirms the "intuitive" model in [**18-19, 26, 43, 191**], summarised as follows, and illustrated in **Figure 2.9**. FSW inclines the isobar lines on the suction side in the forward direction in the decelerating zone after the blade suction peak, resulting in an additional radial pressure gradient acting against the outward migration. (Such “more forward” inclination of isobar lines of FSW blading can be observed e.g. in Fig. 3.6 near the blade leading and trailing edges.) This verbally expressed intuitive model has been exceeded in the present discussion, by systematic application of the analytical model, enabling the comprehensive consideration and systematisation of factors influencing the outward migration, using fluid mechanical principles presented in the form of descriptive mathematical formulae.

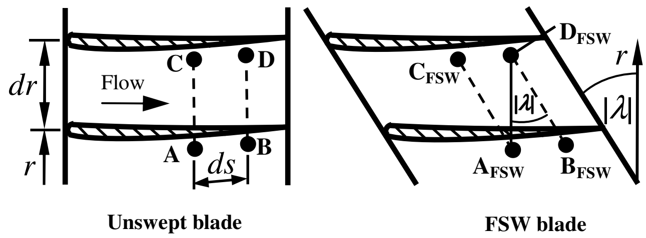

Figure 2.8. *Sketch on the effect of FSW*

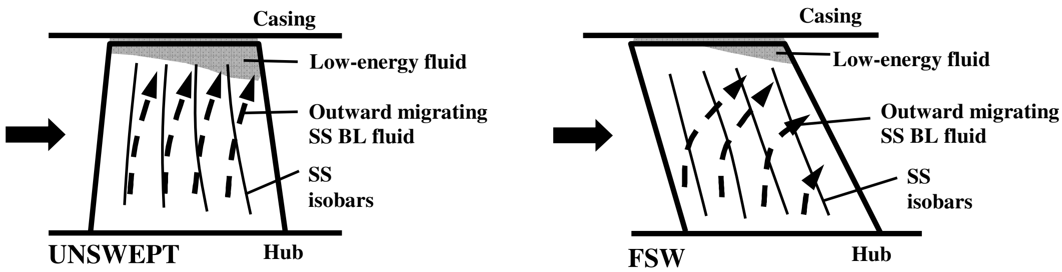

Figure 2.9. *Sketch, prepared after* [**19**], *on the suppression of radially outward flow of suction side boundary layer (SS BL) fluid by means of FSW* [**4**]

Beside the benefit of FSW on moderation of outward migration of the suction side boundary layer fluid, this favourable effect is coupled with the possible reduction of loss associated with the tip leakage flow. FSW results in positive sweep [**4**] near the tip. It has been pointed out that positive sweep provides a possible means for reducing tip clearance losses as a result of chordwise redistribution of tip section loading toward a more uniform loading distribution, e.g. [**17**].

The benefits of FSW, applied to rotor BUP-29, have been demonstrated e.g. in [**26**], in terms of the retardation of outward migration of low-energy fluid on the suction side as well as the moderation of endwall blockage and the associated losses. The data in [**25**] indicate that, in the region $R > R_{\mathrm{EWB}} = 0.92$ (conf. Table 2.1), the mass-averaged total pressure loss reduction due to FSW is approximately 2 per cent of dynamic pressure calculated with inlet relative velocity at midspan. This improvement due to FSW is in the same order of magnitude with the loss reduction presented in [**27**], and reported as a remarkable benefit.

The above findings lead to the conclusion that the benefits of FSW in the moderation of near-tip losses can be especially exploited for rotors of CVD. This statement supplements the literature reporting on non-radially stacked rotors of CVD [**19, 21, 37, 43, 50, 154**], referring even very recently to centrifuged boundary layer flow [**191**] and studying endwall blockage [**155**].

The presented analytical model offers a possibility for expanding the formerly developed models describing spanwise migration of aerofoil boundary layer, e.g. in [**156**], by presenting a detailed view of the underlying physics. It intends to contribute to the initiative formulated very recently that the interblade flow must be studied in three-dimensions for turning the knowledge about 3D flow into useful guidelines for assessing aerodynamic behaviour [**157**].

The pronounced benefits of FSW applied to rotors of CVD are in agreement with the view published in [**158**]. In the cited work, the authors conclude that only a modest aerodynamic improvement can be achieved by FSW for fan bladings of moderate load, low solidity, and free vortex design; and the benefits of FSW are likely to be more significant in the presence of stronger non-free vortex flow, i.e. for fans of CVD.

As stated in [**24**], it is impossible to generalise how aerodynamic features such as sweep impact performance for all blading types. Accordingly, inspired by [**150**], it was aimed herein to deepen the physical insight into, and thus to give guidance for control of, the effects related to the outward migration of suction side boundary layer fluid, and the associated increase in endwall blockage, instead of making efforts to establish generally valid quantitative correlations. The trends are to be quantified by means of extensive CFD campaigns on particular blading sets covering parameter ranges of interest.

2.5. NEW SCIENTIFIC RESULTS [4, 139]

Thesis point 1 [**139**] The author has elaborated an analytical model on the effects influencing the radial outward fluid migration in the rotor blade suction side boundary layer, contributing to increased near-tip loss and promoting tip stalling. With use of the model, the author has carried out an especially detailed systematic investigation on the aforementioned effects, exceeding the simplistic interpretation of "outward centrifugation" outlined in the literature.

The author has introduced radial migration parameters μ_{i}^{*} in the analytical model, as quantitative indicators of significance of effects influencing the radial fluid motion. The author has obtained representative μ_{i}^{*} values in an experimental case study. Such quantitative study has been supplemented by the author by investigating on the details of the measured flow field. On this basis, the author has drawn the following conclusion, widening the knowledge published so far in connection with CVD. CVD tends to intensify the outward migration and near-tip accumulation of fluid in the suction side boundary layer, in comparison to free vortex design. Such tendency is related to the suction side radially outward blade passage flow, associated with the vortices shed from the blade of spanwise changing circulation.

Thesis point 2 [**139**] The author has found that the outward migration, and consequently, the near-tip endwall blockage, becomes more pronounced as the intensity of shed vortices due to CVD – represented by the magnitude of radial gradient of blade circulation – increases. Accordingly, the set of blade parameters known formerly to influence the endwall blockage has been supplemented by the author with a new parameter $d\hat{\psi}_{2,\mathrm{D}}/dR$. Based on experiments, the author has quantified the following approximate relationship, which can be utilized in preliminary design. In the case of straight blades, the increase in axial displacement thickness due to CVD is proportional to $d\hat{\psi}_{2,\mathrm{D}}/dR$ at the near-tip endwall.

Thesis point 3 [**4, 139**] Exceeding the verbally expressed intuitive model available in the literature, the purposeful use of the analytical model discussed in Thesis point 1 has led the author to the conclusion that FSW is a means for the moderation of radially outward migration along the suction surface. In the view that CVD tends to promote outward migration, referring to Thesis points 1 and 2, the author has concluded as follows. The benefit of FSW, in terms of moderating near-tip loss, can be better utilised for the rotors of CVD, in comparison to free vortex design. The establishment of this fact complements earlier publications discussing non-radial stacking applied to bladings of CVD, but disregarding the combined aspects of FSW and CVD discussed herein.

3. CORRELATION OF FLOW PATH LENGTH TO TOTAL PRESSURE LOSS IN DIFFUSER FLOWS

3.1. Introduction

Decelerating flows frequently occur in components of hydraulic and air supply systems. They also characterise the blade passages of diffuser vanes and rotors of enthalpy-increasing turbomachinery. It is of great practical importance to be able to control the total pressure loss developing in such diffuser flows. This chapter aims to provide an analysis that focuses on the relationship between the total pressure loss and the distance travelled by fluid particles over the solid surfaces bounding diffuser flows. By such means, qualitative and, to a limited extent, quantitative guidelines can be incorporated in the preliminary design of axial flow turbomachinery blades, in order to achieve efficiency gain. High-fidelity quantification of total pressure loss [**26**] and finalization of blade geometry can then be carried out on the basis of systematic use of CFD tools (e.g. [**129**]).

The main practical concern of the chapter is to explore the relationship between CVD, flow path length, and total pressure loss. The chapter reports on a part of a systematic survey of the effects of CVD on axial rotor aerodynamics along the blade span. The studies reported in the previous chapter [**139**] were concerned with the *near-endwall zone*, i.e. the near-tip region. To supplement [**139**], the present chapter draws conclusions about CVD-related effects *away from the endwalls*.

As stated in [**157**], understanding the 3D flow behaviour, and turning the knowledge about 3D flow into useful engineering guidelines is a challenge even nowadays. This chapter aims to establish preliminary blade design guidelines based on a 3D concept.

Preliminary studies in the subject of this chapter were published by the author in [**4, 159**]. His new independent scientific results in the topic have been summarized in [**160**].

3.2. Preceding remarks

The following notes are important for specifying the subject of the chapter.

Ad 1. Incompressible flows (ρ = constant) are assumed, in order to exclude aerodynamic losses related to compressibility effects, e.g. shock losses [**1**].

Ad 2. Wall-bounded decelerating flows are considered.

Ad 3. Flow scenarios are overviewed for which the total pressure loss $\Delta p'_t$ is dedicated primarily to the growth or even separation of the boundary layer in the aforementioned decelerating flows. In order to get a general view of the underlying physics, diffuser flows at various levels of complexity will be discussed in a synthetic manner. The discussion will include the following.

- Quasi-one-dimensional (**Q1D**) – axial – flows developing in diffusers used in hydraulic or air distribution systems. Conical diffusers will be discussed herein, as e.g. in [**143, 161-163**].
- 2D – linear – blade cascade flows, providing experimental databases for preliminary design of axial flow turbomachinery, e.g. [**72, 105, 110**].
- 3D – annular – blade cascade flows in axial turbomachinery, including both rotors and diffuser vanes, e.g. [**1, 26, 31, 48, 74**].

The 2D and 3D blade cascade flows are analogous to diffuser flows [**1**]. It has been postulated in the aforementioned reference that boundary layer growth in the region of the adverse pressure gradient controls the static pressure rise. This is the region of decelerating flow on the suction side downstream of the suction peak. In [**1**], the blade cascade is viewed as an "equivalent diffuser" with inlet velocity being equal to the peak suction velocity. This view is supported by reference [**112**]. Here, the authors neglected the contribution toward loss from the pressure surface. Reference [**48**] focuses also on loss reduction on the suction side.

On the basis of the above, the cascade loss is associated herein with the suction side region downstream of the suction peak.

Ad 4. The growth of the boundary layer is considered to be intensified by two factors [**1, 143**]:

- Effect of skin friction (surface shear stress) along the solid wall surface
- Adverse streamwise pressure gradient in the decelerating flow.

The present discussion excludes the effect of surface roughness, also influencing boundary layer growth, as reference [**72**] suggests.

Ad 5. The flow path length L is defined as the length of the studied path line of the fluid particles along the solid surface. Such path line is

- Q1D for Q1D – conical – diffuser flows.
- 2D for 2D – linear – blade cascade flows.
- Generally 3D for 3D – annular – blade cascade flows.

L is the length of the effect of skin friction along the solid wall ("blade wetted" length, after [**112**], for blade cascade flows). L, also referred to as "diffusion length" in [**1**], demonstrates the length of flow path along which the fluid particles are exposed to adverse streamwise pressure gradient.

Ad 6. A "comparative case study" comprises flow scenarios for which the inlet and outlet geometrical characteristics and mean velocity vectors are fixed. This enables L to be considered as the sole independent variable. Therefore, the effect of changing L on the development of $\Delta p'_t$ can be investigated within a particular comparative case study.

For practical aspects of fixing the inlet and outlet geometrical characteristics and mean velocity vectors, as well as for an explanation of η_D, η_t, and ω (both ω_v and ω_w), see **Appendix F**.

Ad 7. The Reynolds number effect, associated primarily with laminar separation, is excluded from the case studies discussed herein. For a detailed discussion, and for a definition of Reynolds number, see **Appendix G**.

Ad 8. Within a comparative case study, the streamwise distribution of adverse pressure gradient is assumed to follow the same trends. For example, a local peak of deceleration, possibly generating boundary layer separation impacting on the entire downstream region (appearing e.g. in [**166**]), is excluded. The above are enabled by the following circumstances.

- Q1D diffuser flows: similar contouring style of diffusers, e.g. conical shape.
- 2D blade cascade flows: similar camber style (e.g. parabolic arc); similar profile thickness distribution (e.g. *C4* profile); minimum-loss incidence, as discussed (e.g.) in [**74, 110**].
- 3D blade cascade flows: similar camber style and profile thickness distribution; operational state in the vicinity of the best efficiency point, i.e. design flow rate, corresponding to near-minimum-loss incidence; and exclusion or at least moderation of separation zones. The latter conditions suit the aim of this chapter to seek qualitative guidelines for achieving the best available efficiency.

3.3. Discussion

A logical process is applied in the chapter, illustrated as follows. Two preceding statements – "premises" – will logically imply a "conclusion" statement. Such a logical process is indicated using the symbol shown in the following example: $\begin{smallmatrix} \mathrm{P1} & & \mathrm{P2} \\ & \searrow\swarrow & \\ & \mathrm{C1} & \end{smallmatrix}$, where P1 and P2 are the two premises, and C1 is the conclusion drawn. The conclusion resulting from such a process may be used as a premise in a consecutive one.

The plausibility of each *statement* is supported in the *justification* section subsequent to the statement.

- ***Statement*. Premise P1.** The consequence of decrease – or increase – of flow path length L is the monotonous decrease – or increase – of the effect of wall skin friction and the associated boundary layer growth.

Justification

Q1D flows. In the case of the classic example of a flat plate of zero incidence, the boundary layer thickens along the plate, i.e. with increase of the flow path length [**72, 143, 163**].

2D flows. Reference [**110**] (p. 203, Fig. 146) presents a diagram of wake momentum thickness θ^*, normalized by c. Even at zero diffusion, i.e. at zero adverse streamwise pressure gradient, θ^*/c shows a nearly constant non-zero value. This implies that the extent of boundary layer growth increases with c, i.e. with increasing flow path length. As commented on in the reference, the non-zero value of θ^*/c at zero diffusion predominantly represents the basic friction loss (wall skin friction).

- ***Statement.*** **Premise P2.** The consequence of decrease – or increase – of flow path length L is the monotonous increase – or decrease – of adverse streamwise pressure gradient and the associated boundary layer growth.

Justification

Since a comparative case study fixes the inlet and outlet velocities (see comment "Ad 6" in Section 3.2), the associated pressure rise is realized via a higher – or lower – streamwise gradient if the diffusion length decreases – or increases.

The following statements, C1 to C4, are various formulations of the conclusion drawn from premises P1 and P2. **Figure 3.1** qualitatively illustrates these statements.

- ***Statement.*** **Conclusion C1.** $\overset{\text{P1}\ \ \text{P2}}{\searrow\swarrow}$ C1 A minimum exists for total pressure loss.
- ***Statement.*** **Conclusion C2.** $\overset{\text{P1}\ \ \text{P2}}{\searrow\swarrow}$ C2 An optimum flow path length L_{opt} – associated with a critical adverse streamwise pressure gradient G_{crit} – exists for the minimization of total pressure loss.

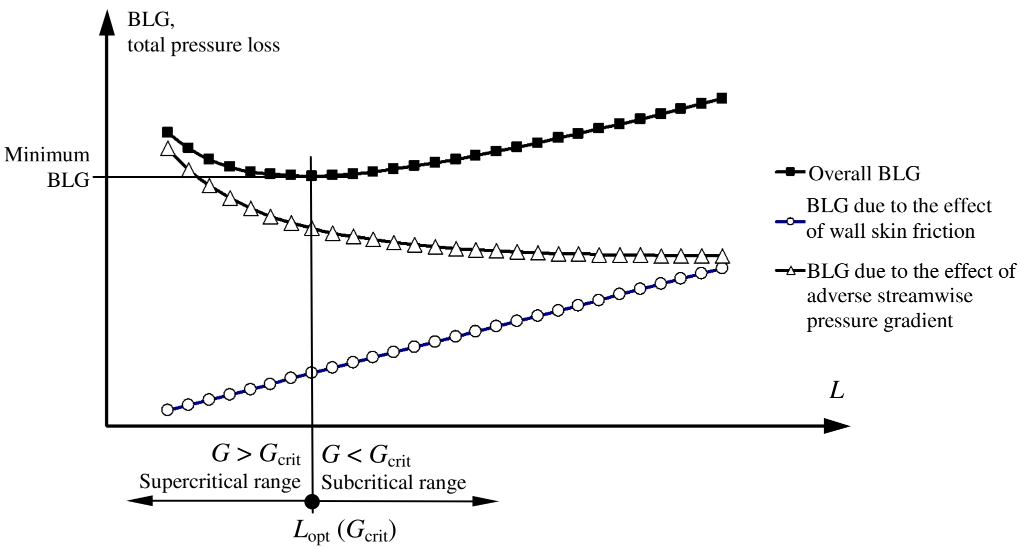

Figure 3.1. *Qualitative trends related to boundary layer growth (BLG in the figure)*

Fig. 3.1 shows the minimum loss at L_{opt}, occurring due to the counter-acting effects formulated in premises P1 and P2 related to modification of L. Flow paths longer – or shorter – than L_{opt} represent the subcritical – or supercritical – ranges from the viewpoint of adverse pressure gradient.

Justification

Q1D flows. For conical diffusers, reference [**163**] reports on an optimum cone angle, implying the existence of an optimum diffuser length, given that a comparative case study fixes D_{D1} and D_{D2} (see comment "Ad 6" in Section 3.2). In [**143**], such optimum cone angle is linked explicitly to the best diffuser efficiency η_D for a given outlet-to-inlet area ratio.

Figure 3.2, obtained on the basis of [**161**], presents the total pressure loss as a function of flow path length, for conical diffusers, for three representative diameter ratios. For explanation of obtaining L and ω_v, see **Appendix H**. Fig. 3.2 adds to the open literature on diffuser loss. It demonstrates the trends outlined in Fig. 3.1. For a given diameter ratio, the loss increases, if the flow path length is reduced below the optimum value (associated with minimum loss). If the flow path length exceeds the optimum value, the loss increases with the flow path length. Increased outlet-to-inlet diameter ratio, i.e. increased diffusion, leads to pronounced loss.

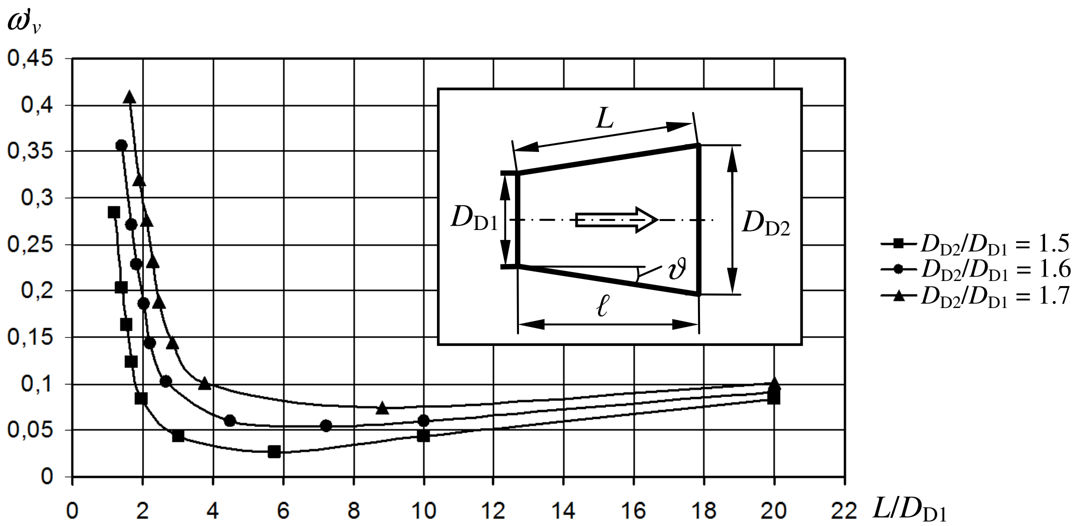

Figure 3.2. *Total pressure loss developing in conical diffusers (after* [**161**]*)*

2D flows. For linear cascades, L is approximated herein as the blade chord length c. In the first example, the work equation for the axial flow cascades, rearranged from p. 197, Eq. (3.18) in [**1**], is referred to:

$$\frac{c}{s_b} C_L \approx 2\cos\alpha_\infty \left(\tan\alpha_1 - \tan\alpha_2\right) \qquad (3.1)$$

where $\alpha_\infty = \tan^{-1}[(\tan\ \alpha_1+\tan\ \alpha_2)/2]$. In [**72**], citing (e.g.) [**105**], plots are presented, showing the existence of optimum solidity as a function of α_2 and (α_1-α_2). This means that an optimum chord length c – associated with L_{opt} – is assigned to given inlet and outlet flow conditions, at fixed blade spacing s_{b}. An optimum lift coefficient $C_{\mathrm{L\ opt}}$, associated again with the optimum solidity via Eq. (3.1), is defined in [**72**]. $C_{\mathrm{L\ opt}}$ relates implicitly to a maximum lift-to-drag ratio, as a function of inlet and outlet angles. As discussed in [**164**], the increase – or decrease – of lift-to-drag ratio leads to the gain – or deterioration – of cascade efficiency. The above imply the following.

- If the lift coefficient exceeds $C_{\mathrm{L\ opt}}$ ("overloading"), a given static pressure rise is intended to be realized by blades of "too short" a chord. Consequently, the supercritical G leads to pronounced boundary layer growth, deteriorating the lift-to-drag ratio relative to the $C_{\mathrm{L\ opt}}$ case.
- If the lift coefficient is below $C_{\mathrm{L\ opt}}$ (insufficient utilization of blade loading capability), a given static pressure rise is intended to be realized by blades of "too long" a chord. Consequently, the boundary layer growth associated with pronounced skin friction along the "too long" flow path deteriorates the lift-to-drag ratio again.

The second example is related to reference [**110**]. This states that the estimation of loss based on the diffusion factor D can serve as a basis for determining an optimum solidity. The optimum solidity results in the minimum computed loss coefficient for given inlet and outlet velocity conditions. Based on [**110**], the total pressure loss coefficient can be approximated as follows.

$$\omega'_v \approx 2\left(\frac{\theta^*}{c}\right)\frac{c}{s_{\mathrm{b}}}\frac{1}{\cos\alpha_2}\left(\frac{\cos\alpha_1}{\cos\alpha_2}\right)^2 \qquad (3.2)$$

The Lieblein diffusion factor D is defined in Eq. (2.29).

Figure 3.3 represents θ^*/c as a function of D, processing an extensive database involving various cascade and blade profile geometries [NACA 65-(A_{10})10 series, and British *C4* parabolic arc profile] ([**110**], reproduced from Fig. 148). Although the conclusions in [**110**] are based on blade cascades characterised by the aforementioned profiles, the moderation of loss relying on the D criterion is a general concept for various profile geometries [**74**], also including circular arc-cambered blades with a thin profile of uniform thickness [**25-26**]. The trend line described by Eq. (3.3) has been fitted to the data set, indicated by a bold line in the figure. The square of the correlation index r_c^2 [**167**] for the range of D = 0 to 0.7 is also reported below.

$$\theta^*/c = 6.2\cdot10^{-3} + 3\cdot10^{-4}\cdot\exp(6.34\cdot D) \qquad r_c^2 = 0.81 \qquad (3.3)$$

A comparative case study is carried out as follows. α_1 and α_2 is fixed. Then, D is computed for various solidity values. By inserting the values of D into Eq. (3.3), and substituting Eq. (3.3) into Eq. (3.2), the loss coefficient ω'_v can be expressed as a function of solidity. **Figure 3.4** presents the result for three representative inlet and outlet flow angle data couples, relevant to high-pressure industrial fans. These trends are similar to those noted in Fig. 3.2, showing that the same effects govern the development of loss in the Q1D and 2D flows being studied. The figure also indicates that increased turning, i.e. increased diffusion, leads to pronounced loss.

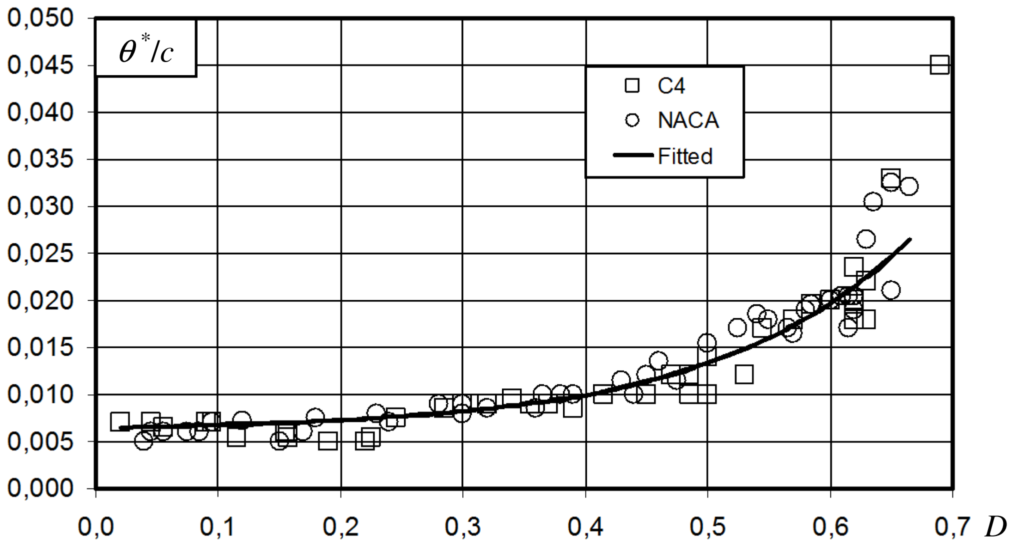

Figure 3.3. *Correlation between D and θ^*/c (after* [**110**]*)*

Fig. 3.4 also presents the D factors as a function of solidity. The data points $D(\omega_{\min})$ representing the D values related to the minimum loss coefficient are indicated. These are in accordance with the literature recommendations [**74, 110**] that $D \le 0.6$, or, for certain high-pressure fan applications [**74**], $D \le 0.7$ should be realized for loss moderation. However, the figure draws attention to how D values being excessively low relative to $D(\omega_{\min})$, i.e. the realization of a given diffusion by blading of "too long" a chord, leads to the increase of loss via increasing the effect of skin friction.

- ***Statement.* Conclusion C3.** $\begin{smallmatrix}\mathrm{P1} & & \mathrm{P2}\\ \searrow & & \swarrow\\ & \mathrm{C3} & \end{smallmatrix}$ The consequence of decrease of flow path length L is the decrease of total pressure loss, provided that the adverse streamwise pressure gradient remains subcritical ($G < G_{\mathrm{crit}}$).

- ***Statement.* Conclusion C4.** $\begin{smallmatrix}\mathrm{P1} & & \mathrm{P2}\\ \searrow & & \swarrow\\ & \mathrm{C4} & \end{smallmatrix}$ The consequence of increase of flow path length L is the increase of total pressure loss, if the adverse streamwise pressure gradient is subcritical ($G < G_{\mathrm{crit}}$).

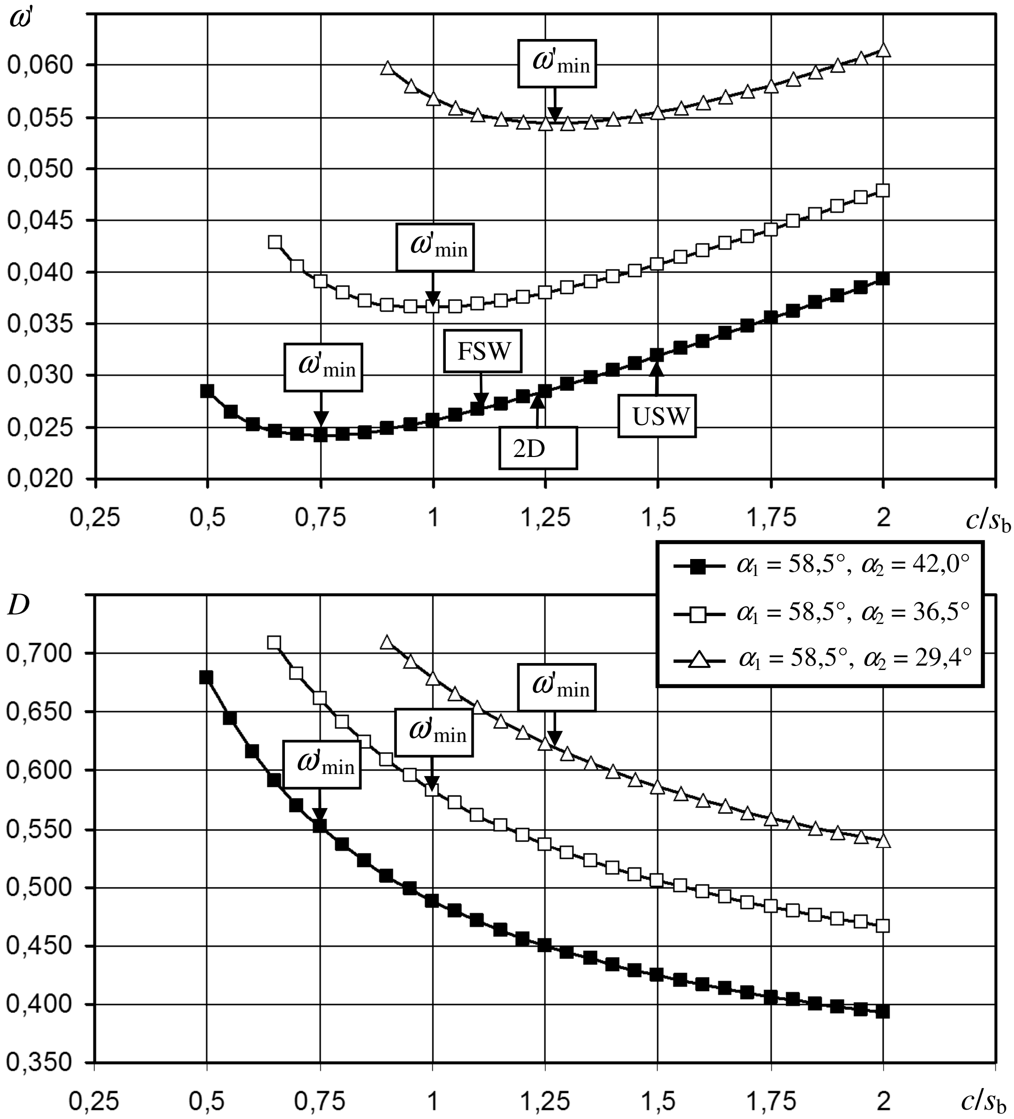

Figure 3.4. *Loss developing in 2D blade cascades (after* [**110**]*). Top: total pressure loss coefficient* ω' *as a function of solidity. Bottom: Lieblein diffusion factor D as a function of solidity. For the compared 3D cases of USW and FSW rotors, the studied flow path lengths L are applied instead of blade chord c.*

Justification

1D and 2D flows. The former examples, illustrated in Figs. 3.2 and 3.4, support conclusions C3 and C4 as well.

3D flows. In what follows in the thesis

- 3D annular blade cascade flows are discussed.
- The flow region away from the annulus walls is studied, in order to moderate endwall effects.

3D interblade flow effects modify the length of flow paths in annular flows. For example, [**168**] reports that intensification of the radial outward flow increased the "effective chord length", by elongating the paths of fluid particles over the blade surface. Another example is the effect of blade sweep [**4**]. Sweep introduces three-dimensionality to the originally 2D throughflow (via cylindrical stream surfaces), elongating the flow path, as explained in [**2**] and illustrated in [**169**]. As [**48**] reports, the streamlines of swept rotors indicate a longer trajectory of the particles over the suction surface, which was found to increase the boundary layer thickness. Even minor changes in flow path length were found to cause remarkable change in growth of the boundary layer. Reference [**112**] draws attention to how, when sweep is introduced, c/s_b, and hence the "blade wetted area", must be increased in order to maintain constant loading for fixed inlet and exit flow angles. The loss generated in the blade surface boundary layer was found to increase with increasing blade surface length, i.e. with increasing flow path length, in [**112**].

- ***Statement.*** **Premise P3.** In the case of straight blades, the intensification – or moderation – of radial outward flow results in increase – or decrease – of length L of flow paths.

Justification

The blade stacking line is the line connecting the centres of gravity of the individual blade sections fitting to cylindrical surfaces. Conventional "straight" blades are radially stacked, i.e. the stacking line is radial. The left-hand side sketch in **Figure 3.5** presents an example of a straight blade, exhibiting radial outward flow on the suction side. The sketch illustrates that the addition of radial outward flow to the fictitious 2D through-flow along a cylindrical stream surface – indicated by a dashed line – elongates the suction side streamline. The more intense the radial outward flow, the longer the flow path. Such a flow path-elongating effect is referred to (e.g.) in [**168**].

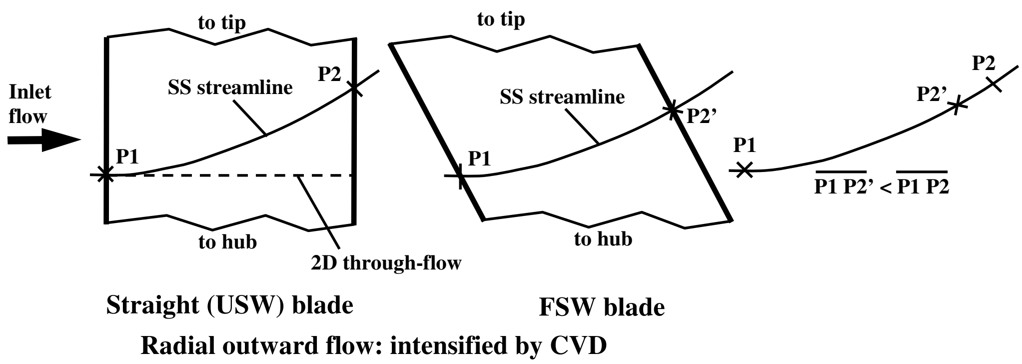

Figure 3.5. Shortening of flow path due to the combination of radial outward flow and FSW. SS: suction side.

- ***Statement.*** **Premise P4.** A consequence of CVD is intensified radial outward flow in the suction side boundary layer.

Justification

As [**154**] points out, in the case of non-free vortex flow, shed vorticity induces stream surface twist, producing opposite spanwise velocities on the two blade surfaces. Reference [**156**] states that radial transport dominates in the suction side boundary layer. Reference [**139**] provides a detailed analysis of the intensification of radial outward flow in the suction side boundary layer due to CVD. Such effect is pointed out via the experimental data in [**144**]. In simple words, such an effect – explained and illustrated in [**139**] in more detail – can be described as follows. Spanwise increasing blade circulation corresponds to vortices shed from the blade, according to Helmholtz's theorem [**143**]. The sense of rotation of these elementary shed vortices corresponds to radial outward and inward flows on the suction side and pressure side, respectively.

- ***Statement.*** **Conclusion C5.** $\begin{smallmatrix}\text{P3} & \text{P4}\\ \searrow & \swarrow\\ \multicolumn{2}{c}{\text{C5}}\end{smallmatrix}$ In the case of straight blades, CVD results in increase of flow path length *L* on the suction side.

- ***Statement.*** **Conclusion C6.** $\begin{smallmatrix}\text{C4} & \text{C5}\\ \searrow & \swarrow\\ \multicolumn{2}{c}{\text{C6}}\end{smallmatrix}$ In comparison to free vortex design, CVD applied to straight blades tends to represent an additional source of total pressure loss. This is due to elongation of the flow paths on the suction side, caused by intensified radial outward flow.

- ***Statement.*** **Premise P5.** Applying forward sweep to a rotor blading, exhibiting radial outward flow on the suction side, results in the decrease of flow path length *L*, relative to the case concerning the unswept – straight – blading.

Justification

The following sentences provide a brief reminder on former definitions. A blade is swept when the blade sections of a straight datum blade are shifted parallel to the chord. This results in a non-radial blade stacking line. A blade is of FSW – or backward sweep – if the sections of a straight datum blade are shifted parallel to their chord in such a way that the blade section under consideration is upstream – or downstream – of the neighbouring blade section at a lower radius. Reference [**4**] gives an overview of the potential aerodynamic benefits of various blade-stacking techniques comprising FSW. The drawings on the left- and right-hand side in **Figure 3.5** are sketches of comparative straight and FSW blades, respectively. As explained in [**31**], all rotor blades are subject to radially outward flow on the suction side. As [**31**] states, radially outward flow is primarily due to "radial centrifugation" of the fluid. Further causes for the intensification of radially outward flow – among the others, the effect due to CVD – are discussed in detail in [**139**]. According to [**31**], if backward sweep is used, the path of the boundary layer fluid becomes elongated, due to the longer path available before reaching the trailing edge. In contrast, FSW severely limits the range of radial travel of boundary layer fluid, by truncating the flow path near the trailing edge. Fig. 3.5 makes such an effect visible.

- ***Statement.*** **Conclusion C7.** $\begin{tikzcd}[row sep=tiny, column sep=tiny] C3 \arrow[dr] & & P5 \arrow[dl] \\ & C7 & \end{tikzcd}$ Applying FSW to a rotor blading, exhibiting radial outward flow on the suction side, results in the decrease of total pressure loss, provided that the adverse streamwise pressure gradient remains subcritical.

Justification

It has been outlined in [**31**] that, due to the effect formulated in Premise P5, the boundary layer on a FSW blade becomes thinner than that on a straight, unswept blade. Such thinning of turbulent boundary layer on FSW blades has also been referred to in [**74**] as a benefit, having the potential for reduction of broadband noise (boundary layer "self-noise"). In contrast, as stated in [**31**], boundary layers of backward-swept blades should be thicker than those of an unswept blade, since the outward-migrating boundary layer can move farther away due to a longer path being available before reaching the trailing edge.

- ***Statement.*** **Conclusion C8.** $\begin{tikzcd}[row sep=tiny, column sep=tiny] C6 \arrow[dr] & & C7 \arrow[dl] \\ & C8 & \end{tikzcd}$ The adverse effect of CVD described in Conclusion C6 can be counterbalanced by incorporation of FSW in CVD, provided that the adverse streamwise pressure gradient remains subcritical.

The case study in the next section will support this statement. Preliminary studies in [**159**] also indicated that a suitable combination of blade sweep and spanwise changing circulation results in a shortening of the flow path available to the trailing edge, leading to a moderation of loss.

Formula (3.5) summarizes the steps towards deriving Conclusions C6 to C8 – being the most important new statements made by the paper.

$$\begin{tikzcd}[row sep=small, column sep=tiny]
P1 \arrow[dr] & & P2 \arrow[dl] & & P3 \arrow[dr] & & P4 \arrow[dl] & & P1 \arrow[dr] & & P2 \arrow[dl] & & & \\
& C4 \arrow[drr] & & & & C5 \arrow[dll] & & & & C3 \arrow[drr] & & & & P5 \arrow[dll] \\
& & & C6 \arrow[drrrr] & & & & & & & & C7 \arrow[dllll] & & \\
& & & & & & & C8 & & & & & &
\end{tikzcd} \tag{3.5}$$

3.4. Application of FSW to a CVD rotor – a case study

The comparative CFD case study reported by Corsini and Rispoli in reference [**26**] is taken as the basis.

The study comprises straight – unswept (**USW**) – and FSW bladed high-pressure industrial axial fan rotors of CVD. Further information about this comparative case study is available in [**25, 95**]. The means of investigation is a highly efficient CFD technique incorporating anisotropic turbulence modelling. The reliability of the CFD tool is thoroughly reported in detail in [**26, 145**]. The rotor design and geometrical parameters are documented in detail in [**26, 144**], and therefore, only a brief account is given here. **Table 3.1** presents the main data commonly representative for the two rotors and relevant to this chapter. FSW has been re-cambered and re-staggered, attempting to retain the original performance of USW, as suggested in [**4**]. Possible discrepancies between the USW and FSW data are indicated as uncertainty ranges in the table. Streamlines passing the suction side close to the blade surfaces approximately at midspan and mid-chord will be studied. Therefore, quantitative data relevant to the midspan are presented for further discussion.

First, the relevance of the assumptions listed in Section 3.2 to this case study is commented on, referring to the data in Table 3.1.

- Isolated axial flow rotors, comprising circular arc-cambered blades with a thin profile of uniform thickness, are investigated, at the design flow rate.
- The Mach number relevant to the midspan, Ma_{mid}, was calculated on the basis of the design relative midspan flow velocity and the speed of sound in air at 20 °*C*. Its value implies the reasonability of the incompressible flow assumption.
- As an approximation to Eq. (G3) in Appendix G, the Reynolds number was calculated on the basis of the design relative midspan flow velocity, the length of blade chord fitting the cylindrical surface at midspan, and the kinematic viscosity of air at 20 °*C*. Re_{mid} significantly exceeds the critical range of $(1.5\div2.5)\cdot10^5$ [**74, 86, 110**].
- Given that the tip diameter, the hub-to-tip ratio and the blade count are equal for the two rotors, they have identical blade spacings.
- In the near-midspan region, the two rotors are characterised by nearly identical inlet and outlet flow angles. This is indicated by the axial velocity and swirl profiles in [**25-26, 95**]. The axial velocity and swirl are characterised by dimensionless pitch-averaged $\hat{\varphi}_2$ and $\hat{\psi}_2$ coefficients, respectively [**25-26, 95**]. Following the methodology in [**1, 164**], the representative axial flow coefficient as well as the inlet and outlet flow angles – taken at the cylindrical surface at midspan – were calculated as follows.

$$\hat{\varphi}_{12} = \frac{\hat{\varphi}_1 + \hat{\varphi}_2}{2} \text{ [1]} \tag{3.6a}$$

$$\alpha_1 = \tan^{-1}\frac{R}{\hat{\varphi}_{12}} \text{ (swirl-free inlet)} \tag{3.6b}$$

$$\alpha_2 = \tan^{-1}\frac{R - \hat{\psi}_2/2R}{\hat{\varphi}_{12}} \tag{3.6c}$$

Table 3.1. *Rotor operational and geometrical data* [**25-26, 95**]

N_b [-]	12	
ν_{ht} [-]	0.676	
r_t [m]	0.315	
S [m]	0.102	
$s_{b\,mid}$ [m]	0.138	
c_{mid} [m]	0.171	± 0.001
γ_{mid} [deg]	47.4	± 0.4
θ_{mid} [deg]	24.3	± 1.1
$(c/s_b)_{mid}$ [-]	1.235	± 0.005
AR [-]	0.597	
R_{mid} [-]	0.838	
n [1/min]	1100	
Φ_D [-]	0.5	
Ψ_D [-]	0.5	
Ma_{mid} [-]	0.103	
Re_{mid} [-]	$4.01 \cdot 10^5$	
$\hat{\varphi}_{1mid}$ [-]	0.495	
$\hat{\varphi}_{2mid}$ [-]	0.530	± 0.010
$\hat{\varphi}_{12mid}$ [-]	0.513	± 0.005
$\hat{\psi}_{2mid}$ [-]	0.630	± 0.020
$\alpha_{1\,mid}$ [deg]	58.5	± 0.2
$\alpha_{2\,mid}$ [deg]	42.0	± 0.5
D_{mid} [-]	0.452	± 0.015

In addition to the flow angle values presented in Table 3.1, fair agreement between the two rotors in respect of flow angle conditions is also confirmed by reference [**95**]. Here, the streamwise flow angle distributions are presented along the near-midspan, near-midchord 3D streamlines. On this basis, it is concluded that the inlet and outlet flow angles at the near-leading edge and near-trailing edge streamline sections are nearly identical for USW and FSW.

The table also presents the length of blade chord fitting to the cylindrical surface at midspan, as well as the solidity.

The nearly identical inlet and outlet conditions and the equal solidity values manifest themselves in a nearly equal D diffusion factor at midspan (Eq. 2.29), i.e. nearly equal diffusion effect, as also presented in [**26**].

Figure 3.6 presents the static pressure distribution as well as near-suction side streamlines for the two rotors, reproduced from [**26**]. The rotor suction surfaces are plotted in their meridional views. The limiting streamlines [**178**] under investigation, passing the suction side at near-midspan and near-mid-chord, are marked with bold lines. Although the scrutinized flow path for USW enters and exits the blade passage near the endwalls, it mainly proceeds through the passage away from the endwalls. Near-endwall loss-generating effects, such as near-hub separation, casing wall boundary layer, and tip leakage flow, can be clearly distinguished from the loss zone developing along the blade surface. This can be seen later in the loss coefficient plots in Fig. 3.8.

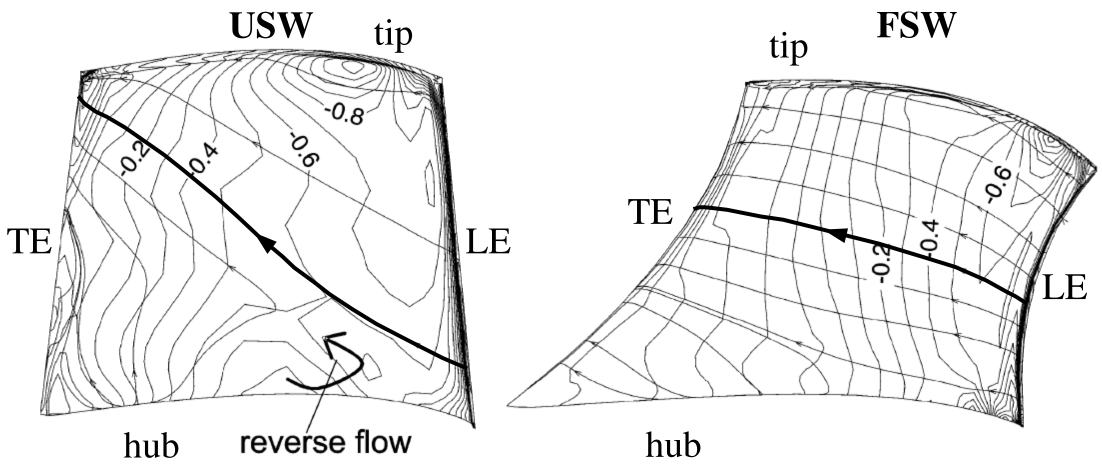

Figure 3.6. *Static pressure coefficient C_p distribution and streamlines on USW and FSW blades on the suction side* [**26**]. *The studied flow paths are indicated with bold lines. LE:leading edge. TE: trailing edge.*

As Fig. 3.6 suggests, the CVD concept in the case of the USW rotor results in a significantly elongated flow path compared to 2D through-flow, presenting a life-like proof for Conclusion C5. The departure from 2D through-flow results in a considerable increase of "effective chord length" [**168**] for the USW rotor. The blade chord corresponding to the fictitious 2D through-flow is 0.171 *m* (Table 3.1). Compared to this, the length of flow path investigated for USW suction side has an increased value, estimated to $L_{USW} = 0.207$ *m*, i.e. 21 % increase. Calculated with a midspan blade spacing of $s_{b\ mid} = 0.138$ *m*, this corresponds to an increased "effective solidity" of $L_{USW}/s_{b\ mid} = 1.500$, compared to the 2D case of $(c/s_b)_{mid} = 1.235$.

In contrast, in the FSW case, the radial outward flow applied to the CVD rotor has been attenuated due to forward sweep, as pointed out in [**139**]. In addition, the forward sweep angle of 35° has been set in such a way that the streamlines are approximately perpendicular to the leading edge and the trailing edge, thus realizing approximately the shortest available flow path along the blade surface. It can be seen with a single glance at Fig. 3.6 that the FSW flow path is considerably shorter than the USW one. The above effects result in the following estimated parameter values. $L_{FSW} = 0.153$ *m*, i.e. a decrease of 11 %, compared to the fictitious 2D blade chord of 0.171 *m*. The effective solidity is $L_{FSW}/s_{b\ mid} = 1.109$, lower than the 2D case of $(c/s)_{b\ mid} = 1.235$. Therefore, the effective solidity – i.e. the flow path length and the related total pressure loss – can even be reduced relative to the 2D case, by means of appropriate incorporation of FSW in CVD.

Fig. 3.6 presents the static pressure distribution in the form of contour plots of the C_p static pressure coefficient. C_p is obtained as local static pressure minus pitch-averaged mean static pressure at inlet at midspan, non-dimensionalised by the fictitious dynamic pressure calculated with rotor tip speed. Based on the figure, the local non-dimensional streamwise pressure gradient g has been obtained using numerical derivation as follows:

$$g_p = \frac{\partial C_p}{\partial (L/c_{\mathrm{mid}})} \tag{3.7}$$

where δL is the increment in the streamwise length coordinate along the studied flow path. **Figure 3.7** compares the estimated streamwise distribution of g_p for the two rotors. The horizontal axis presents the fraction of total flow path length L, i.e. 0 % and 100 % are assigned to the leading edge and trailing edge, respectively, for both rotors. Behaving as expected, FSW is characterised by a higher adverse pressure gradient – larger positive g_p values – along the dominant portion of the flow path. This is due to the fact that both rotors carry out approximately the same diffusion, but the studied available flow path is shorter for FSW.

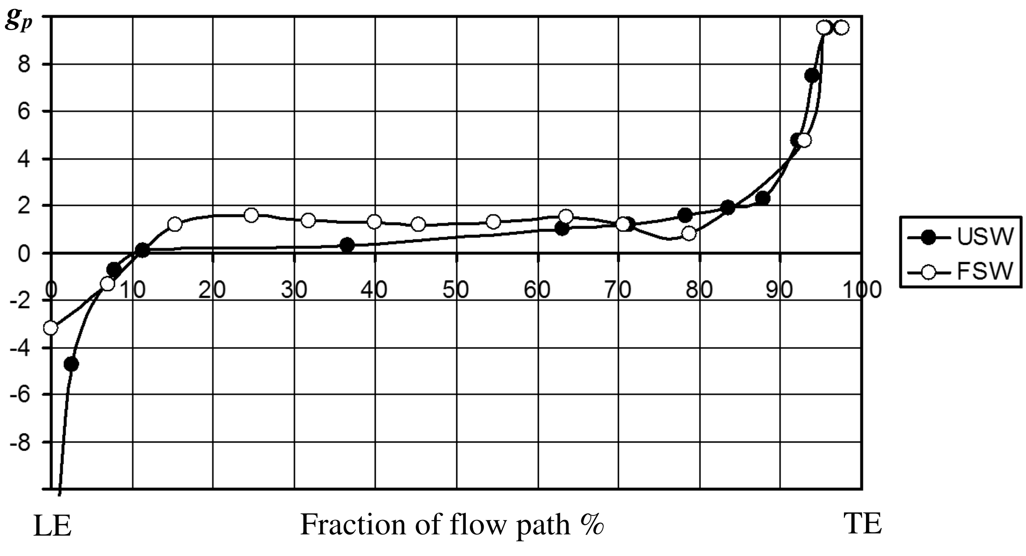

Figure 3.7. *Evolution of streamwise pressure gradient g_p along the flow paths. LE:leading edge. TE: trailing edge.*

It must be acknowledged that 2D cascade flow data cannot correspond perfectly to 3D rotor flows. Still, the following *brief* approximation will be presented herein. The post-processed 2D Lieblein data, specified in Eqs. (2.29) and (3.3) and in the related Fig. 3.4, will be considered. The loss-reducing potential for shortening the 3D flow paths by applying FSW to a USW rotor will be predicted on this 2D basis. To this end, conical surfaces fitting approximately to the investigated 3D suction side flow paths are considered. (This way of modelling will be referred to as quasi-three-dimensional approach in Chapter 4.) It is assumed that the elementary blade cascades fitting to these conical surfaces can be developed into 2D cascade planes. The related aerodynamic behaviour is studied on the basis of 2D cascade approach.

According to the flow angle data in Table 3.1, the diagram related to $\alpha_1 = 58.5°$ and $\alpha_2 = 42.0°$ in Fig. 3.4 can be assigned to the present case study. The uncertainty range of the total pressure loss coefficient – caused by propagation of the uncertainty of the flow angles included in Table 3.1 – is indicated approximately by the size of the marker symbols in Fig. 3.4. The diagram indicates the data points for the effective solidity values of $L_{FSW}/s_{b\ mid} = 1.109$, $(c/s_b)_{mid} = 1.235$, and $L_{USW}/s_{b\ mid} = 1.500$, using the labels FSW, 2D, and USW, respectively. According to the definitions in Eqs. (F3a) and (F3b) in Appendix F, the loss coefficient is derived using the absolute inlet velocity for the 2D linear cascade flow, and it is derived using the relative inlet velocity for the USW and FSW rotor flows. Fig. 3.4 suggests the following.

- The case study is in the subcritical adverse streamwise pressure gradient range, i.e. the FSW, 2D, and USW data points correspond to solidity values higher than the solidity related to minimum loss, ω_{min}. This suggests that loss reduction may be expected from the FSW blade, in spite of the increased streamwise pressure gradient indicated in Fig. 3.7.
- The loss data indicated in Fig. 3.4 – together with other data of the flow path analysis – are presented in **Table 3.2**, and are labelled as "2D approach". The uncertainty of the data is also included in the table. The difference $\omega_{USW} - \omega_{FSW}$ is one order of magnitude larger than the uncertainty in ω. Therefore, the predicted loss-reducing effect is judged to be of significance from the viewpoint of detectability. As the ω data imply, an approximate loss reduction of 16 % is predicted for the FSW flow path under interrogation, relative to the USW case. Considering the nearly linear trend of the diagrams in the studied range in Fig. 3.4, each reduction of 10 % in flow path length is predicted to result in an approximate loss reduction of 4 %.

***Table 3.2**. Results of flow path analysis*

	USW	2D	FSW	
Flow path length	$L_{USW} = 0.207\ m$	$c_{mid} = 0.171\ m$	$L_{FSW} = 0.153\ m$	$\pm 0.002\ m$
Effective solidity	$L_{USW}/s_{mid} = 1.500$	$(c/s)_{mid} = 1.235$	$L_{FSW}/s_{mid} = 1.109$	± 0.01
ω loss coefficient: 2D approach	0.032	0.029	0.027	± 0.0005
ω loss coefficient: 3D approach	0.041	-	0.029	± 0.003

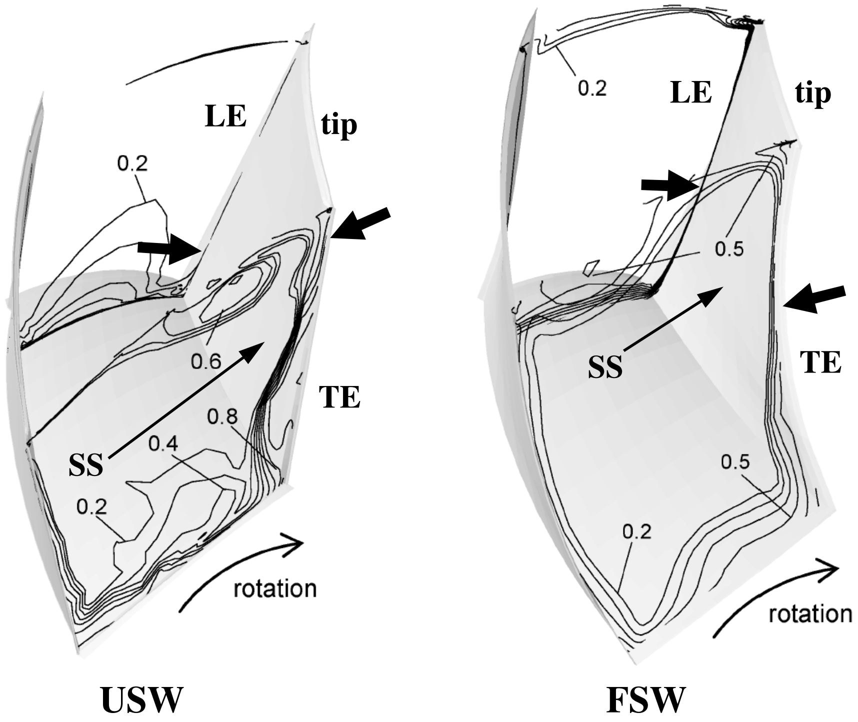

Figure 3.8. *Evolution of total pressure loss coefficient* ω_{loc} *inside the blade passages at 10 % and 98 % blade chord* [**26**]. *The location of entrance and exit of the studied flow paths is indicated by bold arrows. LE:leading edge. TE: trailing edge. SS: blade suction side.*

The above findings were then correlated with the 3D CFD data published in [**26**]. **Figure 3.8** shows the evolution of the local total pressure loss coefficient ω_{loc} inside the blade passages. Instead of the mass-averaging taken in Eqs. (F3a) and (F3b) in Appendix F, the local total pressure is considered in ω_{loc}, but the same normalization method is applied. ω_{loc} contour plots are presented at the 10 % and 98 % midspan chord positions. The location of the investigated suction side flow paths (see Fig. 3.6) near the leading edges and trailing edges are indicated in Fig. 3.8 by bold arrows. At the near-leading edge section of the studied flow path, the FSW rotor exhibits a higher loss. This probably corresponds to the higher initial pressure gradient (see Fig. 3.7). However, at the near-trailing edge section of the same flow path, the FSW rotor is characterised by thinned suction side boundary layer, and lower loss. The loss reduction is attributed to a shortening of the flow path. The thinning of the turbulent boundary layer in the FSW rotor is also clearly visible on the turbulence intensity contour plots in [**26**]. This is in accordance with the recommendation in [**74**] that the turbulent boundary layer flow be controlled by forward sweep. Boundary layer thinning is visible for FSW not only in the vicinity of the near-trailing edge section of the studied flow path, but also at higher and lower radii, just in the region where a systematic shortening of flow paths can be observed in Fig. 3.6. For comparison with ω data obtained on the basis of the 2D cascade approach (Fig. 3.4, Table 3.2), the loss data in [**26**] were processed. The total pressure loss in the boundary layer developing on the blades at 98 % chord at the exit radius of the suction side flow path has been pitch-averaged. Table 3.2 includes the resultant ω data with the label "3D approach". For the 3D approach, the estimated uncertainty of ω is considerably higher than for the 2D approach, mainly due to the approximative manner of numerical integral-averaging along the pitch. The loss-reducing trend due to flow path shortening shows fair agreement for both the 2D and 3D approaches.

As Table 3.2 suggests, despite the applied simplifications and assumptions, the 2D approach, based on the Lieblein cascade data, is introduced as a preliminary design tool for the prediction of order of magnitude of the following quantities. 1) Total pressure loss developing along the 3D rotor flow paths. 2) Reduction of total pressure loss via shortening of the flow paths, e.g. by applying FSW to a rotor of CVD. In the 3D case study based on [**26**], the ω values are somewhat higher than those predicted by the 2D approach. The probable main reason for this is that the profile loss for the blades in [**26**], i.e. circular arc-cambered blades with a thin profile of uniform thickness, is higher than that for the *C4* and NACA profiles in [**110**] (conf. Fig. 3.3). The 2D approach underestimates the loss reduction observed in the present case study. As the data imply, even higher loss reduction can be achieved by applying FSW. The beneficial effects of FSW resulted in a total efficiency gain of order of magnitude of 2 % in [**26**]. The literature survey in [**4**] suggests that an efficiency gain of 2-3 % can be achieved at the design point by suitable application of FSW.

The trends outlined in the chapter are to be quantified by means of extensive CFD campaigns for particular design assignments. Reference [**170**] gives one example of CFD-based iterative combination of CVD with FSW.

3.5. NEW SCIENTIFIC RESULTS [4, 160]

Thesis point 4 [**160**] The author has post-processed and evaluated literature data on diffuser flows of various levels of complexity in a comprehensive manner. The studies incorporated Q1D (conical diffuser), 2D (linear blade cascade) and 3D (annular blade cascade) flows. The inlet and outlet geometrical and velocity conditions were considered as fixed for each comparative study. The author has drawn the following common conclusion for each type of flow. The consequence of decreasing the flow path length along the wall is to decrease the total pressure loss – due to moderating the effect of wall skin friction –, provided that the adverse streamwise pressure gradient remains below a critical value.

Thesis point 5 [**160**] The linear cascade studies published by Lieblein [**110**] were re-interpreted by the author. On this basis, the author has elaborated a method for estimating the total pressure loss as well as its modification due to a change of flow path length along the blade, in blade cascade flows. Using this method in preliminary blade design, it can be predicted in which solidity range and to what extent one may expect loss reduction by reducing the flow path length, i.e. by reducing the effective blade chord length, for prescribed inlet and outlet flow angles and fixed blade spacing.

Thesis point 6 [**4, 160**] The author has pointed out that, in comparison to free vortex design, CVD applied to straight axial flow rotor blades tends to represent an additional source of total pressure loss farther from the endwalls. The cause is the elongation of the flow paths along the blade suction side – and thus, increase of effect of wall skin friction –, due to intensified radial outward flow. The author has established that this adverse effect can be moderated by the incorporation of FSW in CVD, via shortening the flow paths on the suction side, while retaining the inlet and outlet velocity conditions. On this basis, the author concluded as follows. The benefit of FSW, in terms of moderating loss *away from the endwalls*, can be better utilised for the rotors of CVD, in comparison to free vortex design. This statement adds to Thesis point 3, also discussing the especial benefits of FSW applied to CVD rotors, but only in moderating loss *near the tip*.

4. INCORPORATION OF FSW IN PRELIMINARY CVD

4.1. Introduction

It has been pointed out in the previous chapters that FSW is especially beneficial for the rotors of CVD, in terms of moderating loss near the tip [**139**] (Chapter 2) as well as away from the endwalls [**160**] (Chapter 3).

The following abbreviations are used in this chapter in the flow modelling approaches:

- **2D**: two-dimensional flow in a rectilinear cascade,
- **Q2D**: quasi-two-dimensional modelling approach applied to an elementary annular (cylindrical) rotor cascade of constant middle radius, by neglecting the radial flow, and assuming the adaptability of 2D cascade correlations,
- **Q3D**: quasi-three-dimensional modelling approach applied to an elementary conical rotor cascade, and assuming the adaptability of 2D cascade correlations,
- **3D**: fully three-dimensional rotor blade passage flow.

In Chapter 3, the literature survey implied that most loss is generated in the blade suction side boundary layer away from the endwalls. Therefore, the control of loss generated along the suction side flow paths is of primary interest in blade design.

In the case study in Chapter 3, 3D flow paths on the suction side of blade of CVD rotors were investigated away from the endwalls. Conical surfaces approximately fitting these flow paths were considered. As a brief approximation, it was assumed that the elemental blade cascades fitting these conical surfaces can be developed into 2D cascade planes. Accordingly, the development of total pressure loss along the 3D suction side flow paths was studied on the basis of a Q3D cascade approach, utilising 2D cascade data [**110**]. It was found that the loss developing along the suction side flow paths can be moderated by applying FSW, due to flow path shortening. The Q3D cascade approach was introduced as a tool for estimating the order of magnitude of the total pressure loss along the 3D rotor flow paths, as well as its reduction via flow path shortening due to FSW.

The aforementioned results are in accordance with a new concept incorporating FSW in *preliminary* CVD. The main features of the proposed new concept are listed below.

1) *The proposed concept supplements the widespread Q2D approach that is used extensively in preliminary CVD.* As noted in [**112, 157**], the early stages of blade design are still often done on a 2D basis. The Q2D approach is frequently applied even being aware that blade sweep and/or spanwise changing design blade circulation introduce 3D effects [**2, 4**]. As referred to in [**112**], it is stated in the classic work [**2**] that a 2D approach can be correctly employed for a plane perpendicular to the stacking axis of a swept blade of infinite span. Recently, paper [**112**] presented a simple method for estimating the change in blade boundary layer loss with sweep – in a 2D

aerodynamic loss approach. In preliminary CVD, the Q2D approach has been used in the past decades, and is used even nowadays, as for the fans reported e.g. in [**1, 37-38, 59, 72, 74, 79, 104, 178, 189**], occasionally regarding blades featuring sweep as well.

2) *The concept combines the Q2D approach with a Q3D approach.* In the Q3D approach, the elementary – conical – blade sections are designed as ones fitting the 3D streamlines on the suction side. By such combination, the concept provides a design tool enabling loss moderation along the 3D suction side flow paths, while simultaneously retaining the main features of the Q2D approach. Therefore, the concept contributes to satisfying the need formulated by Cumpsty [**157**] as follows: "Now full 3D calculations (…) are possible (…) – almost anything can be calculated, given the commitment of computer resources, but understanding of the 3D behaviour remains a challenge. (…) There is a related problem: how to turn knowledge about 3D flow into useful guidelines for assessing aerodynamic behaviour."

3) *The concept relies on traditional 2D cascade measurement data*, e.g. [**72, 105, 108, 110, 179**]. Classic empirical 2D cascade correlations are used even very recently in preliminary blade design, e.g. [**187-188**]. Correlations by Howell are of frequent use, e.g. [**72, 178, 185-187**]. As a representative choice, empirical correlations by Howell are used in the present paper. However, this choice means no restriction in using the concept incorporating other empirical databases.

4) *A key issue in the concept is determining the optimum blade solidity, separately in the Q2D and Q3D approaches.* Correlations by Howell [**179**], cited in [**72**], provide a convenient tool for this purpose. Howell's data are used to this day for obtainment of optimum solidity [**187**]. It is noted, however, that the optimum solidity can be estimated using other databases as well, as demonstrated in [**72, 160**].

5) *At a given mean radius of a rotor of CVD, the optimum solidity has been found to be lower in the Q3D approach than that in the Q2D approach. FSW offers a unique means for simultaneous realisation of such different optimum solidities in one blade geometry. Accordingly, FSW is quantified in the concept as being favourable for a rotor of CVD.* The corresponding sweep angle distribution is therefore *an output*, i.e. *a result*, of the proposed preliminary CVD process. This provides a new design feature in comparison to the literature. In contrast to the concept presented herein, reports on axial flow rotors of CVD usually consider sweep as a *design input*, i.e. a feature *prescribed* arbitrarily by the designer. The favourable stacking line geometry is then sought by means of testing various CVD rotors of blade sweep prescribed in an arbitrary manner, as in the research programs reported e.g. in [**18-19, 21, 37-38, 43, 154-155, 158, 191**].

6) *For brief estimation of the 3D suction side flow paths, forming the basis of the Q3D approach, CFD is applied to the preliminary blade geometry.* Such use of CFD in early stages of design is suggested e.g. in [**157**].

7) *The concept serves only for the preliminary design of blade geometry away from the endwalls – where the Q2D and Q3D approaches are presumed to be applicable* [**112, 157**]. In addition to FSW, incorporation of dihedral (lean) in blade stacking is also discussed in the paper. The final blade geometry, optionally including both sweep and dihedral, can be obtained via refinements using fully 3D, CFD-based methods, as proposed e.g. in [**157, 191**]. In the near-endwall region, 3D considerations are to be made in final design. For example, near the hub, not FSW but backward sweep – corresponding to positive sweep – is found to be beneficial [**4**]. However, such refinements are beyond the scope of the *preliminary* design method proposed herein.

8) In addition to the assumptions and restrictions listed in Section 1.2, the design method outlined herein is proposed for CVD rotors of relatively large spanwise gradient of blade circulation, exhibiting pronounced radial outward flow on the suction side.

The 2D cascade concept, as well as Q2D and Q3D approaches of rotor flow, is outlined first. Then, descriptive relationships for rotor flows are discussed, in comparison between the Q2D and Q3D approaches. The preliminary blade design procedure is outlined, with the innovative incorporation of FSW. Finally, a design case study is presented, supporting the appropriateness of the proposed concept.

The outline as well as preliminary details of the design concept proposed herein by the author were published in [**4, 95, 170, 173-176, 190**].

4.2. 2D cascade concept; Q2D and Q3D rotor flow approaches

4.2.1. 2D concept

In this section, the chosen empirical 2D cascade correlation, as well as its physical relevance to the proposed design concept, is presented.

As noted earlier, a key issue of the proposed design concept is determining the optimum blade solidity. The optimum solidity can be determined either directly from Howell's 2D cascade correlations ([**179**], cited in [**72, 87**]), or indirectly, using other cascade databases [**72, 160**], as function of inlet and outlet flow angles. In the process of obtaining the optimum solidity, the blade section lift coefficient is incorporated herein as *auxiliary data*, for lifelike interpretation of blade load. Classic lift coefficients are used even nowadays as lifelike approximate indicators of blade load [**1, 17, 27, 74, 112, 164, 178, 186, 188**].

Details on the 2D concept are outlined in **Appendix J**. For explanation of pitch-averaging applied for the various quantities, **Appendix K** is referred to.

Combining the expression for the blade circulation as function of blade spacing and change in pitchwise velocity, Bernoulli equation, Kutta-Joukowski theorem, and definition of lift coefficient, [**1**], leads to the following statement. Details on obtaining Eq. (4.1), and definitions of lift and drag coefficients, are given in **Appendix L**. The isentropic static pressure rise through a 2D cascade is directly proportional to the product of blade solidity and lift coefficient; for fixed density, mean flow velocity, and mean flow angle:

$$\Delta p_{\mathrm{is}} = \frac{c}{s_{\mathrm{b}}} C_{\mathrm{L}} \rho \frac{\hat{v}_{\infty}^2}{2} \sin \alpha_{\infty} \tag{4.1}$$

Dividing Eq. (4.1) by the chord length c implies $(\Delta p_{\mathrm{is}}/c) \sim C_{\mathrm{L}}$ for fixed blade spacing, density, and mean flow characteristics. By such means, it is demonstrated that C_{L} is a lifelike indicator of the chordwise mean adverse pressure gradient, approximated as $(\Delta p_{\mathrm{is}}/c)$.

Let us consider a series of consecutive blades of number N_{b}, having a fixed pitchwise extension $s_{\mathrm{b}}N_{\mathrm{b}}$. The solidity in Eq. (4.1) can be written as $c/s_{\mathrm{b}}=(cN_{\mathrm{b}})/(s_{\mathrm{b}}N_{\mathrm{b}})$, where cN_{b} approximates the sum of "blade wetted length" [**160**] through the blade series. If Δp_{is} is prescribed, Eq. (4.1) indicates the following trends.

- Increasing C_{L} tends to increase the adverse pressure gradient but tends to decrease the blade wetted length cN_{b} – the latter moderates the effect of skin friction.
- In contrast, decreasing C_{L} tends to decrease the adverse pressure gradient but tends to increase the blade wetted length – the latter increases the effect of skin friction.
- The above imply the existence of an optimum solidity $(c/s_{\mathrm{b}})_{\mathrm{opt}}$, associated with an optimum lift coefficient C_{Lopt}, for minimising the total pressure loss [**160**].

In what follows, an approximate correlation, enabling a simple mathematical treatment, is sought for C_{Lopt}. Let us assume that prescribed Δp_{is} in Eq. (4.1) is obtained at a C_{Lopt} value. Then, the isentropic static pressure rise is intended to be increased by increasing the solidity: $\partial(\Delta p_{\mathrm{is}})/\partial(c/s_{\mathrm{b}})>0$. According to the *chain rule*,

$$\frac{\partial(\Delta p_{\mathrm{is}})}{\partial(c/s_{\mathrm{b}})} = \frac{\partial(\Delta p_{\mathrm{is}})}{\partial C_{\mathrm{Lopt}}} \cdot \frac{\partial C_{\mathrm{Lopt}}}{\partial(c/s_{\mathrm{b}})} > 0 \tag{4.2}$$

Increasing the solidity tends to increase the interference of the adjoining blades on the flow around a blade, and thus, tends to reduce the lift coefficient, e.g. [**1**]. Therefore, $\partial C_{\mathrm{Lopt}}/\partial(c/s_{\mathrm{b}}) < 0$ is presumed. This implies via relationship (4.2) that $\partial(\Delta p_{\mathrm{is}})/\partial C_{\mathrm{Lopt}}<0$: increasing the static pressure rise tends to lessen C_{Lopt}. This statement is in accordance with reference [**72**] remarking that the greater the static pressure rise, the smaller is the permissible C_{L}. The isentropic total pressure rise can be expressed using the Bernoulli equation as follows.

$$\Delta p_{\mathrm{is}} = \rho\left(\frac{\hat{v}_1^2}{2} - \frac{\hat{v}_2^2}{2}\right) = \rho\frac{\hat{v}_1^2}{2}\left[1-\left(\frac{\hat{v}_{z12}/\cos\alpha_2}{\hat{v}_{z12}/\cos\alpha_1}\right)^2\right] = \rho\frac{\hat{v}_1^2}{2}\left[1-\left(\frac{\cos\alpha_1}{\cos\alpha_2}\right)^2\right] \tag{4.3}$$

The result $\partial(\Delta p_{is})/\partial C_{Lopt}<0$, together with Eq. (4.3), allows for the following approximation: C_{Lopt} increases monotonously with $(\cos\alpha_1/\cos\alpha_2)^2$. Introducing a generalized power exponent $B_{CL} > 0$ instead of the value of 2 in Eq. (4.3), and taking direct proportionality, using a factor $A_{CL} > 0$, as the simplest mathematical approach, C_{Lopt} is approximated herein using the following formula:

$$C_{\mathrm{Lopt}} = A_{CL} \cdot \left(\frac{\cos\alpha_1}{\cos\alpha_2} \right)^{B_{CL}} \tag{4.4}$$

This approximation is consistent with the empirical cascade correlation reported in [**179**], and referred to in [**72, 87**] – termed herein as Howell's correlation –; with the cascade correlations by Carter [**72**]; and with [**110**]. For the Howell's correlation, A_{CL} = 2 and B_{CL} = 2.75 are specified in [**72, 87**], for the solidity range (c/s_b) of 0.6 to 2.

The relationship in Eq. (4.4) manifests herein the adaptation of experimental 2D cascade data to rotor flow. For rotor Q2D as well as Q3D approaches, the optimum solidity is approximated in the thesis via C_{Lopt} with use of formula (4.4), in which, however, the flow angles are calculated not with *absolute* but with *relative* velocities.

4.2.2. Q2D approach

As discussed in [**139, 160**], significant radial velocities may develop in a CVD rotor. However, in the Q2D CVD rotor approach, the radial flow is neglected. Fictitious stream tubes of constant middle radius r_{12} – termed herein as cylindrical stream tubes – are assumed through the rotor along the z axis, as illustrated in **Figure 4.1**. It is assumed in the Q2D approach that the elementary annular cascade enclosed in a cylindrical stream tube can be developed into a 2D cascade plane. Accordingly, the preliminary Q2D blade design relies on a 2D experimental database. Further details and examples on application of Q2D approach in preliminary CVD are published e.g. in [**1, 37-38, 59, 72, 74, 79, 104, 178, 189**].

Further notes on both Q2D and Q3D approach are given in **Appendix M**.

4.2.3. Q3D approach

A comprehensive overview on Q3D – axisymmetric – design approaches is given in reference [**1**]. In the Q3D approach used herein, the elementary blade cascade under consideration is enclosed between neighbouring *conical* surfaces of mean cone half-angle β, as shown in Fig. 4.1. The elementary conical cascade is characterised by radii r_1 and r_2 at the blade leading edge and trailing edge, respectively. Since the Q3D blade design approach is intended to control the loss generated along the suction side flow paths, the β values are to be set by such means that the conical surfaces approximately fit the *limiting streamlines* [**182**] on the suction side.

The local yaw angle of the limiting streamlines, ε_L, is defined as follows (conf. [**183**], and Figs. 2.1., 2.2.):

$$\varepsilon_L = \tan^{-1}\left[\lim_{n\to 0}(w_r/w_s)\right] \tag{4.5}$$

The representative mean $\tilde{\varepsilon}_L$ value along a suction side streamline under consideration is approximated on the basis of CFD (e.g. [**26**]). The cone half-angle is then calculated as

$$\beta = \tan^{-1}\left[\tan\tilde{\varepsilon}_L/\cos\gamma_{12}\right] \tag{4.6}$$

Where γ_{12} is the stagger angle at mean radius $r_{12} = (r_1+r_2)/2$.

The mean radial velocity is approximated through the blade passage as $v_r \approx \hat{v}_{z12}\tan\beta$.

Despite the presence of 3D flow, the adaptability of the 2D concept is assumed in the Q3D approach, as well as it was accepted in the Q2D approach, as e.g. in [**1, 37-38, 59, 72, 74, 79, 104, 178, 189**]. Thus, it is assumed in the Q3D approach that the elementary conical cascade can be developed into a 2D cascade plane, and can therefore be designed using a 2D database. This assumption is supported by the case study in [**160**], see Chapter 3.

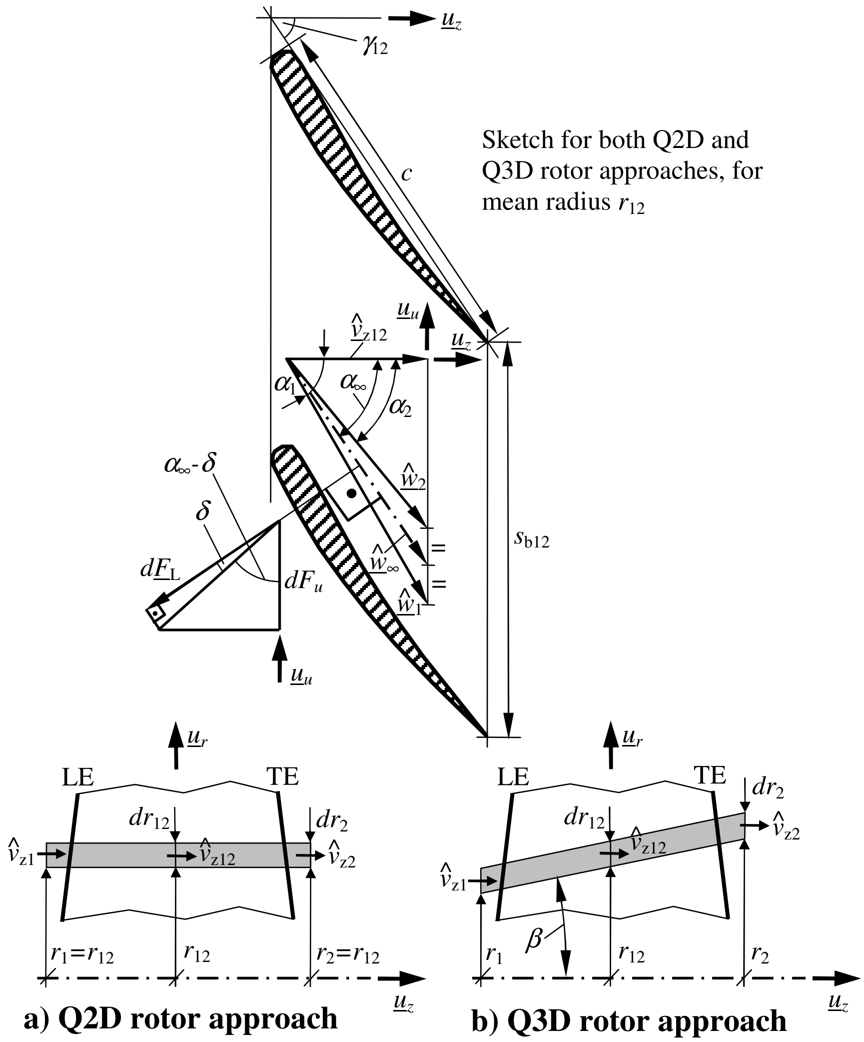

Figure 4.1. *Comparative sketches on Q2D and Q3D approaches. LE: leading edge. TE: trailing edge.*

4.3. Outline of blade design

4.3.1. Relationships describing rotor flows

Let us consider a Q2D (cylindrical) and a Q3D (conical) elementary cascade of equal mean radius r_{12} within the same rotor (Fig. 4.1). The optimum solidities will be approximated for both of them on the basis of 2D cascade data. Characteristics in the Q3D and Q2D approach will be denoted with subscripts for a clear distinction.

The same functions will be used for both approaches for describing the radial distributions of $\hat{\psi}_2$ and $\hat{\varphi}_2$. R_{12} is equal, but the inlet and outlet radii, R_1 and R_2, are different for the two approaches. Accordingly, $\hat{\varphi}_2(R_2), \hat{\varphi}_{12}(R_{12})$, and $\hat{\psi}_2(R_2)$ are also different for a cylindrical and for a conical elementary cascade of equal R_{12}.

Relationships valid in both Q2D and Q3D approach. As suggested by e.g. reference [**1**], the axial velocity through an elementary cascade is represented by an inlet-to-outlet arithmetic mean value, i.e.

$$\hat{\varphi}_{12}(R_{12}) = \frac{\hat{\varphi}_1(R_1) + \hat{\varphi}_2(R_2)}{2} \tag{4.7}$$

As an approximation for the fulfilment of conservation of mass through the elementary cascade, $\hat{\varphi}_{12} R_{12} dR_{12} \approx \hat{\varphi}_2 R_2 dR_2$ is taken into account.

The z-wise component of the angular momentum equation applied in the absolute frame of reference, to the control volume enclosing the elementary cascade, takes the following approximate form (conf. e.g. [**1, 74**]). Comments on obtaining Eq. (4.8) are given in Appendix M.

$$2 r_2^2 \pi \, dr_2 \, \rho \hat{v}_{z2} \hat{v}_{u2} = dM_z \tag{4.8}$$

The spanwise distribution of outlet axial velocity appearing in Eq. (4.8) is approximated with numerical integration of the simplified radial equilibrium equation, the use of which is suggested by references [**1, 74, 185**] for general whirl distribution, i.e. including CVD:

$$\left(\eta_t - \frac{\hat{\psi}_2}{2R_2^2}\right)\frac{d\hat{\psi}_2}{dR_2} = \frac{d}{dR_2}\left(\hat{\varphi}_2^2\right) \tag{4.9}$$

In the above equation, the kinetic energy related to the outlet radial velocity has been neglected in comparison to those related to the other outlet velocity components. Furthermore, the local total efficiency η_t [**164**] is taken herein as constant along the span. This simplifying assumption, suggested in [**74**], and supported by references [**27, 38, 122, 164**], is reasonable in the region away from the endwalls, to which the approach presented herein is anyway restricted.

Various styles for prescribing the radial distribution of the isentropic total pressure rise $\hat{\psi}_2(R_2)$ incorporated in Eq. (9), being a main feature of the CVD concept, are summarized e.g. in

[**1, 74**]. The power function $\hat{\psi}_2(R_2)$ distribution, utilized e.g. in [**26, 59, 79-81, 84-86, 144-145**], and specified in the following equation is taken herein as example. This choice means there is no restriction to introducing other $\hat{\psi}_2(R_2)$ distributions in the presented concept.

$$\hat{\psi}_2(R_2) = \hat{\psi}_2(\nu_{\mathrm{ht}}) \cdot \left(\frac{R_2}{\nu_{\mathrm{ht}}}\right)^m \tag{4.10}$$

Appendix N delivers information on the way of obtaining Eq. (4.9), the integral conditions related to the $\hat{\psi}_2(R_2)$ and $\hat{\varphi}_2(R_2)$ distributions, as well as expression of global total efficiency $\overline{\eta}_{\mathrm{t}}$.

Relationships valid for the Q3D approach. The flow angles are obtained using the following equations, which consider that the meridional mean velocity is approximated as $\hat{\varphi}_{12}/\cos\beta$ (Fig. 4.1).

$$\alpha_{1\,\mathrm{Q3D}} = \tan^{-1}\left(\frac{R_{1\,\mathrm{Q3D}}}{\hat{\varphi}_{12\,\mathrm{Q3D}}/\cos\beta}\right)\text{(swirl-free inlet)} \tag{4.11a}$$

$$\alpha_{2\,\mathrm{Q3D}} = \tan^{-1}\left(\frac{R_{2\,\mathrm{Q3D}} - \hat{\psi}_{2\,\mathrm{Q3D}}/2R_{2\,\mathrm{Q3D}}}{\hat{\varphi}_{12\,\mathrm{Q3D}}/\cos\beta}\right) \tag{4.11b}$$

The free-stream relative velocity is as follows:

$$(w_\infty/u_{\mathrm{t}})_{\mathrm{Q3D}} = \left\{\hat{\varphi}^2_{12\,\mathrm{Q3D}}\left(1+\tan^2\beta\right) + \left[R_{12} - \hat{\psi}_{2\,\mathrm{Q3D}}/\left(4R_{2\,\mathrm{Q3D}}\right)\right]^2\right\}^{1/2} \tag{4.12}$$

In the above equation, the square of the meridional velocity component has been characterised by $\hat{\varphi}^2_{12}\left(1+\tan^2\beta\right)$. Furthermore, the arithmetic mean value for the relative inlet and outlet tangential velocities – of R_1 and $R_2 - \hat{\psi}_2/2R_2$, respectively – has been taken into account.

The free-stream flow angle is calculated as

$$\alpha_{\infty\,\mathrm{Q3D}} = \cos^{-1}\left[\frac{\hat{\varphi}_{12\,\mathrm{Q3D}}/\cos\beta}{(w_\infty/u_{\mathrm{t}})_{\mathrm{Q3D}}}\right] \tag{4.13}$$

The elementary z-wise torque reacting on the elementary cascade, dM_z, included in Eq. (4.8), can be expressed in another way as follows (upper part of Fig. 4.1).

$$dM_{z\,\mathrm{Q3D}} = N_{\mathrm{b}}\, r_{12}\, (dF)_{u\,\mathrm{Q3D}} \tag{4.14}$$

Where the tangential component of elementary blade force is approximated as

$$(dF)_u = (dF_{\mathrm{L}}/\cos\delta)_{u\,\mathrm{Q3D}} = C_{\mathrm{L\,Q3D}}\,\rho\frac{w^2_{\infty\,\mathrm{Q3D}}}{2}\left(c_{\mathrm{Q3D}}\,dr_{12\,\mathrm{Q3D}}\cos\beta\right)\frac{\cos\left(\alpha_{\infty\,\mathrm{Q3D}} - \delta_{\mathrm{Q3D}}\right)}{\cos\delta_{\mathrm{Q3D}}} \approx$$

$$\approx C_{\mathrm{L\,Q3D}}\,\rho\frac{w_{\infty\,\mathrm{Q3D}}}{2}\hat{v}_{z12\,\mathrm{Q3D}}\,c_{\mathrm{Q3D}}\,dr_{12\,\mathrm{Q3D}} \tag{4.15}$$

In Eq. (4.14), the elementary blade force is modelled as a force concentrated on the mean radius of the elementary blade section, r_{12}. In Eq. (4.15), it has been considered that the surface of an elementary blade section between the conical surfaces of half-angle β and radial distance dr_{12} is $c_{Q3D}\, dr_{12} \cos\beta$. c_{Q3D} is the „effective chord length" fitting the cone of half-angle β. Furthermore, the approximations $\cos\delta \approx 1$ and $\alpha_\infty >> \delta$ have been made herein, for a simpler interpretation. (However, these approximations can be omitted in a more detailed design process.) These approximations are supported (e.g.) by [**74, 87, 184**]. Finally, $w_{\infty\,Q3D} \cos\alpha_{\infty\,Q3D} = \hat{v}_{z12\,Q3D} / \cos\beta$ was considered, using Eq. (4.13).

Combining Eqs. (4.8) and (4.14), considering the conservation of mass via $\hat{\varphi}_{12} R_{12} dR_{12} \approx \hat{\varphi}_2 R_2 dR_2$, and substitution of mean blade spacing $s_{b\,12} = 2\, r_{12}\, \pi \,/\, N_b$ gives the "fundamental cascade equation" of the elementary cascade (conf. [**74**]):

$$C_{L\,Q3D} \left(\frac{c}{s_{b\,12}} \right)_{Q3D} = \frac{r_{2\,Q3D}}{r_{12}} \frac{2\, \hat{v}_{u2\,Q3D}}{w_{\infty\,Q3D}} \tag{4.16a}$$

In dimensionless form:

$$C_{L\,Q3D} \left(\frac{c}{s_{b\,12}} \right)_{Q3D} = \frac{R_{2\,Q3D}}{R_{12}} \frac{\hat{\psi}_{2\,Q3D} / R_{2\,Q3D}}{\left\{ \hat{\varphi}^2_{12\,Q3D} \left(1 + \tan^2\beta\right) + \left[R_{12} - \hat{\psi}_{2\,Q3D} / \left(4 R_{2\,Q3D}\right) \right]^2 \right\}^{1/2}} \tag{4.16b}$$

Relationships valid for the Q2D approach. Substituting $R_1 = R_2 = R_{12}$ and $\beta = 0$ into Eqs. (4.11) to (4.16), and taking

$\hat{\varphi}_2(R_{12})$, $\quad \hat{\varphi}_{12}(R_{12}) = [\hat{\varphi}_1(R_{12}) + \hat{\varphi}_2(R_{12})]/2$, and $\quad \hat{\psi}_2(R_{12})$, instead of

$\hat{\varphi}_2(R_2)$, $\quad \hat{\varphi}_{12}(R_{12}) = [\hat{\varphi}_1(R_1) + \hat{\varphi}_2(R_2)]/2$, and $\quad \hat{\psi}_2(R_2)$, respectively,

formulae well-known in axial fan design based on the Q2D approach (e.g. fundamental cascade equation in [**74, 87**]) are obtained. These formulae are presented in **Appendix P**.

4.3.2. Preliminary CVD procedure

Design based on the Q2D approach. For correction, the design process may return from a given step to a previous one, within an iterative procedure. ***1a)*** Values for Φ, Ψ, $\overline{\eta}_t$ [**164**], and ν_{ht} are taken as initial input data. ***1b)*** An inlet condition $\hat{\varphi}_1(R_1)$ is prescribed. ***1c)*** An initial $\hat{\psi}_2(R_2)$ distribution is prescribed, e.g. on the basis of Eq. (4.10). ***1d)*** An initial $\hat{\varphi}_2(R_2)$ distribution is calculated on the basis of Eq. (4.9), for which a representative η_t value is chosen. ***1e)*** The $\hat{\psi}_2(R_2)$ and $\hat{\varphi}_2(R_2)$ distributions are refined, in order to match with the integral conditions represented by Φ, Ψ, and $\overline{\eta}_t$ (conf. [**74**]), as well as to control the diffusion through the blading. The $\hat{\varphi}_2(R_2)$ distribution can be corrected for endwall blockage consideration. An empirical method for predicting blockage in radially stacked rotor bladings of CVD is outlined in [**139**], see Chapter 2.

1f) The imaginary rotor is subdivided into Q2D elementary cascades along the span. Each elementary cascade under consideration has a mean radius R_{12}. For each elementary cascade, the following characteristics are calculated in steps ***1g)*** to ***1i)***, with consideration of $R_1 = R_2 = R_{12}$, and $\beta = 0$ (corresponding to the Q2D approach):

1g) $\hat{\varphi}_{12\,\mathrm{Q2D}}$, based on Eq. (4.7); and $C_{\mathrm{L\,opt\,Q2D}} \cdot (c/s_{\mathrm{b}\,12})_{\mathrm{opt\,Q2D}}$, based on Eq. (4.16b).

1h) $\alpha_{1\,\mathrm{Q2D}}$ and $\alpha_{2\,\mathrm{Q2D}}$ are calculated, on the basis of Eqs. (4.11a) and (4.11b). $C_{\mathrm{L\,opt\,Q2D}}$ is estimated using 2D cascade correlations, e.g. Howell's correlation represented by Eq. (4.4).

1i) Dividing $C_{\mathrm{L\,opt\,Q2D}} \cdot (c/s_{\mathrm{b}\,12})_{\mathrm{opt\,Q2D}}$, obtained in step *1g)*, by $C_{\mathrm{L\,opt\,Q2D}}$, obtained in step *1h)*, results in the optimum solidity $(c/s_{\mathrm{b}\,12})_{\mathrm{opt\,Q2D}}$ for the elementary cascade under consideration. The solidity can be expressed as $c/s_{\mathrm{b}12} = cN_{\mathrm{b}}/(2r_{12}\pi)$. Therefore, calculating the optimum solidity controls cN_{b}, related to the suction side flow path length summed for all of the blades of number N_{b}. By selecting an appropriate N_{b} value, and with knowledge of r_{12}, the blade spacing $s_{\mathrm{b}12}$ is calculated, and the optimum chord length assigned to the elementary cylindrical cascade, $c_{\mathrm{opt\,Q2D}}$, is obtained.

1j) The camber geometry as well as the stagger angle γ_{12} are designed in order to match the designed performance at moderate losses, taking 2D cascade correlations as starting point. Appropriate ways of cambering and staggering are beyond the scope of the thesis.

Design based on the Q3D approach. Besides the Q2D approach, the blade characteristics *of the same rotor* can be obtained via a Q3D-based process as well.

2a) The flow field in the rotor designed with the Q2D approach is to be tested using CFD. The distribution of mean yaw angle $\tilde{\varepsilon}_{\mathrm{L}}$ along the radius is estimated. See Eq. (4.5) for details.

2b) With knowledge of the designed Q2D geometry incorporating the stagger angle γ_{12}, the spanwise distribution of cone half-angle β for the Q3D approach is estimated along the span, using Eq. (4.6).

2c) The $\hat{\psi}_2(R_2)$ and $\hat{\varphi}_2(R_2)$ distributions established in Q2D design are used as basis also for the Q3D approach. For realisation of these distributions also in the Q3D approach, and for further improvement of efficiency, re-cambering and re-staggering [**4**] techniques may iteratively be used.

2d) Steps from *1g)* can be carried out in the Q3D approach, for the same elementary rotors of radii R_{12}: $\hat{\varphi}_{12\,\mathrm{Q3D}}$ [Eq. (4.7)], $C_{\mathrm{L\,opt\,Q3D}} \cdot (c/s_{\mathrm{b}\,12})_{\mathrm{opt\,Q3D}}$ [Eq. (4.16b)], $\alpha_{1\,\mathrm{Q3D}}$ [Eq. (4.11a)], $\alpha_{2\,\mathrm{Q3D}}$ [Eq. (4.11b)], $C_{\mathrm{L\,opt\,Q3D}}$ [Eq. (4.4)], $(c/s_{\mathrm{b}\,12})_{\mathrm{opt\,Q3D}}$, and $c_{\mathrm{opt\,Q3D}}$, are calculated.

4.4. Incorporation of FSW into preliminary CVD

In the calculations outlined in the previous section, and carried out using parameters valid in normal fan applications, it has been found that, for the same mean radius r_{12},

$$c_{\text{opt Q3D}} < c_{\text{opt Q2D}} \tag{4.17a}$$

The underlying physics of this tendency is as follows. Viewing the blade passage flow in the Q3D approach, the diffusion (deceleration) is usually moderate in comparison to that in the Q2D approach, i.e.

$$\left(\frac{\hat{w}_2}{\hat{w}_1}\right)_{\text{Q3D}} > \left(\frac{\hat{w}_2}{\hat{w}_1}\right)_{\text{Q2D}} \tag{4.17b}$$

The validity of this relationship is justified in **Appendix Q**. On the basis of Eqs. (4.11a) to (4.11b), it can be pointed out that $\cos\alpha$ is the ratio between the meridional velocity component and the relative velocity. By assuming approximately equal meridional velocities for the inlet and the outlet (see the aforementioned equations), relationship (4.17b) can be written as

$$\left(\frac{\cos\alpha_1}{\cos\alpha_2}\right)_{\text{Q3D}} > \left(\frac{\cos\alpha_1}{\cos\alpha_2}\right)_{\text{Q2D}} \tag{4.17c}$$

Taking Eq. (4.4) into account, the above relationship implies

$$C_{\text{L opt Q3D}} > C_{\text{L opt Q2D}} \tag{4.17d}$$

The fundamental cascade equations [conf. Eq. (4.16a)] developed for the Q3D and Q2D approaches have been compared. For Q2D, see the comments at the end of Section 4.3.1. The inequality expressed in relationship (4.17d) has been found to be dominant in the difference between the Q3D and Q2D fundamental cascade equations. This implies that the optimum solidity for the Q3D approach tends to be less than that for the Q2D approach, leading to relationship (4.17a).

FSW offers a unique means for *simultaneous* realization of the different $c_{\text{opt Q2D}}$ and $c_{\text{opt Q3D}} < c_{\text{opt Q2D}}$ values for the same mean radius r_{12}, *in one blade geometry*. **Figure 4.2** gives an aid to the explanation. In Fig. 4.2a), the blade is viewed from the direction normal to the FSW blade, being approximately normal to $\underline{u}_r$. The optimum FSW angle is approximated as follows, using Fig. 4.2b):

$$|\lambda_{\text{opt}}| = \frac{\tilde{\varepsilon}_{\text{L}}}{2} + \lambda^* \tag{4.18}$$

The absolute value is taken in Eq. (4.18) for λ_{opt}, because, according to the sign convention in [**2**], the sweep angle is negative for FSW. The auxiliary angle λ^* is obtained in the following way. Applying the *law of sines* to the triangle next to the grey one in Fig. 4.2b) reads

$$\frac{1}{2}\frac{\sqrt{\left(c_{\text{opt Q3D}}\sin\tilde{\varepsilon}_{\text{L}}\right)^2+\left(c_{\text{opt Q2D}}-c_{\text{opt Q3D}}\cos\tilde{\varepsilon}_{\text{L}}\right)^2}}{\sin\left(90°-\tilde{\varepsilon}_{\text{L}}/2\right)}=\frac{1}{2}\frac{c_{\text{opt Q2D}}-c_{\text{opt Q3D}}}{\sin\lambda^*} \tag{4.19}$$

The expression under the square root multiplied by ½ is the length of the shortest side of the grey triangle. Rearrangement of Eq. (4.19) reads

$$\lambda^*=\sin^{-1}\frac{(1-CR)\cos\left(\tilde{\varepsilon}_{\text{L}}/2\right)}{\sqrt{(1-CR)^2+2CR\left(1-\cos\tilde{\varepsilon}_{\text{L}}\right)}} \tag{4.20}$$

Where $CR=c_{\text{opt Q3D}}/c_{\text{opt Q2D}}$ is the Q3D-to-Q2D chord ratio.

It is conceivable using Fig. 4.2b) that $\tilde{\varepsilon}_{\text{L}}\to 0$ (no radial flow) implies $CR\to 1$, $\lambda^*\to 0$, and $|\lambda_{\text{opt}}|\to 0$. Therefore, away from the endwalls, radial blade stacking is proposed by the presented design method for truly 2D rotor flows, approximated by the free vortex design style.

On the basis of an appropriate CFD tool, an iterative design procedure can be elaborated. In the first step, an USW rotor is designed using the Q2D approach (steps *1a)* to *1j)* in Section 4.3.2). The USW rotor is simulated, according to step *2a)* in Section 4.3.2. The first approximation of $\tilde{\varepsilon}_{\text{L}}$ along the radius is made on this basis. Then, a first version of the FSW rotor is designed, on the basis of steps *2b)* to *2d)* in Section 4.3.2., and Eqs. (4.18) and (4.20). This first version of the FSW rotor, labelled as FSW_1, is surveyed by CFD. Given that FSW in itself moderates the radially outward flow on the suction side in the case of rotors of CVD, as reported e.g. in [**19, 26, 139, 160**], a reduction is foreseen in $\tilde{\varepsilon}_{\text{L}}$ for the FSW_1 rotor, compared to the USW one. Using the reduced $\tilde{\varepsilon}_{\text{L}}$ data, a next, FSW_2 rotor version can be designed, for which Eq. (4.18) tailors a moderated $|\lambda_{\text{opt}}|$ value. The CFD and redesign procedures can be repeated upon demand, for monitoring $\tilde{\varepsilon}_{\text{i}}$ in the consecutive rotor versions FSW_{i}. Fast convergence in $|\lambda_{\text{opt}}|$ is foreseen via some iterative steps.

When applying dihedral of local angle κ, e.g. in circumferential forward skew [**4**], the blade surface in Fig. 4.2a) can be viewed as making an angle κ with the $\underline{u}_r$ direction, as illustrated in Fig. 4.2c). Consequently, only the $c_{\text{opt Q3D}}\cos\kappa$ component of the Q3D optimum chord will play a role in determining λ_{opt}. Therefore, $CR\cdot\cos\kappa$ is to be substituted into Eq. (4.20), instead of CR. In circumferential forward skew, the sweep and dihedral angles are in relationship. Therefore, besides optimum FSW, Eq. (4.18) implies the existence of an optimum forward-skewed geometry as well. The $\tilde{\varepsilon}_{\text{L}}$ distribution affected by both sweep and dihedral is to be monitored via the iterative CFD campaign.

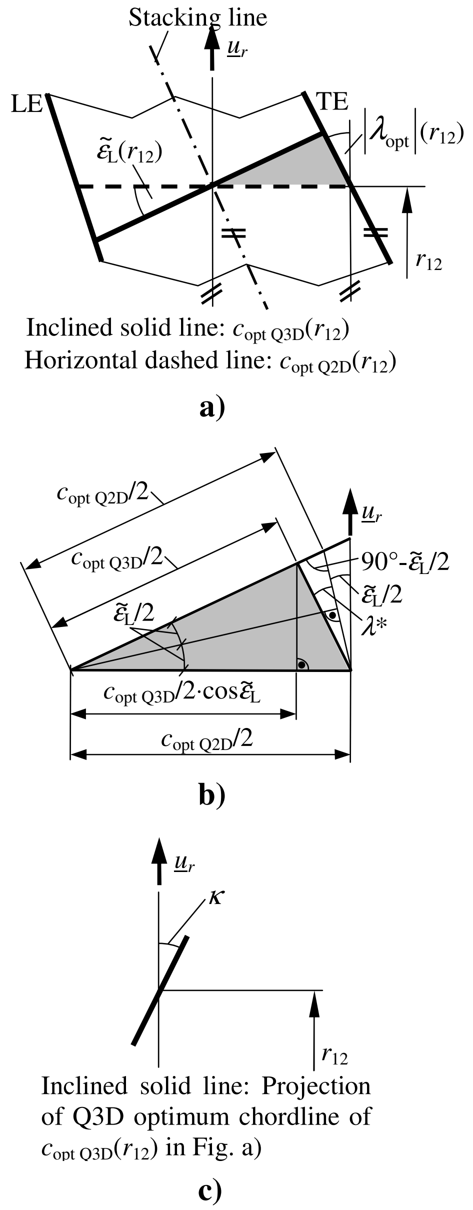

Figure 4.2. *Sketch for obtaining optimum forward sweep angle.* ***a)*** *The blade is viewed from the direction normal to the blade surface, in absence of dihedral.* ***b)*** *Enlarged view of the grey triangle and its surroundings from Fig. a).* ***c)*** *The blade is viewed from the direction parallel to the Q2D chordline at* r_{12}*, at presence of dihedral. LE: leading edge. TE: trailing edge.*

4.5. Design case study

The comparative USW and FSW rotors reported in [**26**] serve herein as design examples. The original, USW version was designed using a Q2D approach by Bencze and his co-authors, and was investigated by experimental [**86, 91, 144**] and CFD [**93, 145-146**] means. It was redesigned by the author using the preliminary design method presented herein, resulting in a FSW, sweep-only (no dihedral) rotor. The isentropic total pressure rise was prescribed along the span by using the power function in Eq. (4.10), with $m = 1.4$. A uniform axial inlet condition was assumed in design. The endwall blockage was approximately considered by correcting the design outlet axial velocity profile, using the empirical correlation in [**139**] (Chapter 2). Howell's correlation [Eq. (4.4)] was used in determining the optimum chord lengths in the Q2D and Q3D approaches. The solidity and the camber geometry were eventually corrected for manufacturing reasons.

Representative operational and geometrical data for the rotors are summarized in **Table 3.1** of the previous chapter. Possible discrepancies between the USW and FSW data are indicated as uncertainty ranges in the last column of the table. Further details on the blade geometry are available in [**25-26, 95, 170, 175**].

When designing FSW, the β distribution along the span, representing the Q3D approach, has iteratively been modelled on the basis of CFD. The spanwise distributions of $\hat{\psi}_2$ and $\hat{\varphi}_2$ data are presented in **Figure 4.3**. The uncertainty of the LDA data, valid at 95 % level of confidence, is reported in **Table 4.1**, and is indicated by error bars in the diagrams. The fair agreement among the CFD [**26, 95**], experimental [**91, 144**], and preliminary design data away from the endwalls supports the validity of the applied CFD technique as well as the reasonability of the swirl and axial velocity distributions applied in the design. Only limited efforts were made in the presented case study to correct the blade geometries to better match the designed $\hat{\psi}_2$ and $\hat{\varphi}_2$ distributions.

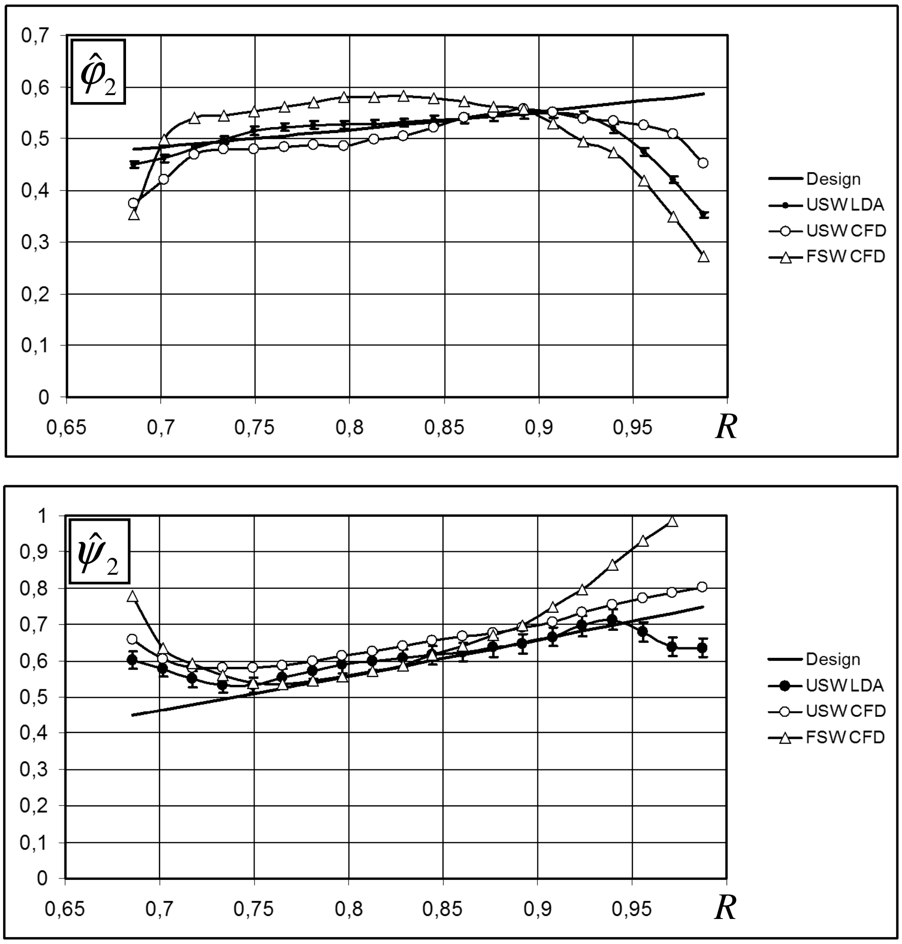

Figure 4.3. *Spanwise distributions of* $\hat{\varphi}_2$ *and* $\hat{\psi}_2$

Table 4.1. *Experimental uncertainty*

Quantity	Φ	Ψ	$\hat{\psi}_2$	$\hat{\varphi}_2$
Uncertainty	± 1.5 %	± 0.5 %	± 4 %	± 1.5 %

Figure 4.4 presents the spanwise distributions of $|\lambda_{opt}|$ and β obtained in design of FSW. A comparative analysis on the limiting streamlines on the suction side of USW and FSW was reported in Chapter 3 [**160**]. In addition, the conical blade sections considered in the Q3D approach, corresponding to the β distribution in Fig. 4.4, are compared to the meridional projection of suction side limiting streamlines of FSW in **Figure 4.5**, reproduced from [**26**]. The fair agreement between the modelled conical sections and the limiting streamlines on the suction side, especially away from the endwalls, supports the self-consistency of the Q3D design approach.

When manufacturing FSW, the 35° optimum sweep angle obtained near the hub (referring to Fig. 4.4) was applied along the entire span, as a reasonable approximation, for moderating the axial extension of the rotor.

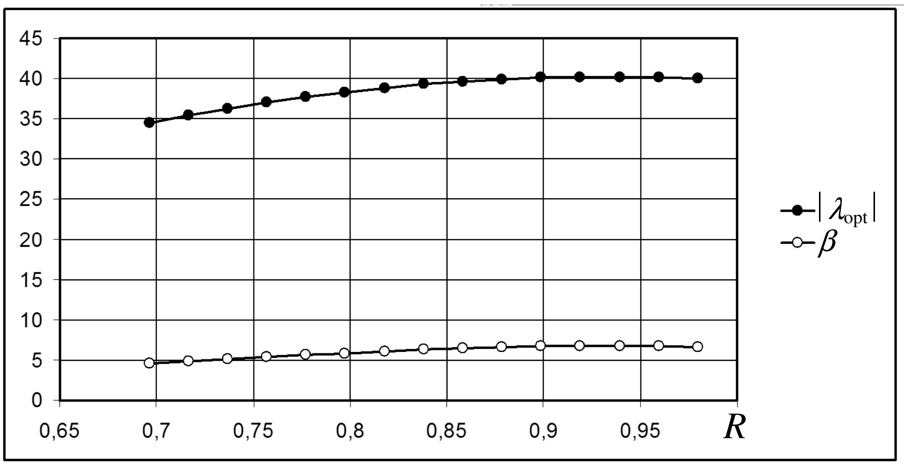

Figure 4.4. *Spanwise distributions of* $|\lambda_{opt}|$ and β

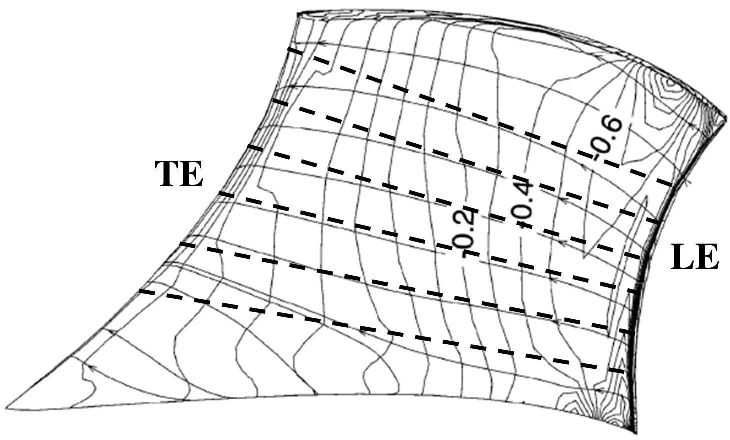

Figure 4.5. *Comparison between simulated suction side limiting streamlines [solid lines extending from leading edge (LE) to trailing edge (TE)] and conical sections modelled in the Q3D approach (dashed lines) for FSW. Contour lines: static pressure coefficient* [**26**].

The FSW rotor presented herein is not meant to be the best solution available from this particular design assignment, in lack of an extensive, fully 3D CFD-based iterative refinement of rotor geometry, also incorporating the spanwise distribution of sweep. Still, as already demonstrated in Fig. 3.8 (reproduced from [**26**]), FSW exhibits considerably lower total pressure loss along the dominant portion of span, especially on the suction side and away from the endwalls. Considering the studies in [**160**], this is attributed to the design method presented herein. Paper [**25**] reports on the difference between averaged total pressure loss coefficients related to FSW and USW. The data indicate that applying FSW resulted in total pressure loss reduction along the dominant part of span. The spanwise mean value of loss reduction is approximately 10 per cent of dynamic pressure calculated with inlet relative velocity at midspan [**25**].

The FSW rotor was manufactured with larger tip clearance, for mechanical reasons (τ/S_{FSW} = 0.04, τ/S_{USW} = 0.029). The characteristic and efficiency curves were measured at the Department for both USW and FSW [**175**], and were published later also in references [**25-26**]. The experimental uncertainties are reported in Table 4.1. Measured at the design flow rate, FSW generated a slightly higher total pressure rise: $\Psi_{\mathrm{FSW}} = 0.52$, $\Psi_{\mathrm{USW}} = 0.49$ [**26**]. The global total efficiency measured for FSW has been corrected for the clearance size valid for the USW rotor, on the basis of the semi-empirical expression in [**184**], with substitution of near-tip data approximated using Fig. 4.3 ($\hat{\psi}_2$ = 0.65, $\hat{\varphi}_{12} = 0.5$, $\alpha_\infty = 50°$) and AR = 0.597 from Table 3.1.

Due to the incorporation of FSW in the CVD method, the CFD-based and experiment-based data showed 2 percent [**26**] and 3 percent gain in $\overline{\eta}_{\mathrm{t}}$, respectively, at the design flow rate. As the literature overview in [**4**] suggests, efficiency gain in the percent order of magnitude is considered as success in turbomachinery R&D. In this view, the design method proposed herein offers potential for efficiency gain that is worth mentioning.

The success of the design method incorporating FSW in CVD supports the latent tendency appearing in the literature [**18-19, 37-38, 50, 158**], and pointed out by the author [**4**], that FSW is especially beneficial for efficiency gain in the case of CVD rotors, at the design point. In these cases, efficiency gain up to the percent order of magnitude has been reported.

4.6. NEW SCIENTIFIC RESULTS [4, 95, 170, 173-176, 190]

Thesis point 7 The author has elaborated a new preliminary blade design method – termed herein the new method –, incorporating FSW in CVD. Supplementing the traditional Q2D CVD technique, the new method enables a more accurate consideration and control of blade aerodynamics along the 3D suction side flow paths, where the majority of loss is generated away from the endwalls. For this purpose, the new method combines the Q2D and Q3D blade design approaches for CVD rotors. A key issue of the new method is determining the optimum blade solidities separately in the Q2D and Q3D approaches, and realizing these different solidities simultaneously in one single forward-swept blade geometry. The view dominates in the literature that sweep is a *design input*, i.e. it is *prescribed* in preliminary design. In contrast, the new method serves with the sweep angle distribution as *design output*, i.e. the blade stacking geometry, found beneficial from aerodynamic point of view, is a *result* of the preliminary design process. A design case study revealed that the new method offers the potential for efficiency gain in the percent order of magnitude at the design flow rate.

5. UTILISATION OF THE RESULTS; OUTLOOK

The results presented herein have been obtained within the framework of basic departmental research as well as applied R&D projects. The background knowledge in design, CFD, experimentation, and fan operation, related to the guidelines and methods summarized in the thesis points, has been utilised by the Department in R&D and consultancy for the ventilation industry and end-users. Some examples, selected from the areas of such activity, are as follows: industrial ventilating fans of high specific performance and high efficiency; fans applied in heat exchangers; destratification jet fans; electric motor cooling fans with low noise and moderate absorbed shaft power; fans of long throw and high specific performance; flue gas extractor fans; a wind tunnel fan of broad operational range.

Beyond the above applications, the future objective is the elaboration of a CFD-aided, algorithmised blade design and optimisation method of wide-ranging applicability, incorporating the features of controlled vortex design and non-radial stacking, corresponding to the current trend of turbomachinery R&D. As a preparatory step in design and optimisation, initial versions of blading geometry are to be elaborated, utilising the guidelines and the preliminary design method discussed in the thesis points. Taking these initial blading versions as a basis, the systematic harmonisation of spanwise distribution of blade circulation, blade stacking, and the geometry of the elementary blade sections is to be carried out in an algorithmised manner, incorporating advanced CFD methods.

A parallel future goal is the concerted investigation of aerodynamic and noise generation mechanisms in highly-loaded axial flow rotor blade rows. Special attention is to be paid to the flow phenomena related to controlled vortex design, appearing as noise sources, and influenced by non-radial blade stacking. Among others, such phenomena are: vortices shed from the blade trailing edge; stagnation of high-loss fluid near the tip, influencing the tip leakage flow; and thickened boundary layer on the blade suction side. The guidelines for moderation of noise, obtained in such investigation, are to be eventually considered in the aforementioned algorithmised design and optimisation procedure.

The project results have been published to the turbomachinery community, at technical events and in journals, including archival journals considered by the Science Citation Index. These publications have received a number of independent citations by colleagues working for foreign research institutions and industrial firms. The results of R&D and related industrial activity have been incorporated in university courses taught by the author in the fields of fluid machinery, industrial air technology, and flow measurements. Under supervision of the author, numerous undergraduate, graduating, and PhD students have contributed and continue to contribute to the research activity.

6. REFERENCES

Some industrial companies are included in the Reference List. This is not to be considered as a commercial endorsement. Furthermore, their inclusion in the dissertation is not to be considered as a judgment, either positive or negative, of their products. The independent references as well as the publications elaborated by the author and cited herein are included in a single list.

[1] Lakshminarayana, B. *Fluid Dynamics and Heat Transfer of Turbomachinery*. John Wiley & Sons, Inc., New York, 1996.

[2] Smith, L. M., Yeh, H. Sweep and dihedral effects in axial-flow turbomachinery. *ASME J. Basic Engineering*, 1963, **85**, pp. 401-416.

[3] Daly, B. B. *Woods practical guide to fan engineering*. Woods of Colchester Ltd., 1992. (Sixth impression)

[4] Vad, J. Aerodynamic effects of blade sweep and skew in low-speed axial flow rotors near the design flow rate: an overview. *Proc. Instn Mech. Engrs, Part A, J. Power and Energy*, 2008, **222**, pp. 69-85.

[5] Küchemann, D. The distribution of lift over the surface of swept wings. *The Aeronautical Quarterly*, 1952, **4**, pp. 261-278.

[6] Estevadeordal, J., Gogineni, S., Copenhaver, W., Bloch, G., Brendel, M. Flow field in a low-speed axial fan: a DPIV investigation. *Experimental Thermal and Fluid Science*, 2000, **23**, pp. 11-21.

[7] *United States Patent.* High efficiency and low weight axial flow fan. Patent No. US 6,368,061 B1., 2002.

[8] Gallimore, S. J., Bolger, J. J., Cumpsty, N. A., Taylor, M. J., Wright, P. I., Place, J. M. M. The use of sweep and dihedral in multistage axial flow compressor blading – Parts I and II. *ASME J. Turbomachinery*, 2002, **124**, pp. 521-541.

[9] Ebm-papst Mulfingen GmbH & Co. KG. Automotive-brushless DC fans & blowers. Air-conditioning of commercial vehicles. 2005, *Product catalogue*, Version 05/2005.

[10] Moreau, S., Henner, M., Neal, D. 3D rotor-stator interaction in automotive engine cooling fan systems. *6th European Conference on Turbomachinery Fluid Dynamics and Thermodynamics*, Lille, 2005, Proceedings pp. 145-157.

[11] Gifford, N. L., Hunt, A. G., Savory, E., Martinuzzi, R. J. Experimental study of low-pressure automotive cooling fan aerodynamics under blocked conditions. *CSME 2006 Forum*, Kananaskis, Calgary, Canada, 2006.

[12] Moreau, S., Henner, M., Brouckaert, J. F., Neal, D. Numerical and experimental investigation of rotor-stator interaction in automotive engine cooling fan systems. *7th European Conference on Turbomachinery Fluid Dynamics and Thermodynamics*, Athens, 2007, Proceedings pp. 215-228.

[13] Clemen, C. Inverse 3D camber-line calculation tool INCA-3D. *ASME TURBO EXPO*, Berlin, 2008, *ASME Paper* GT2008-50253, CD-ROM Proceedings (ISBN 0-7918-3824-2)

[14] Clemen, C., Schrapp, H., Gümmer, V., Müller, R., Künzelmann, M., Vogeler, K. Design of a highly-loaded four-stage low-speed research compressor. *ASME TURBO EXPO*, Berlin, 2008, *ASME Paper* GT2008-50254, CD-ROM Proceedings (ISBN 0-7918-3824-2)

[15] Henner, M., Moreau, S., Brouckaert, J. F. Comparison of experimental and numerical flow field in an automotive engine cooling module. *8th European Conference on Turbomachinery Fluid Dynamics and Thermodynamics (ETC'08)*, Graz, 2009, Proceedings pp. 387-399.

[16] Jin, G., Ouyang, H., Wu, Y., Du, Z. Experimental and numerical investigations on the tip leakage flow of axial fans with circumferential skewed blades under off-design conditions. *Proc. Institution of Mechanical Engineers – Part C: Journal of Mechanical Engineering Science*, 2010, **224**, pp. 1203-1216.

[17] Clemen, C., Stark, U. Compressor blades with sweep and dihedral: a parameter study. *5th European Conference on Turbomachinery Fluid Dynamics and Thermodynamics*, Prague, 2003, Proceedings pp. 151-161.

[18] Mohammed, K. P., Prithvi Raj, D. Investigation on axial flow fan impellers with forward swept blades. *ASME J. Fluids Engineering,* September 1977, pp. 543-547.

[19] Yamaguchi, N., Tominaga, T., Hattori, S., Mitsuhashi, T. Secondary-loss reduction by forward-skewing of axial compressor rotor blading. *Yokohama International Gas Turbine Congress*, Yokohama, 1991, Proceedings pp. II.61-II.68.

[20] Breugelmans, F. A. E. Energy efficient design through fluid dynamics improvements in turbocomponents. *International Seminar on Thermal and Fluid Engineering for Advanced Energy Systems.* Institute of Advanced Material Study, Kyushu University, Kasuga, Japan, 1997. Lecture note, Von Karman Institute for Fluid Dynamics.

[21] Beiler, M.G., Carolus T.H. Computation and measurement of the flow in axial flow fans with skewed blades. *ASME J. Turbomachinery*, 1999, **121**, pp. 59-66.

[22] Gümmer, V., Swoboda, M., Goller, M., Dobat, A. The impact of rotor tip sweep on the three-dimensional flow in a highly-loaded single-stage low-speed axial compressor: Part I – Design and numerical analysis. *5th European Conference on Turbomachinery Fluid Dynamics and Thermodynamics*, Prague, 2003, Proceedings pp. 163-174.

[23] Rohkamm, H., Wulff, D., Kosyna, G., Saathoff, H., Stark, U., Gümmer, V., Swoboda, M., Goller, M. The impact of rotor tip sweep on the three-dimensional flow in a highly-loaded single-stage low-speed axial compressor: Part II – Test facility and experimental results. *5th European Conference on Turbomachinery Fluid Dynamics and Thermodynamics*, Prague, 2003, Proceedings pp. 175-185.

[24] McNulty, G. S., Decker, J. J., Beacher, B. F., Khalid, S. A. The impact of forward swept rotors on tip-limited low-speed axial compressors. 2003, *ASME Paper* No. GT2003-38837.

[25] Corsini, A., Rispoli, F. The role of forward sweep in subsonic axial fan rotor aerodynamics at design and off-design operating conditions. 2003, *ASME Paper* No. GT2003-38671.

[26] Corsini, A., Rispoli, F. Using sweep to extend the stall-free operational range in axial fan rotors. *Proc. Instn Mech. Engrs, Part A, J. Power and Energy*, 2004, **218**, pp. 129-139.

[27] Clemen, C., Gümmer, V., Goller, M., Rohkamm, H., Stark, U., Saathoff, H. Tip-aerodynamics of forward-swept rotor blades in a highly-loaded single-stage axial-flow low-speed compressor. 10th International Symposium on *Transport Phenomena and Dynamics of Rotating Machinery (ISROMAC10)*, Honolulu, 2004, Proceedings CD-ROM, Paper No. 027.

[28] Goller, M., Gümmer, V., Clemen, C., Swoboda, M. Enhancement of highly-loaded axial compressor stage performance using rotor blade tip tailoring, Part I – Numerical design studies. *6th European Conference on Turbomachinery Fluid Dynamics and Thermodynamics*, Lille, 2005, Proceedings pp. 88-99.

[29] Rohkamm, H., Kosyna, G., Saathoff, H., Stark, U. Enhancement of highly-loaded axial compressor stage performance using rotor blade tip tailoring, Part II – Experimental results. *6th European Conference on Turbomachinery Fluid Dynamics and Thermodynamics*, Lille, 2005, Proceedings pp. 100-110.

[30] Brown, N. A. The use of skewed blades for ship propellers and truck fans. *Noise and Fluids Engineering. Winter Annual Meeting of ASME*, Atlanta, 1977. Proceedings pp. 201-207.

[31] Wright, T., Simmons, W. E. Blade sweep for low-speed axial fans. *ASME J. Turbomachinery*, 1990, **112**, pp. 151-158.

[32] Ohtsuta, K., Akishita, S. Noise reduction of short ducted fan by using forward swept and inclined blade. 1990, *AIAA paper* No. 90-3986-CP.

[33] Kodama, H., Namba, M. Lifting surface theory for steady aerodynamic analysis of ducted counter rotation propfan. 1992, *ASME Paper* No. 92-GT-14.

[34] Stütz, W. Einfluß der Sichelung auf das aerodynamische und akustische Verhalten von Axialventilatoren. *Strömungsmechanik und Strömungsmaschinen* (Mitteilungen des Instituts für Strömungslehre und Strömungsmaschinen der Universität Karlsruhe), 1992, **44**, pp. 1-58.

[35] Srivastava, R., Mehmed, O. On the static stability of forward swept propfans. 1993, *AIAA paper* No. 93-1634-CP.

[36] Meixner, H.-U., Caglar, S., Felsch, K.-O. Geräuschreduktion durch Sichelung der Schaufeln bei Axialventilatoren. *Strömungsmechanik und Strömungsmaschinen* (Mitteilungen des Instituts für Strömungslehre und Strömungsmaschinen der Universität Karlsruhe), 1994, 47/94, pp. 43-58.

[37] Meixner, H. U. Vergleichende LDA-Messungen an ungesichelten und gesichelten Axialventilatoren. *Doctoral Dissertation, Universität Karlsruhe*, VDI-Verlag, Reihe 7: Strömungstechnik, No. 266, Düsseldorf, 1995.

[38] Beiler, M. G. Untersuchung der dreidimensionalen Strömung durch Axialventilatoren mit gekrümmten Schaufeln. *Doctoral Dissertation, Universität-GH-Siegen*, VDI Verlag, Reihe 7: Strömungstechnik, No. 298, Düsseldorf, 1996.

[39] Carolus, T., Stremel, M. Sichelschaufeln bei Axialventilatoren. *Heizung Lüftung /Klima Haustechnik*, 2000, **51**, pp. 33-39.

[40] Thomson, D., Watson, K., Norden, C., Gorrell, S., Braisted, W., Brockman, R. Assessment of organic matrix components for a forward swept fan stage. 1994, *AIAA Paper* No. 94-1353-CP.

[41] Lee, G. H., Baek, J. H. A numerical study on the structure of tip clearance flow in a highly forward-swept axial-flow fan. 2002, *ASME Paper* No. FEDSM2002-31186.

[42] Lee, G. H., Baek, J. H., Myung, H. J. Structure of tip leakage flow in a forward-swept axial-flow fan. *Flow, Turbulence and Combustion*, 2003, **70**, pp. 241-265.

[43] Govardhan, M., Krishna Kumar, O. G., Sitaram, N. Computational study of the effect of sweep on the performance and flow field in an axial flow compressor rotor. *Proc. Instn Mech. Engrs, Part A, J. Power and Energy*, 2007, **221**, pp. 315-329.

[44] Wadia, A. R., Szucs, P. N., Crall, D. W. Inner workings of aerodynamic sweep. *ASME J. Turbomachinery*, 1998, **120**, pp. 671-682.

[45] Kuhn, K. Experimentelle Untersuchung einer Axialpumpe und Rohrturbine mit gepfeilten Schaufeln. *Doctoral Dissertation, Technische Universität Graz*, Institut for Hydraulische Strömungsmaschinen, 2000.

[46] Forstner, M. Experimentelle Untersuchungen an vorwärts und rückwärts gepfeilten Axialpumpenschaufeln. *Doctoral Dissertation, Technische Universität Graz*, Institut for Hydraulische Strömungsmaschinen, 2002.

[47] Lucheng Ji, Jiang Chen, Feng Lin. Review and understanding on sweep in axial compressor design. 2005, *ASME Paper* No. GT2005-68473.

[48] Helming, K. Numerical analysis of sweep effects in shrouded propfan rotors. *J. Propulsion and Power*, 1996, **12**, pp. 139-145.

[49] Deich, M. E., Troyanovskii, B. M., Filippov, G. A. An effective way of improving the efficiency of turbine stages. *Thermal Engineering*, 1990, **37**, pp. 520-523.

[50] Li, Y., Quang, H., Du, Z.-H. Optimization design and experimental study of low-pressure axial fan with forward-skewed blades. *Int. J. Rotating Machinery*, **2007**, Article ID 85275, 10 pages, doi: 10.1155/2007/85275.

[51] Forstner, M., Kuhn, K., Glas, W., Jaberg, H. The flow field of pump impellers with forward and backward sweep. *4th European Conference on Turbomachinery Fluid Dynamics and Thermodynamics*, Florence, 2001, Proceedings pp. 577-587.

[52] Jang,C.-M., Li, P., Kim, K.-Y. Optimization of blade sweep in a transonic axial compressor rotor. *JSME Int. J., Series B – Fluids and Thermal Egineering*, 2005, **48**, pp. 793-801.

[53] Jang, C.-M., Samad, A., Kim, K-Y. Optimal design of swept, leaned and skewed blades in a transonic axial compressor. 2006, *ASME Paper* No. GT2006-90384.

[54] Shang, E., Wang, Z. Q., Su, J. X. The experimental investigations on the compressor cascades with leaned and curved blade. 1993, *ASME paper* No. 93-GT-50

[55] Sasaki, T., Breugelmans, F. Comparison of sweep and dihedral effects on compressor cascade performance. *ASME J. Turbomachinery*, 1998, **120**, pp. 454-464.

[56] Song, Y., Zhao, G., Chen, F., Wang, Z. Experimental study of sweep and dihedral effects on compressor cascade performance. *6th European Conference on Turbomachinery Fluid Dynamics and Thermodynamics*, Lille, 2005, Proceedings pp. 1-9.

[57] Horlock, J. H. *Axial Flow Compressors*. Kreiger Publishing Co., Melbourne, FL., 1973.

[58] HELIOS *Hauptkatalog* 2001/2002. Druckschrift-Nr. 95 178.005 / 03.01

[59] Somlyódy, L. Axiálventilátorok tervezése és jelleggörbeszámítása. (Design and characteristic curve calculation of axial flow fans) *Doctoral Dissertation, Technical University of Budapest*, 1971. (in Hungarian)

[60] Wolter GmbH. Axial fans AXV, BXV. 2007, *Product catalogue*, Version WX1 V.2007/2.

[61] Jiang, Cai-ling, Chen Jiang-ping, Chen Zhi-jiu, Tian Jie, Ou Yang Hua, Du Zhao-hui. Experimental and numerical study on aeroacoustic sound of axial flow fan in room air conditioner. *Applied Acoustics*, 2007, **68**, pp. 458-472.

[62] Laraqi, N., García de María, J. M., Baïri, A. Thermal evolution of a fan submitted to high temperature in a confined environment. *High Temperature*, 2007, **45**, pp. 717-724.

[63] Bianchi, S., Corsini, A., Rispoli, F., Sheard, A. G. Experimental aeroacoustic studies on improved tip geometries for passive noise signature control in low-speed axial fans. *ASME TURBO EXPO*, Berlin, 2008, *ASME Paper* GT2008-51057, CD-ROM Proceedings (ISBN 0-7918-3824-2)

[64] Szlivka, F., Molnár, I. Measured and non-free vortex design results of axial flow fans. *Journal of Mechanical Science and Technology*, 2008, **22**, pp. 1902-1907.

[65] Keszthelyi, I. Axiális ventilátorok tervezése a radiális sebesség-összetevő figyelembevételével. Mezőgazdasági axiális ventilátorok. (Design of axial fans with consideration of radial velocity component. Agricultural axial fans.) (in Hungarian) *Magyar Épületgépészet*, 2000, **49** (11), pp. 27-28.

[66] Fog Cannon. Function. *www.fogcannon.com*

[67] Bruschi, P. Percorso virtuoso. *Costruzioni*, 2009, October, pp. 22-26.

[68] Vad, J. Application of controlled vortex design concept to axial flow industrial fans. *Proc. GÉPÉSZET'2010 Konferencia (Conference on Mechanical Engineering)*, Budapest, 2010 (CD-ROM) (ISBN 978-963-313-007-0), pp. 875-881.

[69] Vad, J., Horváth, Cs., Lohász, M. M., Jesch, D., Molnár, L., Koscsó, G., Nagy, L., Dániel, I., Gulyás, A. Redesign of an electric motor cooling fan for reduction of fan noise and absorbed power. *Proc. 11th European Conference on Turbomachinery Fluid Dynamics and Thermodynamics (ETC'11)*, Istanbul, 2011, Paper No. 055, pp. 69-79.

[70] Dring, R. P., Joslyn, H. D., Hardin, L. W. An investigation of axial compressor rotor aerodynamics. *ASME J. Engineering Power*, 1982, **104**, pp. 84-96.

[71] Sieverding, C. H. Secondary flows in axial turbines. 1986, Von Karman Institute for Fluid Dynamics, Belgium, *Lecture note* No. 9.

[72] Wallis, R. A. *Axial Flow Fans*. George Newnes Limited, London, 1961.

[73] Sørensen, D. N., Sørensen, J. N. Toward improved rotor-only axial fans – Part I: A numerically efficient aerodynamic model for arbitrary vortex flow. *ASME J. Fluids Engineering*, 2000, **122**, pp. 318-323.

[74] Carolus, T. *Ventilatoren.* B. G. Teubner Verlag, Wiesbaden, 2003.

[75] Gruber, J. A szárnylapátos szellőző méretezése és üzeme. (Design and operation of airfoil ventilating fan) *Doctoral Dissertation, Technical University of Budapest*, 1943. (in Hungarian)

[76] Stepanoff, A. J. *Turboblowers*. John Wiley & Sons, New York, 1955.

[77] Shepherd, D. G. *Principles of Turbomachinery*. The Macmillan Company, New York, 1956.

[78] Vavra, M. H. *Aero-thermodynamics and flow in turbomachines*. John Wiley & Sons, New York, London, 1960.

[79] Somlyódy, L. Wirkung der Drallverteilung auf die Kenngrössen von Axialventilatoren. *Periodica Polytechnica*, 1971, **15** (3), pp. 293-305.

[80] Somlyódy, L. Berechnung der Beschaufelung und der Strömung axial durchströmter Wirbelmaschinen mit Anwendung von Gittermessung. *Periodica Polytechnica*, 1971, **15,** No. 3.

[81] Somlyódy, L. Improvement of the efficiency of free blow-out axial fans using variable circulation. *Acta Technica Academiae Scientiarum Hungaricae*, 1974, **79**, pp. 115-132.

[82] Nath, G. Investigation of three-dimensional flow through the rotor of an axial fan. *J. Aeronautical Society India*, 1970, **22**, pp. 45-52.

[83] Geshpande, A. G., Nath, G. Three-dimensional non-free vortex flow in axial fans. *Acta Technica Academiae Scientiarum Hungaricae*, 1971, **72**, pp. 215-239.

[84] Bencze, F., Szlivka, F. A new method for the design of axial flow fans of changing circulation. *8th Conference on Fluid Machinery*, Budapest, 1987, Proceedings pp. 94-102.

[85] Bencze, F., Füredi, G., Keszthelyi, I., Szlivka, F. Design and measurement experiences of axial flow fans. *9th Conference on Fluid Machinery*, Budapest, 1991, Proceedings pp. 35-43.

[86] Bencze,F., Keszthelyi, I., Szlivka, F., Pekáry, G. Der Einfluss der Schaufelzahl auf die Kennzahlen von Axialventilatoren. *Heizung Lüftung /Klima Haustechnik*, 8 / 1990, pp. 700-706.

[87] Gruber, J. (editor and author), Blahó, M., Herzog, P., Kurutz, I., Preszler, L., Szentmártony, T., Vajna, Z. *Ventilátorok* (*Ventilating fans*), Műszaki Könyvkiadó, Budapest, 4th edition, 1978 (in Hungarian)

[88] Vajna, Z. Kvázi-háromdimenziós módszer félaxiális átömlésű áramlástechnikai gépek méretezésére. (Quasi-three-dimensional method for design of mixed flow turbomachinery) *Academic doctoral dissertation, Technical University of Budapest*, 1987. (in Hungarian)

[89] Vad, J., Bencze, F., Füredi, G., Szombati, R. Fluid mechanical investigation on axial flow fans. *10th Conference on Fluid Machinery*, Budapest, 1995, Proceedings pp. 500-509.

[90] Vad, J., Bencze, F. Secondary flow in axial flow fans of non-free vortex operation. *8th International Symposium on Application of Laser Techniques to Fluid Mechanics*, Lisbon, 1996, Proceedings pp. 14.6.1.-14.6.8.

[91] Vad, J. Axiális átömlésű ventilátorok mögötti sebességtér vizsgálata lézer Doppler anemométerrel. (Laser Doppler anemometer investigation on the velocity field downstream of axial flow fans) *Ph.D. Dissertation, Technical University of Budapest, Department of Fluid Mechanics*, 1997. (in Hungarian)

[92] Szlivka, F., Molnár, I. Analysis of design method of axial flow fans in the view of the measurement results. *International Conference on Fluid and Thermal Energy Conversion*, 2006 (FTEC 2006), Jakarta, 2006, Proceedings pp. 107-1-107-13.

[93] Corsini, A., Rispoli, F., Vad, J., Bencze, F. Concerted experimental and numerical studies on axial flow fan rotor aerodynamics. *3rd European Conference on Turbomachinery Fluid Dynamics and Thermodynamics*, London, 1999, Proceedings pp. 519-531.

[94] Vad, J., Bencze, F. Improvement in design method of high performance axial flow turbomachines. *GÉPÉSZET'2000 Konferencia (Conference on Mechanical Engineering)*, Budapest, 2000, Proceedings pp. 462-466.

[95] Corsini, A., Rispoli, F., Vad, J., Bencze, F. Effects of blade sweep in a high performance axial flow rotor. *4th European Conference on Turbomachinery Fluid Dynamics and Thermodynamics*, Florence, 2001, Proceedings pp. 63-76.

[96] Molnár, L., Vad J. Design of a small-scale axial flow fan rotor of high specific performance. *Proc. MICROCAD'2009 Konferencia (International Computer Science Conference)*, Miskolc, 2009, Section E: Fluid and Heat Engineering, Proceedings pp. 71-76.

[97] Ziehl-Abegg AG. *Axial fans.* www.ziehl-abegg.com

[98] Novovent. 2002, *General catalogue*.

[99] Vad, J. *Advanced flow measurements.* University lecture note. Műegyetemi Kiadó, 2008. ID: 45085. ISBN 978 963 420 951 5.

[100] Testing and CFD study of Airius destratification fans. BSRIA Ltd. *Technical report*, 2007. available at www.airius.co.uk.

[101] Vad, J. Application of controlled vortex design concept to axial flow industrial fans. *Proc. GÉPÉSZET'2010 Konferencia (Conference on Mechanical Engineering)*, Budapest, 2010 (CD-ROM) (ISBN 978-963-313-007-0), Proceedings pp. 875-881.

[102] Vad, J. Fokozott fajlagos teljesítményű, energetikailag kedvező üzemű axiális átömlésű füstgázventilátorok tervezése és mérése (Design and measurement of axial flow flue gas extractor fans of high specific performance and energetically favourable operation). *GÉP*, 2010, **61** (11), pp. 15-18. (in Hungarian with English abstract)

[103] Vad, J., Kwedikha, A. R. A., Horváth, Cs., Balczó, M., Lohász, M. M., Régert, T. Aerodynamic effects of forward blade skew in axial flow rotors of controlled vortex design. *Proc. Instn Mech. Engrs, Part A, J. Power and Energy*, 2007, **221**, pp. 1011-1023.

[104] Stark, U., Bookjans, W., Mauß, M. Kennlinienberechnung für Axialventilatoren mit gesichelten Schaufeln. *Universität Karlsruhe*, *Fortschritt-Berichte VDI*, Reihe 7: Strömungstechnik, No. 356, VDI Verlag GmbH, Düsseldorf, 1999.

[105] Howell, A. R. The present basis of axial flow compressor design. 1942, British Aeronautical Research Council, Part I: *R. and M.* 2095, Part II: *R. A. E. Report* E 3961.

[106] Patterson G. N. Ducted fans. Design for high efficiency. Australian Council for Aeronautics. 1944, *Report* No. ACA 7

[107] Wallis, R. A. Wind tunnel tests on a series of circular arc plate airfoils. 1946, *A.R.L. Aero Note* 74.

[108] Carter, A. D. S., Hughes, H. P. A theoretical investigation into the effect of profile shape on the performance of aerofoils in cascade. 1946, British Aeronautical Research Council, *R. & M.* 2384.

[109] Cordier, O. Änlichkeitsbedingungen für Strömungsmaschinen. *Brennstoff-Wärme-Kraft*, 1952, **5**, No. 10.

[110] Lieblein, S. Experimental flow in two-dimensional cascades. Chapter VI in *Aerodynamic design of axial-flow compressors.* 1965, *Report NASA SP-36*, Washington D. C.

[111] Lewis, R. I., Hill, J. M. The influence of sweep and dihedral in turbomachinery blade rows. *J. Mechanical Engineering Science*, 1971, **13**, pp. 266-285.

[112] Pullan, G., Harvey, N. W. Influence of sweep on axial flow turbine aerodynamics at midspan. *ASME J. Turbomachinery*, 2007, **129**, pp. 591-598.

[113] Bogers, P. Investigation of the effects of sweep and dihedral on the development of compressor blade secondary losses. 1997, *Project Report* 1997-23, Von Karman Institute for Fluid Dynamics.

[114] Breugelmans, F. Experimental investigation of sweep and dihedral in compressors. 1999, In *Turbomachinery Design Systems*, Von Karman Institute for Fluid Dynamics, Belgium, Lecture Series 1999-02

[115] Denton, J. D., Xu, L. The exploitation of 3D flow in turbomachinery design. 1999, In *Turbomachinery Design Systems*, Von Karman Institute for Fluid Dynamics, Belgium, Lecture Series 1999-02.

[116] Chen, B., Yuan, X. Advanced aerodynamic optimization system for turbomachinery. *ASME J. Turbomachinery*, 2008, **130**, pp. 021005-1 to 021005-12.

[117] Van den Braembussche, R. A. Modern turbomachinery component design. *Conference on Modelling Fluid Flow (CMFF'06)*, Budapest, 2006, Proceedings pp. 33-48.

[118] Glas, W. Optimierung gepfeilter Pumpenschaufeln mit Evolutionären Algorithmen. *Doctoral Dissertation, Technische Universität Graz*, Institut for Hydraulische Strömungsmaschinen, 2000.

[119] Glas, W., Jaberg, H. Multi-objective evolutionary algorithm for the optimization of swept pump impellers. *4th European Conference on Turbomachinery Fluid Dynamics and Thermodynamics*, Florence, 2001, Proceedings pp. 469-479.

[120] Van den Braembussche, R. A., Sieverding, C. H., Maretto, L. A., Sabatini, A. Turbine stage optimization by means of a full 3D blade design concept. *4th European Conference on Turbomachinery Fluid Dynamics and Thermodynamics*, Florence, 2001, Proceedings pp. 217-226.

[121] Lampart, P. Numerical optimisation of a high pressure steam turbine stage. *Conference on Modelling Fluid Flow (CMFF'03)*, Budapest, 2003, Proceedings pp. 1238-1245.

[122] Seo, S.-J., Choi, S.-M., and Kim, K.-Y. Design optimization of a low-speed fan blade with sweep and lean. *Proc. Instn Mech. Engrs, Part A, J. Power and Energy*, 2008, **222**, pp. 87-92.

[123] Biollo, R., Benini, E. Aerodynamic behaviour of a novel three-dimensional shaped transonic compressor rotor blade. *ASME TURBO EXPO*, Berlin, 2008, *ASME Paper* GT2008-51397, CD-ROM Proceedings (ISBN 0-7918-3824-2)

[124] Samad, A., Kim, K.-Y. Stacking and thickness optimization of a compressor blade using weighted average surrogate model. *ASME TURBO EXPO*, Berlin, 2008, *ASME Paper* GT2008-50262, CD-ROM Proceedings (ISBN 0-7918-3824-2)

[125] Kristóf, G., Pap, E., Régert, T. CFD Simulation und PIV Messungen im Laufrad einer radialen Kreiselpumpe. *GALA Conference*, Winterthur, 2001, Proceedings pp. 29.1-29.6.

[126] Kristóf, G., Pöszmet, I., Fodor, G., Régert, T., Mezősi, B., Dávid, N. Numerical simulation of a side channel pump. *Conference on Modelling Fluid Flow (CMFF'03)*, Budapest, 2003, Proceedings pp. 997-1002.

[127] Lohász, M. M. Rambaud, P. Benocci, C. Flow features in a fully developed ribbed duct flow as a result of MILES. *Flow, Turbulence and Combustion,* 2006, **77**, pp. 59-76.

[128] Régert, T., Nagy, L., Balczó, M., Molnár, B. Investigation of the characteristics of turbulent boundary layer over an airfoil. *Conference on Modelling Fluid Flow (CMFF'06)*, Budapest, 2006, Proceedings pp. 225-232.

[129] Lohász, M. M., Nagy, L., Wurm, H. LES of the transitional flow in a miniature centrifugal pump. *Conference on Modelling Fluid Flow (CMFF'09)*, Budapest, Hungary, 2009, Proceedings pp. 826-832.

[130] Inoue, M., Kuroumaru, M. Three-dimensional structure and decay of vortices behind an axial flow rotating blade row. *ASME J. Engineering Gas Turbines Power*, 1984, **106**, pp. 561-569.

[131] Inoue, M., Kuroumaru, M., Fukuhara, M. Behavior of tip leakage flow behind an axial compressor rotor. *ASME J. Engineering Gas Turbines Power*, 1986, **108**, pp. 7-14.

[132] Nagl, G. Experimentelle Untersuchung der dreidimensionalen Strömung in einer Axialpumpe mit rotierenden Drucksonden. *Doctoral Dissertation, Technische Universität Graz, Institut for Hydraulische Strömungsmaschinen*, 1995.

[133] Furukawa, M., Inoue, M., Saiki, M., Yamada, K. The role of tip leakage vortex breakdown in compressor rotor aerodynamics. *ASME J. Turbomachinery*, 1999, **121**, pp. 469-480.

[134] Goltz, I., Kosyna, G., Wulff, D., Schrapp, H., Bross, S. Part load operating performance and stall inception of a single-stage axial-flow pump. *10th International Symposium on Transport Phenomena and Dynamics of Rotating Machinery (ISROMAC10)*, Honolulu, 2004, Proceedings CD-ROM, Paper No. 014.

[135] Wagner, J. H., Dring, R. P., Joslyn, H. D. Inlet boundary layer effects in an axial compressor rotor: Part I – Blade-to-blade effects. *ASME J. Engineering Gas Turbines Power*, 1985, **107**, pp. 374-380.

[136] Place, J. M. M., Cumpsty, N. A. *Comments* in [**55**], 1998.

[137] Vad, J. Analytical modeling of radial fluid migration in the boundary layer of axial flow turbomachinery blades. *ASME TURBO EXPO*, Barcelona, 2006, ASME Paper GT2006-90523, CD-ROM Proceedings (ISBN 0-7918-3774-2)

[138] Vad, J., Horváth, Cs. The impact of the vortex design method on the stall behavior of axial flow fan and compressor rotors. *ASME TURBO EXPO*, Berlin, 2008, ASME Paper GT2008-50333, CD-ROM Proceedings (ISBN 0-7918-3824-2)

[139] Vad, J. Radial fluid migration and endwall blockage in axial flow rotors. *Proc. Instn Mech. Engrs, Part A, J. Power and Energy*, **224**, pp. 399-417.

[140] Lesieur, M. *Turbulence in fluids.* 4th revised and enlarged edition, Springer, The Netherlands, 2008.

[141] Lakshminarayana, B., Davino, R., Pouagare, M. Three-dimensional flow field in the tip region of a compressor rotor passage – Part II: Turbulence properties. *ASME J. Engineering Power*, 1982, **104**, pp. 772-781.

[142] Albring, W. *Elementarvorgänge fluider Wirbelbewegungen.* Akademie-Verlag, Berlin, 1981.

[143] Lajos, T. *Fundamentals of fluid mechanics* (Az Áramlástan alapjai), Mackensen, Budapest, 2008 (in Hungarian) (ISBN 978 963 06 6382 3)

[144] Vad, J., Bencze, F. Three-dimensional flow in axial flow fans of non-free vortex design. *Int. J. Heat Fluid Flow*, 1998, **19**, pp. 601-607.

[145] Corsini, A., Rispoli, F. Flow analyses in a high-pressure axial ventilation fan with a non-linear eddy-viscosity closure. *Int. J. Heat Fluid Flow*, 2005, **26**, pp. 349-361.

[146] Vad, J., Bencze, F., Corsini, A., Rispoli, F. Non-free vortex flow effects in an axial flow rotor. *Periodica Polytechnica, Mechanical Engineering Series*, 2001, **45** (2), pp. 201-216.

[147] Vad, J., Koscsó, G., Gutermuth, M., Kasza, Zs., Tábi, T., Csörgő, T. Study of the aero-acoustic and aerodynamic effects of soft coating upon airfoil. *JSME Int. J., Series C - Mechanical Systems, Machine Elements and Manufacturing*, 2006, **49**, pp. 648-656.

[148] Pope, S. B. *Turbulent Flows.* Cambridge University Press, 2000.

[149] Inoue, M., Kuroumaru, M. Structure of tip clearance flow in an isolated axial compressor rotor. *ASME J. Turbomachinery*, 1989, **111**, pp. 250-256.

[150] Khalid, S. A., Khalsa, A. S., Waitz, I. A., Tan, C. S., Greitzer, E. M., Cumpsty, N. A., Adamczyk, J. J., Marble, F. E. Endwall blockage in axial compressors. *ASME J. Turbomachinery*, 1999, **121**, pp. 499-509.

[151] Corsini, A., Rispoli, F., Sheard, A. G. Development of improved blade tip endplate concepts for low-noise operation in industrial fans. *Proc. Instn Mech. Engrs, Part A, J. Power and Energy*, 2007, **221**, pp. 669-681.

[152] Corsini, A., Rispoli, F., Sheard, A. G. Aerodynamic performance of blade tip end-plates designed for low-noise operation in axial flow fans. *ASME J. Fluids Engineering*, 2009, **131**, pp. 1-13.

[153] Sanger, N. L., Shreeve, R. P. Comparison of the calculated and experimental cascade performance for controlled-diffusion compressor stator blading. *ASME J. Turbomachinery*, 1986, **108**, pp. 42-50.

[154] Ramakrishna, P. V., Govardhan, M. Study of sweep and induced dihedral effects in subsonic axial flow compressor passages – Part 1: Design considerations – changes in incidence, deflection, and streamline curvature. *Int. J. Rotating Machinery*, **2009**, Article ID 787145, 11 pages, doi: 10.1155/2009/787145.

[155] Ramakrishna, P. V., Govardhan, M. Study of sweep and induced dihedral effects in subsonic axial flow compressor passages – Part 2: Detailed study of the effects on tip leakage phenomena. *Int. J. Rotating Machinery*, **2010**, Article ID 491413, 13 pages, doi: 10.1155/2010/491413.

[156] Dunham, J. Modelling of spanwise mixing in compressor through-flow computations. *Proc. Instn Mech. Engrs, Part A, J. Power and Energy*, 1997, **211**, pp. 243-251.

[157] Cumpsty, N. A. Some lessons learned. *ASME J. Turbomachinery*, 2010, **132**, pp. 041018-1-7.

[158] Cros, S., Carbonneau, X. Computational study of the aerodynamic impact of stall margin improvements in a high tip speed fan. *Proc. 8th European Conference on Turbomachinery Fluid Dynamics and Thermodynamics (ETC'08)*, Graz, 2009, Proceedings pp. 401-410.

[159] Vad, J. Effects of sweep and spanwise changing circulation applied to airfoils: a case study. *J. Computational Applied Mechanics*, 2004, **5** (2), pp. 383-400.

[160] Vad, J. Correlation of flow path length to total pressure loss in diffuser flows. *Proc. Instn Mech. Engrs, Part A, J. Power and Energy*, 2011, **225**, pp. 481-496.

[161] Albring, W. *Angewandte Strömungslehre*. Akademie-Verlag, Berlin, 1978/90. (6., bearbeitete Auflage)

[162] Idel'cik, I. E. *Handbook of Hydraulic Resistance*. Jaico Publishing House, Delhi, 2008. (3nd Edition, 6th Jaico Impression).

[163] Zierep, J. *Strömungsmechanik*. Springer-Verlag Berlin Heidelberg New York, 1991.

[164] Vad, J., Kwedikha, A. R. A., Jaberg, H. Effects of blade sweep on the performance characteristics of axial flow turbomachinery rotors. *Proc. Instn Mech. Engrs, Part A, J. Power and Energy*, 2006, **220**, pp. 737-751.

[165] Koch, C. C. Stalling pressure rise capability of an axial compressor stage. *ASME J. Engineering Power*, 1981, **103**, pp. 645-656.

[166] Van den Braembussche, R. A. Design and optimisation of turbomachinery components. *Proc. 4th European Conference on Turbomachinery Fluid Dynamics and Thermodynamics*, Florence, Italy, 2001, Proceedings pp. 5-20.

[167] Weisstein, E. W. "Correlation Index." From *MathWorld* – A Wolfram Web Resource. http://mathworld.wolfram.com/CorrelationIndex.html.

[168] Gifford, N. L., Savory, E., Martinuzzi, R. J. Experimental study of automotive cooling fan aerodynamics. *SAE Paper* No. 2007-01-1525, 2007.

[169] Friedrichs, J., Baumgarten, S., Kosyna, G., Stark, U. Effect of stator design on stator boundary layer flow in a highly loaded single-stage axial-flow low-speed compressor. *ASME J. Turbomachinery*, 2001, **123**, pp. 483-489.

[170] Corsini, A., Rispoli, F., Vad, J. Iterative design of axial flow fans of high specific performance with swept blades. *Proc. 5th European Conference on Turbomachinery Fluid Dynamics and Thermodynamics (ETC'03)*, Prague, Czech Republic, 2003, Proceedings pp. 245-256.

[171] Lakshminarayana, B., Zaccaria, M., Marathe, B. The structure of tip clearance flow in axial flow compressors. *ASME J. Turbomachinery*, 1995, **117**, pp. 336-347.

[172] Weisstein, E. W. "Osculating Circle." From *MathWorld* – A Wolfram Web Resource. http://mathworld.wolfram.com/OsculatingCircle.html.

[173] Vad, J., Bencze, F., Corsini, A., Rispoli, F. Design aspects of three-dimensional flow in high performance axial flow ventilating fans. *6th International Symposium on Ventilation for Contaminant Control (VENTILATION'2000)*, Helsinki, 2000, Proceedings Vol. 1, pp. 108-110.

[174] Vad, J. Incorporation of forward blade sweep in the non-free vortex design method of axial flow turbomachinery rotors. *Periodica Polytechnica, Mechanical Engineering Series*, 2001, **45** (2), pp. 217-237.

[175] Vad, J., Corsini, A. Comparative investigation on axial flow industrial fans of high specific performance with unswept and forward swept blades at design and off-design conditions. 9th International Symposium on *Transport Phenomena and Dynamics of Rotating Machinery (ISROMAC9)*, Honolulu, 2002, CD-ROM Proceedings, Paper No. FD-ABS-016. Proc. Abstracts p. 301.

[176] Vad, J. Iterative design of high performance axial flow rotors with forward-swept blades. *GÉPÉSZET'2002 Konferencia (Conference on Mechanical Engineering)*, Budapest, 2002, Proceedings Vol. 2, pp. 679-683.

[177] Fáy, Á. Computation of pump characteristics. *Conference on Modelling Fluid Flow (CMFF'03)*, Budapest, 2003, Proceedings pp. 933-941.

[178] Horlock, J. H., Denton, J. D. A review of some early design practice using computational fluid dynamics and a current perspective. *ASME J. Turbomachinery*, 2005, **127**, pp. 5-13.

[179] Howell, A. R., Mettam, M., Nock, J. Some general notes on axial flow compressor design. *Power Jets Report* R1088, 1945.

[180] Cox, Sir H. Roxbee (Editor). *Gas turbine principles and practice*. George Newnes. London. 1955. Chapter 5.

[181] Korn, G. A., Korn, T. M. *Mathematical handbook for Scientists and Engineers.* McGraw-Hill Book Company, New York-San Francisco-Toronto-London-Sydney, 1967. (2nd Edition).

[182] Corsini, A. *Private communication*, 2010.

[183] Cooke, J. C. An axially symmetric analogue for general three-dimensional boundary layers. *R &M. No. 3200 (21,386), A. R. C. Technical Report*, 1961.

[184] Lakshminarayana, B. Methods of predicting the tip clearance effects in axial flow turbomachinery. *ASME J. Basic Engineering*, September 1970, pp. 467-482.

[185] Dixon, S. L. *Fluid mechanics and thermodynamics of turbomachinery*. Butterworth Heinemann, Boston-Oxford-Johannesburg-Melbourne-New Delhi-Singapore, 1998. (4th Edition).

[186] Khoshmanesh, S. Experimental data analysis of five Moore 10000 class fans used in air cooled heat exchangers. *ARPN J. Engineering and Applied Sciences*, 2009, **4**, pp. 38-43.

[187] Rossetti, A., Ardizzon, G., Pavesi, G., Cavazzini, G. An optimum design procedure for an aerodynamic radial diffuser with incompressible flow at different Reynolds numbers. *Proc. Instn Mech. Engrs, Part A, J. Power and Energy*, 2010, **224**, pp. 69-84.

[188] Templalexis, I., Pilidis, P., Pachidis, V., Kotsiopoulos, P. Development of a two-dimensional streamline curvature code. *ASME J. Turbomachinery*, 2011, **133**, pp. 011003-1 to 011003-7.

[189] Sarraf, C., Nouri, H., Ravelet, F., Bakir, F. Experimental study of blade thickness on the overall and local performances of a controlled vortex designed axial-flow fan. *Experimental Thermal and Fluid Science*, 2011, **35**, pp. 684-693.

[190] Van den Braembussche, R. A., Vad, J. Challenges in optimisation of axial flow turbomachinery blades for 3D flow, including sweep and dihedral effects. In: Vad, J., Lajos, T., Schilling, R. (Eds.), *Modelling Fluid Flow - State of the Art,* Springer Verlag Heidelberg, 2004, pp. 99-103.

[191] Ramakrishna, P. V., Govardhan, M. On loading corrections and loss distributions in low-speed forward swept axial compressor rotors. *Proc. Institution of Mechanical Engineers – Part A: Journal of Power and Energy*, 2011, **225**, pp. 120-130.

[192] Czibere, T., Füzy, O., Hajdú, S., Nyíri, A., Vajna, Z. Nemzetközi tudományos helyzetkép az áramlástechnikai gépekkel kapcsolatos kutatásokról. (International scientific overview related to research applied to fluid machinery) *Műszaki Tudomány*, 1970, **42**, pp. 221-231. (in Hungarian)

[193] Füzy, O. *Áramlástechnikai gépek és rendszerek*. (*Fluid machinery and fluids engineering systems*) Tankönyvkiadó, Budapest, 1991 (in Hungarian)

[194] Hős, Cs., Champneys, A., Kullmann, L. Bifurcation analysis of surge and rotating stall in the Moore-Greitzer compression system. *IMA Journal of Applied Mathematics*, 2003, **68** (2), pp. 205-228.

[195] Kovács, L. *Vegyipari szivattyúk és gázsűrítők*. (*Chemical industry pumps and compressors*) Műegyetemi Kiadó, Budapest, 1993 (in Hungarian)

7. APPENDICES

• *Appendix A. Obtainment of derivative vectors*

For the derivations, $x(t) = r \cos t$ and $y(t) = r \sin t$ are considered (Fig. 2.1). Furthermore, it is conceivable using **Figure A1.a)** that according to the change of the independent parameter by dt, the streamline develops in the circumferential direction approximately by the arc length of $r\,dt$, and in the axial direction by dz. Since $(r\,dt)/dz = \tan\alpha$, the relationship $dz/dt = z' = r/\tan\alpha$ is applied.

For expression of dr/dt appearing in the derivatives, let us define a coordinate axis s, with unit vector $\underline{u}_s$, being tangential to the projection of the streamline onto the cylindrical surface of radius r. **Figure A1.b)** illustrates that $ds = dz/\cos\alpha$ and $\tan\varepsilon = dr/ds$. These relationships, together with $dz = (r\,dt)/\tan\alpha$, read $(dr/dt) = (r\tan\varepsilon)/\sin\alpha$.

As **Figure A1.c)** illustrates, a normal coordinate axis n, with unit vector $\underline{u}_n$, is defined, by such means that $\underline{u}_r \times \underline{u}_n = \underline{u}_s$. R_α is the radius of curvature of the projection of the streamline onto the $[n, s]$ plane (α can also be measured on the $[n, s]$ plane). As suggested by the figure, $ds = R_\alpha(-d\alpha)$ and, therefore, $d\alpha/ds = -(1/R_\alpha)$. (Viewed from the direction opposite to $\underline{u}_n$, the streamline segment is convex.)

As Fig. 2.1 suggests, the value of $t = t_P = \pi/2$ is to be substituted in order to obtain the derivative vectors for P. It has been considered that r, α, and ε depend on t, and R_α has been approximated as constant (circular arc streamline segment). Carrying out the first and second derivations, considering the former relationships, and substituting t_P reads after several steps of transformation and simplification

$$\underline{h}'_{\mathrm{P}} = \begin{bmatrix} x'_{\mathrm{P}} \\ y'_{\mathrm{P}} \\ z'_{\mathrm{P}} \end{bmatrix} = r \begin{bmatrix} -1 \\ \tan\varepsilon / \sin\alpha \\ 1/\tan\alpha \end{bmatrix} \tag{A.1}$$

$$\underline{h}''_{\mathrm{P}} = \begin{bmatrix} x''_{\mathrm{P}} \\ y''_{\mathrm{P}} \\ z''_{\mathrm{P}} \end{bmatrix} = r \begin{bmatrix} -2\dfrac{\tan\varepsilon}{\sin\alpha} \\ \dfrac{1}{\sin^2\alpha}\left[\dfrac{\partial(\tan\varepsilon)}{\partial s} r + \dfrac{\tan\varepsilon}{\tan\alpha}\dfrac{r}{R_\alpha} + \tan^2\varepsilon\right] - 1 \\ \dfrac{1}{\sin\alpha}\left(\dfrac{\tan\varepsilon}{\tan\alpha} + \dfrac{r}{R_\alpha}\dfrac{1}{\sin^2\alpha}\right) \end{bmatrix} \tag{A.2}$$

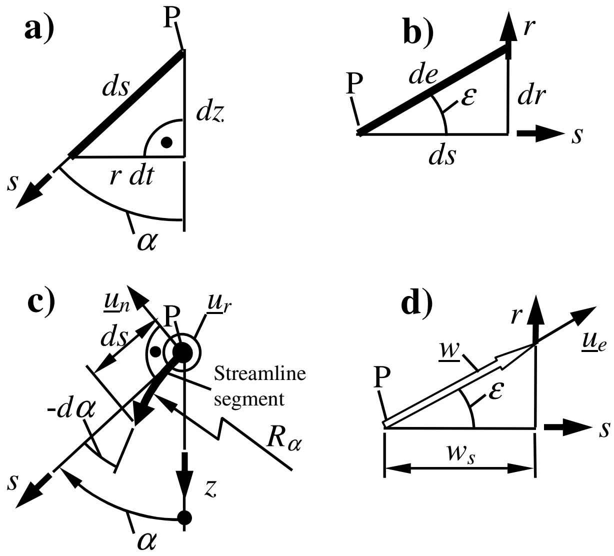

Figure A.1. *Geometrical and kinematic details*

- ***Appendix B.*** ***Obtainment of centripetal acceleration***

The curvature of the streamline is

$$g = \frac{\left|\underline{h}'_{\mathrm{P}} \times \underline{h}''_{\mathrm{P}}\right|}{\left|\underline{h}'_{\mathrm{P}}\right|^3} \tag{B.1}$$

The unit vector pointing from P toward the centre of the osculating circle [**172**] related to P is

$$\underline{k} = \frac{\left(\underline{h}'_{\mathrm{P}} \times \underline{h}''_{\mathrm{P}}\right) \times \underline{h}'_{\mathrm{P}}}{\left|\left(\underline{h}'_{\mathrm{P}} \times \underline{h}''_{\mathrm{P}}\right) \times \underline{h}'_{\mathrm{P}}\right|} \tag{B.2}$$

The centripetal acceleration is

$$\underline{a}_{\mathrm{cp}} = w^2 \, g \, \underline{k} \tag{B.3}$$

Since $\underline{h}'_{\mathrm{P}}$ and $\underline{h}'_{\mathrm{P}} \times \underline{h}''_{\mathrm{P}}$ are perpendicular,

$$\left|\left(\underline{h}'_{\mathrm{P}} \times \underline{h}''_{\mathrm{P}}\right) \times \underline{h}'_{\mathrm{P}}\right| = \left|\underline{h}'_{\mathrm{P}} \times \underline{h}''_{\mathrm{P}}\right| \cdot \left|\underline{h}'_{\mathrm{P}}\right| = g \cdot \left|\underline{h}'_{\mathrm{P}}\right|^4 \tag{B.4}$$

The substitution of Eq. (B.4) to Eq. (B.3) reads Eq. (2.1).

- ***Appendix C. Notes on the model of "outward centrifugation"***

Based on [**1**], the model of "outward centrifugation" is described as follows. Let us assume that the simplified radial equilibrium equation is satisfied in the core flow region:

$$\frac{1}{\rho}\frac{\partial P}{\partial r}-\frac{1}{r}V_u^{\,2}=0 \tag{C.1}$$

Furthermore, it is assumed in [**1**] as an approximation that the radial pressure gradient in the core flow is also valid for the boundary layer, on the basis of Prandtl's boundary layer hypothesis:

$$\frac{\partial P}{\partial r}\approx\frac{\partial p}{\partial r} \tag{C.2}$$

As the blade surface is approached, the absolute tangential velocity in the boundary layer approaches the circumferential velocity of the blade of solid body rotation, i.e. $v_u > V_u$. This implies that

$$\frac{1}{r}v_u^{\,2} > \frac{1}{r}V_u^{\,2}=\frac{1}{\rho}\frac{\partial P}{\partial r}\approx\frac{1}{\rho}\frac{\partial p}{\partial r} \tag{C.3}$$

This imbalance indicates that the centrifugal force in the boundary layer, $\rho\, v_u^2 /r$, is larger than the radial pressure gradient, resulting in the development of outward radial velocity ("centrifuging outward" in [**19, 31, 70, 135, 154, 191**]). Following the above view, the sum of terms

$$\frac{1}{r}\left(v_u^{\,2}-V_u^{\,2}\right)+\frac{1}{\rho}\left[\frac{\partial P}{\partial r}-\frac{\partial p}{\partial r}\right] \tag{C.4}$$

on the right-hand side of Eq. (2.15) is positive, thus increasing μ, i.e. stimulating radial outward fluid migration.

- ***Appendix D. Notes on normal-wise coupling of equations of motion***

The following approximation is made, by applying a first-order approximation of the Taylor series of the pressure function:

$$P(r)=p(r)+\int_0^N\frac{\partial p}{\partial n}(r)dn \tag{D.1}$$

$$P(r+dr)=P(r)+\frac{\partial P}{\partial r}dr=p(r+dr)+\int_0^N\frac{\partial p}{\partial n}(r+dr)dn=$$

$$=p(r)+\frac{\partial p}{\partial r}dr+\int_0^N\left[\frac{\partial p}{\partial n}(r)+\frac{\partial}{\partial r}\left(\frac{\partial p}{\partial n}\right)dr\right]dn \tag{D.2}$$

Subtracting Eq. (D.1) from Eq. (D.2), rearranging and dividing the result by dr, considering it constant, leads to Eq. (2.16).

- ***Appendix E. Obtainment of n-wise acceleration***

The streamwise acceleration in Eq. (2.5) has no n-wise component. Based on Eq. (2.1), the x-wise and z-wise components of $\underline{a}_{cp}$ are expressed, and the sum of their projections onto $\underline{u}_n$ are considered as a_n. Similarly to Eq. (2.2), it can be pointed out that

$$\left[\left(\underline{h}'_{p}\times\underline{h}''_{p}\right)\times\underline{h}'_{p}\right]_x=\left[\left(y'^2+z'^2\right)x''-\left(y'\,y''+z'\,z''\right)x'\right]_p \tag{E.1}$$

$$\left[\left(\underline{h}'_{p}\times\underline{h}''_{p}\right)\times\underline{h}'_{p}\right]_z=\left[\left(x'^2+y'^2\right)z''-\left(x'\,x''+y'\,y''\right)z'\right]_p \tag{E.2}$$

Utilising Eq. (2.1) and Figs. 2.1 and A1:

$$a_n=-\frac{w^2}{\left|\underline{h}'_{p}\right|^4}\left\{\left[\left(\underline{h}'_{p}\times\underline{h}''_{p}\right)\times\underline{h}'_{p}\right]_x\cos\alpha+\left[\left(\underline{h}'_{p}\times\underline{h}''_{p}\right)\times\underline{h}'_{p}\right]_z\sin\alpha\right\} \tag{E.3}$$

Substituting the derivatives from Appendix A into Eqs. (E.1) and (E.2), substituting these equations into Eq. (E.3), and utilising Eq. (2.3) lead to Eq. (2.19), after several steps of transformations and trigonometric simplifications, and considering that $w\cos\varepsilon=w_s$ and $w_s\sin\alpha=w_u$.

- ***Appendix F. Practical aspects of fixing the inlet and outlet geometry and mean velocity vectors; efficiency and total pressure loss coefficient definitions***

Fixing the inlet and outlet geometrical characteristics means the following.

- For Q1D – conical – diffuser flows: fixing the diffuser inlet and outlet diameters D_{D1} and D_{D2}.
- For 2D blade cascade flows: fixing the blade spacing s_b.
- For 3D blade cascade flows: fixing the blade spacing s_b at mid-radius of the portion of blade span under investigation.

The fixed inlet and outlet mean velocity vectors, manifesting the user demand, correspond to the following.

- For Q1D diffuser flows: prescribed mass-averaged isentropic mean static pressure rise Δp_{is}, associated with the inlet and outlet velocity, on the basis of the Bernoulli equation.
- For 2D blade cascade flows, as well as for 3D stator flows at a given spanwise position: prescribed inlet and outlet flow angles α_1 and α_2, i.e. prescribed turning; and prescribed mass-averaged isentropic mean static pressure rise Δp_{is}.
- For 3D rotor blade cascade flows: prescribed inlet and outlet flow angles α_1 and α_2 at mid-radius of the portion of blade span under investigation, i.e. prescribed turning; and prescribed mass-averaged isentropic mean total pressure rise $\Delta p_{t\,is}$ as well as Euler work.

The total pressure loss $\Delta p'_{\mathrm{t}}$ is intended to be moderated for such prescribed isentropic conditions. This gives a means for the following benefits.

- For Q1D diffuser flows, and in 2D as well as 3D stator cascade flows (for the latter, at a given averaged spanwise position): improvement of diffuser efficiency [**143, 161**], leading to gain in Δp at given diffusion:

$$\eta_{\mathrm{D}} = \frac{\Delta p}{\Delta p_{\mathrm{is}}} = \frac{\Delta p_{\mathrm{is}} - \Delta p'_{\mathrm{t}}}{\Delta p_{\mathrm{is}}} = 1 - \frac{\Delta p'_{\mathrm{t}}}{\Delta p_{\mathrm{is}}} \tag{F.1}$$

- In 3D rotor cascade flows, at a given averaged spanwise position: improvement of local total efficiency (detailed explanation in [**164**]), leading to gain in Δp_{t} at a given Euler work input:

$$\eta_{\mathrm{t}} = \frac{\Delta p_{\mathrm{t}}}{\Delta p_{\mathrm{t\,is}}} = \frac{\Delta p_{\mathrm{t\,is}} - \Delta p'_{\mathrm{t}}}{\Delta p_{\mathrm{t\,is}}} = 1 - \frac{\Delta p'_{\mathrm{t}}}{\Delta p_{\mathrm{t\,is}}} \tag{F.2}$$

As explained in [**164**], the local total efficiency is defined for an annular elementary rotor cascade as product of local volume flow rate through the elementary cascade and total pressure rise realized locally by the elementary cascade, divided by the mechanical power input necessary for driving the elementary cascade. After simplifying assumptions, the local total efficiency can be expressed as $\eta_{\mathrm{t}} = \Delta p_{\mathrm{t}} / \Delta p_{\mathrm{t\,is}}$. The local efficiency is used in the technical literature for characterising the local energetic behaviour of rotors along the span, e.g. [**122**].

Following the methodology in [**26, 95, 110**], the total pressure loss will be normalized by the inlet dynamic head for each case (Q1D, 2D as well as 3D flows), resulting in the loss coefficient ω'

$$\omega'_{v} = \frac{\Delta p'_{\mathrm{t}}}{\rho v_1^2 / 2} \quad \text{for Q1D, 2D and stator 3D flows;} \tag{F.3a}$$

$$\omega'_{w} = \frac{\Delta p'_{\mathrm{t}}}{\rho w_1^2 / 2} \quad \text{for 3D rotor flows.} \tag{F.3b}$$

• *Appendix G. Notes on the Reynolds number*

For judgment of the ratio between inertial and viscous forces, the Reynolds number can be theoretically defined on the basis of the true flow path length L:

$$\mathrm{Re} = \mathrm{Re}_L = \frac{L \cdot w_\infty}{\nu} \tag{G.1}$$

For cascade flows, the suction peak is located in the vicinity of the leading edge, especially for traditional blade profiles (e.g. NACA, *C4*, double-circular-arc) [**1**]. Thus, the order of magnitude of L is tailored by the chord length c. In reference [**165**], cited in [**1**], the diffusion length has been taken as the length of the circular arc camber line characterised by c and θ.

$$L \approx \left(\frac{c}{2}\Big/\sin\frac{\theta}{2}\right)\cdot\theta\cdot\frac{2\pi}{360} \tag{G.2}$$

In the turbomachinery community, the blade Reynolds number is defined even in a simpler manner, using the approximation $L \approx c$ [**72, 74, 110**]:

$$\mathrm{Re} = \mathrm{Re}_c = \frac{c\cdot w_\infty}{\nu} \tag{G.3}$$

As mentioned in [**110**], the loss variation with Re is associated primarily with the separation of laminar boundary layer. It is recommended to fulfil the condition $\mathrm{Re}_c > 1.5\cdot10^5$ [**74**] for moderation of loss. Even higher critical Reynolds numbers are set in other references [**86, 110**], up to $2.5\cdot10^5$. It is assumed that the critical Reynolds number is significantly exceeded for the applications discussed herein. This ensures that even if L varies in a comparative case study, e.g. due to 3D flow effects, the resultant modification in Re_L will not cause in itself the modification of the loss. Therefore, the Reynolds number effect, associated primarily with laminar separation, is excluded from the case studies discussed herein.

- ***Appendix H. Notes on geometrical data of conical diffusers; obtainment of total pressure loss coefficient for end-diffusers***

For conical diffusers, L is approximated herein as follows. For the geometrical representation of the diffusers, see the sketch in **Figure 3.2**.

$$L = \frac{\ell}{\cos\vartheta} \qquad \text{where} \qquad \vartheta = \tan^{-1}\frac{D_{D2}-D_{D1}}{2\ell} \tag{H.1}$$

Reference [**161**] presents the diffuser efficiency by considering the outlet dynamic head as a loss, leading to an efficiency definition $\eta_{\mathrm{D\,end}}$ being different from the one given in Eq. (F.1). Such efficiency is characteristic of free-exhausting diffusers, termed "end-diffusers".

$$\eta_{\mathrm{Dend}} = \frac{\Delta p - \rho v_2^2/2}{\Delta p_{\mathrm{is}}} = \frac{\Delta p_{\mathrm{is}} - \Delta p'_{\mathrm{t}} - \rho v_2^2/2}{\Delta p_{\mathrm{is}}} = 1 - \frac{\Delta p'_{\mathrm{t}} + \rho v_2^2/2}{\Delta p_{\mathrm{is}}} = 1 - \frac{\Delta p'_{\mathrm{t}} + (D_{\mathrm{D1}}/D_{\mathrm{D2}})^4(\rho v_1^2/2)}{(\rho v_1^2/2)\left[1-(D_{\mathrm{D2}}/D_{\mathrm{D1}})^{-4}\right]} =$$

$$= 1 - \frac{\omega'_v}{\left[1-(D_{\mathrm{D2}}/D_{\mathrm{D1}})^{-4}\right]} - \frac{(D_{\mathrm{D2}}/D_{\mathrm{D1}})^{-4}}{\left[1-(D_{\mathrm{D2}}/D_{\mathrm{D1}})^{-4}\right]} \tag{H.2}$$

The above equation expresses Δp_{is} using the Bernoulli and continuity equations as a function of the inlet dynamic head and $D_{\mathrm{D2}}/D_{\mathrm{D1}}$. Eq. (F.3a) was considered for inclusion of ω'_v. Reference

[**161**] presents $\eta_{\text{D end}}$ (p. 290, Fig. 21.30) as a function of ℓ/D_{D1} and $D_{\text{D2}}/D_{\text{D1}}$, for a given Reynolds number, on the basis of measurements. The experimental data were post-processed herein as follows. $D_{\text{D2}}/D_{\text{D1}}$ was fixed for a comparative case study. L/D_{D1} was expressed using Eq. (H.1) for various ℓ/D_{D1} data. By rearranging Eq. (H.2), ω_v was calculated as a function of L/D_{D1}, using the experiment-based $\eta_{\text{D end}}$ data.

- ***Appendix J. Details of 2D cascade concept***

In what follows, aerodynamic aspects of the 2D concept, represented by classic measurement data, e.g. [**105, 108, 110**] and used in rotor design, are discussed. **Figure J.1** illustrates the discussion (Fig. J.1a for 2D flow), and **Table J.1** summarizes the mathematical relationships. Fig. J.1 and Table J.1 will be referred to later on as well, when commenting on the adaptation of the 2D concept in Q2D and Q3D approaches of rotor flow, in Appendix M. The expressions in the rows of the table will be referenced as usual for equations, using the numerals specified in the last column, **Eqs. J.1a to J.8c**. For simplicity, the uniformized notation specified in **Table J.2** is used for 2D and rotor flows. Use of the symbols " ≈ " in Table J.1 indicates approximate assumptions.

Table J.1. *Adaptation of 2D data in Q2D and Q3D rotor approaches: comparative features, and assumptions*

Feature	2D approach: a)	Q2D rotor approach: b)	Q3D rotor approach: c)	Ref. #
Spanwise flow	$v_r \equiv 0,\ \partial/\partial r \equiv 0$	$v_r \neq 0, v_r \approx 0,$ $r_1 = r_2 = r_{12}$	$v_r \neq 0,\ v_r \approx \hat{v}_{z12} \tan\beta,$ $r_1 \neq r_2,\ r_{12} = (r_1+r_2)/2$	J.1a-c
Mass conservation consideration	$dq_{\text{V1}} = dq_{\text{V2}}$	$\hat{v}_{z12} r_{12} dr_{12} \approx \hat{v}_{z2} r_2 dr_2$	$\hat{v}_{z12} r_{12} dr_{12} \approx \hat{v}_{z2} r_2 dr_2$	J.2a-c
$\hat{v}_z$	$\hat{v}_{z1} = \hat{v}_{z2}$	$\hat{v}_{z1} \neq \hat{v}_{z2}$	$\hat{v}_{z1} \neq \hat{v}_{z2}$	J.3a-c
$\hat{v}_{z12}$	$\hat{v}_{z12} = \hat{v}_{z1} = \hat{v}_{z2}$	$\hat{v}_{z12} \approx (\hat{v}_{z1} + \hat{v}_{z2})/2$	$\hat{v}_{z12} \approx (\hat{v}_{z1} + \hat{v}_{z2})/2$	J.4a-c
A_{sI}, A_{sII}: Consideration of momentum	$\left[\int_{A_{\text{sI}}, A_{\text{sII}}} \underline{v}\rho(\underline{v}\, d\underline{A}_{\text{s}})\right]_u = 0$	$\left[\int_{A_{\text{sI}}, A_{\text{sII}}} \underline{r} \times [\underline{v}\rho(\underline{v}\, d\underline{A}_{\text{s}})]\right]_z \approx 0$	$\left[\int_{A_{\text{sI}}, A_{\text{sII}}} \underline{r} \times [\underline{v}\rho(\underline{v}\, d\underline{A}_{\text{s}})]\right]_z \approx 0$	J.5a-c
A_{sI}, A_{sII}: Consideration of shear stress	$\left[\int_{A_{\text{sI}}, A_{\text{sII}}} \underline{\tau} \lvert d\underline{A}_{\text{s}} \rvert\right]_u = 0$	$\left[\int_{A_{\text{sI}}, A_{\text{sII}}} \underline{r} \times \underline{\tau} \lvert d\underline{A}_{\text{s}} \rvert\right]_z \approx 0$	$\left[\int_{A_{\text{sI}}, A_{\text{sII}}} \underline{r} \times \underline{\tau} \lvert d\underline{A}_{\text{s}} \rvert\right]_z \approx 0$	J.6a-c
dA_{s1}, dA_{s2}: Consideration of momentum	$\left[\int_{dA_{\text{s1}}, dA_{\text{s2}}} \underline{v}\rho(\underline{v}\, d\underline{A}_{\text{s}})\right]_u =$ $= \rho\, dr\, s_{\text{b}} \hat{v}_{z12} (\hat{v}_{u1} - \hat{v}_{u2})$	$\left[\int_{dA_{\text{s1}}, dA_{\text{s2}}} \underline{r} \times [\underline{v}\rho(\underline{v}\, d\underline{A}_{\text{s}})]\right]_z =$ $= -2 r_2^2 \pi\, dr_2\, \rho\, \hat{v}_{z2} \hat{v}_{u2}$	$\left[\int_{dA_{\text{s1}}, dA_{\text{s2}}} \underline{r} \times [\underline{v}\rho(\underline{v}\, d\underline{A}_{\text{s}})]\right]_z =$ $= -2 r_2^2 \pi\, dr_2\, \rho\, \hat{v}_{z2} \hat{v}_{u2}$	J.7a-c
dA_{s1}, dA_{s2}: Consideration of shear stress	$\left[\int_{dA_{\text{s1}}, dA_{\text{s2}}} \underline{\tau} \lvert d\underline{A}_{\text{s}} \rvert\right]_u \approx 0$	$\left[\int_{dA_{\text{s1}}, dA_{\text{s2}}} \underline{r} \times \underline{\tau} \lvert d\underline{A}_{\text{s}} \rvert\right]_z \approx 0$	$\left[\int_{dA_{\text{s1}}, dA_{\text{s2}}} \underline{r} \times \underline{\tau} \lvert d\underline{A}_{\text{s}} \rvert\right]_z \approx 0$	J.8a-c

Table J.2. *Uniformized notation for 2D and rotor flows*

Notation	2D flow	Rotor flow
r	Spanwise coordinate	Radial coordinate
$\underline{u}_r$	Spanwise unit vector	Radial unit vector (Ch. 2)
$\underline{u}_u$	Pitchwise unit vector	Tangential unit vector (Ch. 2)
$\underline{u}_z$	$\underline{u}_u \times \underline{u}_r = \underline{u}_z$	$\underline{u}_u \times \underline{u}_r = \underline{u}_z$ Axial unit vector (Ch. 2)
1, 2	Inlet and outlet sections, parallel to the [$\underline{u}_u$, $\underline{u}_r$] plane	
CV	Elementary control volume: extended to one pitch for 2D flow; axisymmetric for rotor flow	
dA_{s1}, dA_{s2}	Elementary surfaces bounding the control volume and fitting to the inlet and outlet sections	
A_{sI}, A_{sII}	Surfaces bounding the control volume, at a distance dr_{12} from each other in r direction at mid-chord	

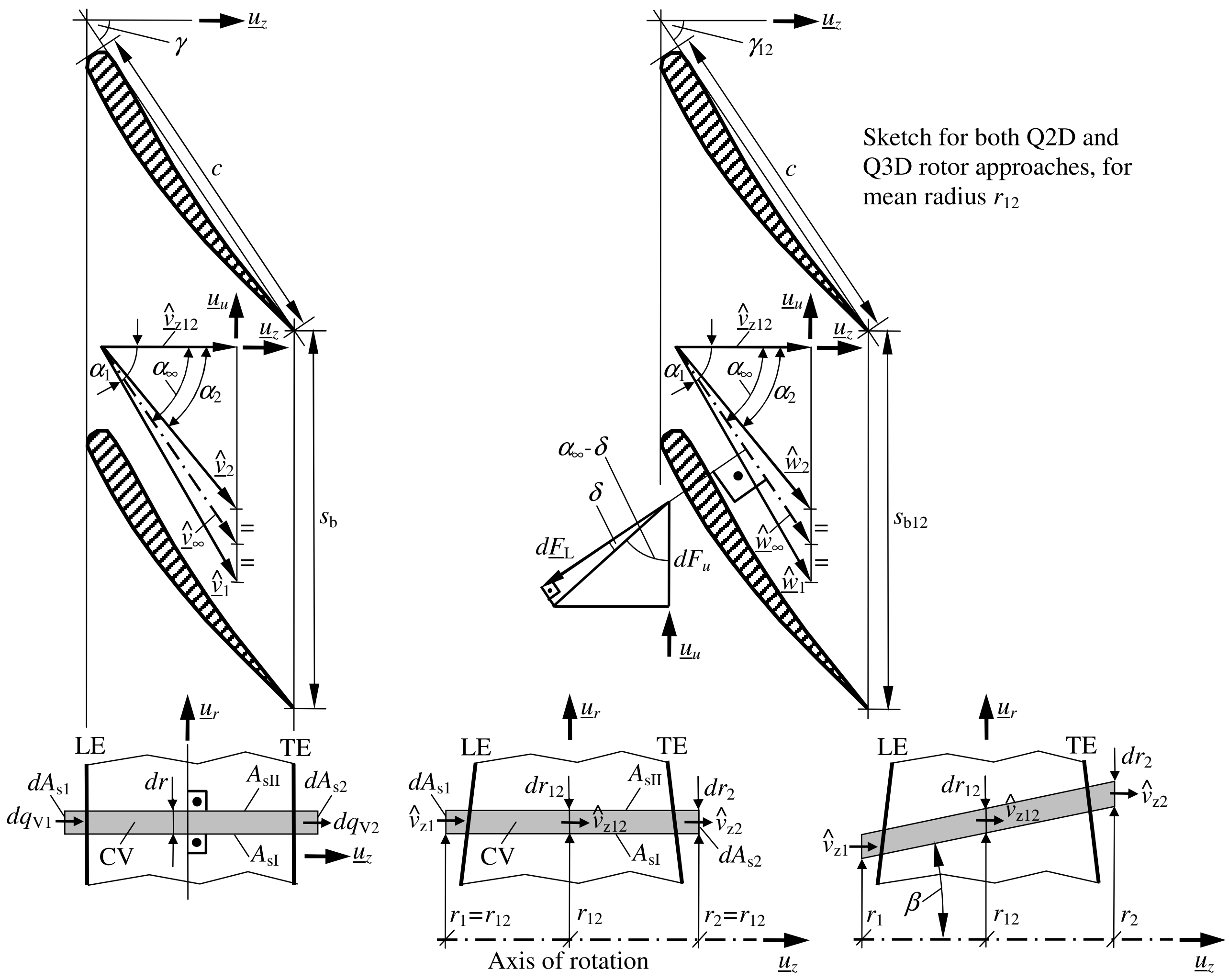

a)
2D cascade flow

b)
Q2D rotor approach

c)
Q3D rotor approach

Figure J.1. *Comparative sketches on 2D, Q2D and Q3D approaches. CV: control volume. LE: leading edge. TE: trailing edge.*

In the case of 2D flow, no spanwise velocity component develops, and the spanwise change of any quantity is zero (Eq. J.1a). According to the lack of spanwise flow, A_{sI} and A_{sII} are stream surfaces. With consideration of incompressibility, the conservation of mass implies equal inlet and outlet elementary volume flow rates (Eq. J.2a). Accordingly, the pitch-averaged z-wise velocity components are equal at inlet and outlet (Eq. J.3a), and this z-wise velocity represents the mean z-wise velocity through the blading as well (Eq. J.4a).

For later use, the momentum fluxes and forces playing role in the pitchwise component of the linear momentum equation applied to the control volume are discussed. The pitchwise momentum fluxes over A_{sI} and A_{sII} are zero (Eq. J.5a), given that the elementary volume flow rates $\underline{v}d\underline{A}_s$ through these surfaces are zero. The pitchwise forces originating from shear stresses over A_{sI} and A_{sII} are zero (Eq. J.6a), given that the shear stresses developing over these surfaces are zero, due to the lack of spanwise velocity gradients, in accordance with the $\partial/\partial r \equiv 0$ condition in Eq. J.1a. The pitchwise forces originating from shear stresses over dA_{s1} and dA_{s2} are neglected, e.g. [**74**] (Eq. J.8a). This neglect is reasonable in the view of near-zero velocity gradients at inlet, and only moderate velocity gradients farther downstream of the cascade.

The pitchwise momentum fluxes over dA_{s1} and dA_{s2} are as follows (Table J.1 for Eq. J.7a):

$$\left[\int_{dA_{s1},dA_{s2}} \underline{v}\rho\left(\underline{v}\,d\underline{A}_s\right)\right]_u = \int_{dA_{s1}}(-v_u)\rho(-v_z dr\,ds_b) + \int_{dA_{s2}}(-v_u)\rho(v_z dr\,ds_b) =$$

$$= \rho\,dr\,s_b\hat{v}_{z12}\left(\hat{v}_{u1}-\hat{v}_{u2}\right) = \rho\,dq_V\left(\hat{v}_{u1}-\hat{v}_{u2}\right) = \rho\,dr\,\hat{v}_{z12}\Gamma \qquad \text{(J.7a)}$$

where blade circulation is approximated using the pitch-averaged pitchwise velocity components (see Appendix K) as follows, e.g. [**1**].

$$\Gamma = \oint \underline{v}\,d\underline{\ell} \approx s_b\left(\hat{v}_{u1}-\hat{v}_{u2}\right) \qquad \text{(J.9)}$$

The free-stream flow angle is calculated as follows (conf. Eq. 3.1) [**1**].

$$\alpha_\infty = \tan^{-1}\frac{\left(\hat{v}_{u1}+\hat{v}_{u2}\right)/2}{\hat{v}_{z12}} = \tan^{-1}\frac{\tan\alpha_1+\tan\alpha_2}{2} = \sin^{-1}\frac{\left(\hat{v}_{u1}+\hat{v}_{u2}\right)/2}{\hat{v}_\infty} = \cos^{-1}\frac{\hat{v}_{z12}}{\hat{v}_\infty} \qquad \text{(J.10)}$$

Eq. (J.10) provides a definition also for the free-stream velocity $\hat{v}_\infty$.

- ***Appendix K. Notes on pitchwise averaging***

A) In Eq. (J.3a) (Table J.1), the pitch-averaged z-wise velocities at dA_{s1} and dA_{s2} have been obtained as follows, using the general definition of volume flow rate $q_V = \int_{A_s}\underline{v}\,d\underline{A}_s$:

$$\hat{v}_{zi} = \frac{dq_{Vi}}{dA_{si}} = \frac{\int_{dA_{si}} v_z\left(dr\,ds_b\right)}{dr\,s_b} = \frac{dr\int_{s_b} v_z ds_b}{dr\,s_b} = \frac{\int_{s_b} v_z ds_b}{s_b} \qquad \text{(K.1)}$$

As a generalization of Eq. (K.1), *pitchwise area-averaging* is considered herein whenever $\hat{v}_z$ or $\hat{\varphi}$ appear.

B) In Eq. (J.7a), the pitch-averaged u-wise velocities at dA_{s1} and dA_{s2} have been obtained as follows:

$$\hat{v}_{ui} = \frac{\int_{dA_{si}} v_{ui}\rho\left(v_z dr\, ds_b\right)}{\rho\, dq_{Vi}} = \frac{\int_{dA_{si}} v_{ui}\rho\left(v_z dr\, ds_b\right)}{\int_{dA_{si}} \rho\left(v_z dr\, ds_b\right)} = \frac{\int_{dA_{si}} v_{ui}\rho\left(v_z dr\, ds_b\right)}{\rho\, dr\, s_b \hat{v}_{zi}} \tag{K.2}$$

As a generalization, *pitchwise mass-averaging* is considered herein whenever $\hat{v}_u$, $\hat{p}_{tis}$ or $\hat{\psi}_2$ appear, being in accordance with e.g. [**171**], and referring to Eq. (N.2).

C) The reasonability of applying mass-averaging to quantities with a pressure dimension can be justified on the basis of the Euler equation of turbomachines (Eqs. N.1, N.2), and the equation of angular momentum [Eq. (4.8)]. Multiplying Eq. (4.8) by the angular speed, and substituting the isentropic total pressure rise, specifies the mechanical power input necessary for driving the annular elementary cascade for obtaining the increase of total enthalpy:

$$dP = dM_z \omega = \left(2r\pi\, dr\, \rho\, \hat{v}_{z2}\right) u_2 \hat{v}_{u2} = dq_m \frac{1}{\rho}\Delta p_{tis} = dq_V \Delta p_{tis} \tag{K.3}$$

The above equation presents that the isentropic total pressure rise, as well as the static and dynamic pressures comprised by the total pressure, are to be determined as mass-averaged mean values, being representative for dP/dq_m.

D) Strictly speaking, when applying pitch-averaging to dynamic pressures, the velocity squares should be averaged. For example, $\overline{\left(v_{u2}^2\right)}$ should be included in Eq. (N.4), instead of $\left(\hat{v}_{u2}\right)^2$. However, this would mean that two types of pitch-averaging should be taken for v_{u2} within one equation (i.e. averaging of v_{u2} for the total pressure rise term $\eta_t u_2 \hat{v}_{u2}$, and averaging of v_{u2} squared for the dynamic pressure term, in Eq. (N.4)). In order to enable a simplified mathematical treatment, the *general integral mean value theorem* is applied herein, based on [**181**]. The theorem yields that

$$\overline{\left(v_{u2}^2\right)} = v_{u2}(\xi)\hat{v}_{u2} \tag{K.4a}$$

where ξ is a specific value of the pitchwise coordinate. With the assumption of $v_{u2}(\xi) \approx \hat{v}_{u2}$, Eq. (K.4a) implies the following approximation:

$$\overline{\left(v_{u2}^2\right)} \approx \left(\hat{v}_{u2}\right)^2 \tag{K.4b}$$

As a generalization, the pitch-average of any squared velocity component is approximated herein as the square of the pitch-average of the velocity component in point, i.e. $\overline{\left(v_{z2}^2\right)} \approx \left(\hat{v}_{z2}\right)^2$ etc. This approach is fully consistent with the common practice in CVD, e.g. [**38, 79**].

- ***Appendix L. Notes on the isentropic static pressure rise through a 2D cascade***

The expression for the circulation in Eq. (J.9) is re-formulated as follows:

$$\Gamma = s_{\mathrm{b}}\left(\hat{v}_{u1} - \hat{v}_{u2}\right) = s_{\mathrm{b}}\frac{\left(\hat{v}_{u1} - \hat{v}_{u2}\right)\left[\left(\hat{v}_{u1} + \hat{v}_{u2}\right)/2\right]}{\left(\hat{v}_{u1} + \hat{v}_{u2}\right)/2} = s_{\mathrm{b}}\left(\frac{\hat{v}_{u1}^2}{2} - \frac{\hat{v}_{u2}^2}{2}\right)\frac{1}{\left(\hat{v}_{u1} + \hat{v}_{u2}\right)/2} \quad \text{(L.1)}$$

It is considered that the inlet and outlet z-wise velocity components are equal for the 2D cascade. Therefore, the isentropic static pressure rise is determined only by the change of square of the pitchwise velocity component. The Bernoulli equation reads:

$$\Delta p_{\mathrm{is}} = \rho\left(\frac{\hat{v}_1^2}{2} - \frac{\hat{v}_2^2}{2}\right) = \rho\left(\frac{\hat{v}_{u1}^2}{2} - \frac{\hat{v}_{u2}^2}{2}\right) \quad \text{(L.2)}$$

Substituting Eq. (L.2) into Eq. (L.1) leads to the following relationship:

$$\Gamma = \Delta p_{\mathrm{is}}\, s_{\mathrm{b}}\,\frac{1}{\rho}\frac{1}{\left(\hat{v}_{u1} + \hat{v}_{u2}\right)/2} \quad \text{(L.3)}$$

The circulation can be expressed also on the basis of the Kutta-Joukowski theorem [**1**]:

$$\Gamma = \frac{dF_{\mathrm{L}}}{dr}\frac{1}{\rho\,\hat{v}_\infty} \quad \text{(L.4)}$$

Where dF_{L}/dr is the lift force per unit spanwise extension. The lift and drag forces, dF_{L} and dF_{D}, are the forces acting on the elementary blade section normal to and parallel with $\underline{\hat{v}}_\infty$, respectively. The lift and drag coefficients are defined as follows:

$$C_{\mathrm{L,D}} = \frac{dF_{\mathrm{L,D}}}{\left(c\,dr\right)\rho\,\hat{v}_\infty^2/2} \quad \text{(L.5)}$$

Therefore

$$\frac{dF_{\mathrm{L}}}{dr} = C_{\mathrm{L}}\,c\,\rho\frac{\hat{v}_\infty^2}{2} \quad \text{(L.6)}$$

Substituting Eq. (L.6) into Eq. (L.4) reads:

$$\Gamma = C_{\mathrm{L}}\,c\frac{\hat{v}_\infty}{2} \quad \text{(L.7)}$$

Making Eqs. (L.3) and (L.7) equal, considering that $\sin\alpha_\infty = \left(\hat{v}_{u1} + \hat{v}_{u2}\right)/2\,\hat{v}_\infty$ according to Eq. (J.10), and rearrangement, lead to Eq. (4.1).

• *Appendix M. Notes on Q2D and Q3D rotor approaches*

• *Q2D approach*

As discussed in the thesis, significant radial velocities may develop in a CVD rotor. However, in the Q2D CVD rotor approach, used e.g. in [**1, 37-38, 59, 72, 74, 79, 104**] – referring to Fig. J.1 and Table J.1 (Eqs. J.1b to J.8b) –, the radial flow is neglected (Eq. J.1b). In Q2D, stream tubes of constant middle radius along the z axis – termed herein as cylindrical stream tubes – are assumed through the rotor, with annular inlet and outlet sections dA_{s1} and dA_{s2}. Such fictitious stream tube is represented by the A_{sI} and A_{sII} surfaces in Fig. J.1b – although A_{sI} and A_{sII} are actually not stream surfaces, due to the presence of radial flow in reality. Still, it is assumed in the Q2D approach that the elementary annular cascade enclosed between A_{sI} and A_{sII} can be developed into a 2D cascade plane. Accordingly, the preliminary Q2D blade design relies on a 2D database selected by the designer. The radial flow leads to rearrangement of the axial velocity profile from inlet to outlet. Accordingly, the inlet and outlet axial velocities at dA_{s1} and dA_{s2} are inequal (Eq. J.3b).

In order to establish a connection to the 2D approach – conf. Eqs. J.2a to J.8a –, the following approximations are made herein. These approximations are accepted in Q2D CVD practice. i) The axial velocity through the blading – being constant for 2D flow – is represented by an inlet-to-outlet arithmetic mean value (Eq. J.4b). ii) As an approximation for the fulfilment of conservation of mass, $\hat{v}_{z12} r_{12} dr_{12} \approx \hat{v}_{z2} r_2 dr_2$ is taken into account (Eq. J.2b). iii) The pitchwise (tangential) momentum fluxes over A_{sI} and A_{sII} – being zero for 2D flow – are assumed to represent zero z-wise angular momentum about the axis of rotation (Eq. J.5b). iv) The pitchwise (tangential) shear forces over A_{sI} and A_{sII} – being zero for 2D flow – are assumed to represent zero torque about the axis of rotation (Eq. J.6b). v) The pitchwise (tangential) shear forces over dA_{s1} and dA_{s2} – neglected for 2D flow – are assumed to represent zero torque about the axis of rotation (Eq. J.8b).

The pitchwise (tangential) momentum fluxes over dA_{s1} and dA_{s2} represent the z-wise angular momentum about the axis of rotation – see also Table J.1 for Eq. J.7b – as expressed in the following relationship. Here, a swirl-free inlet ($v_{u1} \equiv 0$) as well as $dA_{s2} = N_b\, s_{b2}\, dr = 2\, r_2\, \pi\, dr$ are considered.

$$\left[\int_{dA_{s1}, dA_{s2}} \underline{r} \times \left[\underline{v}\rho\left(\underline{v}\, d\,\underline{A}_s\right)\right]\right]_u = -\int_{dA_{s2}} r\, v_u \rho\left(v_z dr\, ds_b\right) = -r_2\, \hat{v}_{u2} \rho\, \hat{v}_{z2}\left(N_b s_b dr_2\right) = -2 r_2^2 \pi\, dr_2\, \rho\, \hat{v}_{z2} \hat{v}_{u2} \qquad \text{(J.7b)}$$

Taking Eq. (J.9) as a basis, but considering the relative pitchwise velocities, and applying $\hat{w}_{ui} = u - \hat{v}_{ui}$ (see the velocity vector diagram in Fig. 2.2), the blade circulation for swirl-free inlet is

$$\Gamma \approx s_b\left(\hat{w}_{u1} - \hat{w}_{u2}\right) = s_b \hat{v}_{u2} = \frac{2r\pi}{N_b} \hat{v}_{u2} = \frac{2\pi}{N_b \omega\rho} \rho u \hat{v}_{u2} = \frac{2\pi}{N_b \omega\rho} \Delta p_{t\,is} \qquad \text{(M.1)}$$

manifesting that the spanwise increasing isentropic total pressure rise prescribed in CVD corresponds to spanwise increasing blade circulation as well.

- ***Q3D approach***

Fig. J.1 and Table J.1 (Eqs. J.1c to J.8c) are referred to.

The radial flow is approximated through the blade passage as $v_r \approx \hat{v}_{z12} \tan\beta$, Eq. (J.1c), for which the mean axial velocity is taken as presented in Eqs. (J.2c) to (J.4c).

Since the neglects in Eqs. (J.5b), (J.6b) and (J.8b) in Table J.1 are accepted in the Q2D approach, they are adapted herein to the Q3D approach as well [Eqs. (J.5c), (J.6c), and (J.8c), respectively]. The mass conservation and momentum considerations for Q2D approach in Eqs. (J.2b) and (J.7b) apply for the Q3D approach as well [Eqs. (J.2c) and (J.7c)].

The z-wise component equation of the angular momentum equation applied to the control volume in the absolute frame of reference takes the form presented in Eq. (4.8), for both Q2D and Q3D approach, with the following considerations. i) Although the flow is unsteady in the absolute frame, according to the rotating blade passages, this periodic unsteadiness does not affect the z-wise angular moments and torques. ii) Eqs. (J.5b) to (J.8b) for the Q2D approach, as well as Eqs. (J.5c) to (J.8c) for the Q3D approach, are taken into account (Table J.1). iii) The force fields acting inside the control volume as well as the pressure-related forces acting on the control volume surfaces do not express any torque about the z axis.

- ***Appendix N. Approximation of the outlet axial velocity distribution; integral conditions for the $\hat{\psi}_2(R_2)$ and $\hat{\varphi}_2(R_2)$ distributions***

Let us select two points, 1 and 2, located at *arbitrary* radii r_1 and r_2 upstream and downstream of the rotor blading, respectively. Applying the Bernoulli equation in the relative (rotating) frame of reference, along an arbitrary line in a blade passage connecting the two points, yields the Euler equation of turbomachines (e.g. [**1, 143**]). The following considerations and assumptions are made. i) Isentropic, incompressible flow is present. ii) The flow is steady in the rotating frame. iii) The fluid is sucked from an irrotational, swirl-free upstream flow field. iv) Gravity effects are neglected. The result is

$$\left(p_2 + \rho\frac{v_2^2}{2}\right)_{\text{is}} - \left(p_1 + \rho\frac{v_1^2}{2}\right) = \rho u_2 v_{u2} \tag{N.1}$$

Taking pitchwise mass-averaging (referring to Eq. K.2) at the radii r_1 and r_2 related to points 1 and 2, yields

$$\hat{p}_{\text{tis}2} - \hat{p}_{\text{t}1} = \Delta p_{\text{tis}} = \rho u_2 \hat{v}_{u2} \tag{N.2}$$

Since radii r_1 and r_2 were selected arbitrarily, they are independent variables. As Eq. (N.2) demonstrates, the isentropic total pressure rise at location 2 depends on the *outlet* characteristics only. Rearranging, and differentiating with respect to r_1 yields

$$\frac{\partial}{\partial r_1}\left[\hat{p}_{\mathrm{tis}\,2}(r_2)\right]-\frac{\partial}{\partial r_1}\left[\Delta p_{\mathrm{tis}}(r_2)\right]\equiv 0=\frac{\partial \hat{p}_{\mathrm{t}1}}{\partial r_1} \qquad \text{(N.3)}$$

On this basis, $\hat{p}_{\mathrm{t}1}$ is taken to be constant along the radius.

The Bernoulli equation extended with the total pressure loss term is applied between points 1 and 2 in the rotating frame. Then, the velocities are transformed from relative ones to absolute ones, using $\underline{v} = \underline{w} + \underline{u}$. The result is, after pitch-averaging at the inlet and outlet radii, as follows.

$$\frac{\hat{p}_{\mathrm{t}1}}{\rho}+\eta_{\mathrm{t}} u_2\,\hat{v}_{u2}\approx\frac{\hat{p}_2}{\rho}+\frac{(\hat{v}_{u2})^2}{2}+\frac{(\hat{v}_{z2})^2}{2} \qquad \text{(N.4)}$$

In the above equation, the real total pressure rise has been expressed as $\Delta p_{\mathrm{t}} = \eta_{\mathrm{t}}\,\Delta p_{\mathrm{t\,is}}$, where the isentropic total pressure rise is to be expressed using Eq. (N.2). Furthermore, the kinetic energy related to the outlet radial velocity has been neglected in comparison to that related to the other outlet velocity components. The local total efficiency, defined in Eq. (F.2) and applied in Eq. (N.4), η_{t}, is often used for local characterisation of blade energetics, e.g. in [**38, 52-53, 122, 164**], for both free vortex-designed and CVD rotors.

Derivation of Eq. (N.4) with respect to r_2 reads

$$\eta_{\mathrm{t}}\left(\omega\hat{v}_{u2}+u_2\frac{d\hat{v}_{u2}}{dr_2}\right)=\frac{1}{\rho}\frac{d\hat{p}_2}{dr_2}+\hat{v}_{u2}\frac{d\hat{v}_{u2}}{dr_2}+\frac{1}{2}\frac{d\left[(\hat{v}_{z2})^2\right]}{dr_2} \qquad \text{(N.5)}$$

The spanwise gradient of static pressure at the outlet is expressed as follows, using the spanwise component of the Euler equation in a cylindrical coordinate system. This approach is supported by, e.g., [**1, 38, 59**] and Eq. (C.1).

$$\frac{1}{\rho}\frac{d\hat{p}_2}{dr_2}=\frac{(\hat{v}_{u2})^2}{r_2} \qquad \text{(N.6)}$$

Substituting Eq. (N.6) into Eq. (N.5), rearrangement, and non-dimensioning yield Eq. (4.9).

The initially unknown $\hat{\psi}_2(\nu_{\mathrm{ht}})$ and $\hat{\varphi}_2(\nu_{\mathrm{ht}})$ conditions must be set in such a way that the $\hat{\psi}_2(R_2)$ and $\hat{\varphi}_2(R_2)$ distributions, specified by Eqs. (4.10) and (4.9), fulfil the following integral conditions.

Global continuity:

$$q_{\mathrm{V}}=2\pi\int_{r_{\mathrm{h}}}^{r_{\mathrm{t}}}\hat{v}_{z2}\,r_2\,dr_2 \qquad \text{(N.7a)}$$

In dimensionless form:

$$\Phi = \frac{2}{1-\nu_{\mathrm{ht}}^2} \int_{\nu_{\mathrm{ht}}}^{1} \hat{\varphi}_2 \, R_2 \, dR_2 \tag{N.7b}$$

Global aerodynamic performance:

$$\overline{\Delta p_{\mathrm{t\,is}}} \, q_{\mathrm{V}} = \frac{\overline{\Delta p_{\mathrm{t}}}}{\overline{\eta}_{\mathrm{t}}} q_{\mathrm{V}} = \int_{r_{\mathrm{h}}}^{r_{\mathrm{t}}} \Delta p_{\mathrm{t\,is}} \, dq_{\mathrm{V}} = \int_{r_{\mathrm{h}}}^{r_{\mathrm{t}}} \left(\rho u_2 \, \hat{v}_{u2}\right)\left(2\pi \hat{v}_{z2} \, r_2 \, dr_2\right) \tag{N.8a}$$

In dimensionless form:

$$\frac{\Psi \, \Phi}{\overline{\eta}_{\mathrm{t}}} = \frac{2}{1-\nu_{\mathrm{ht}}^2} \int_{\nu_{\mathrm{ht}}}^{1} \hat{\psi}_2 \, \hat{\varphi}_2 \, R_2 \, dR_2 \tag{N.8b}$$

The global total efficiency used in Eqs. (N.8a) and (N.8b) is defined principally as follows:

$$\overline{\eta}_{\mathrm{t}} = \frac{\overline{\Delta p_{\mathrm{t}}} \, q_{\mathrm{V}}}{M \, \omega} \tag{N.9}$$

Where $\overline{\Delta p_{\mathrm{t}}} \, q_{\mathrm{V}}$ is the global aerodynamic performance and $M \, \omega$ is the rotor shaft mechanical power input, e.g. [**74**]. However, the volumetric efficiency is taken herein as unity, as a reasonable approximation, and the global total efficiency is therefore approximated as the ratio between the realized and isentropic total pressure rise values, being mass-averaged in the annulus:

$$\overline{\eta}_{\mathrm{t}} \approx \frac{\overline{\Delta p_{\mathrm{t}}}}{\overline{\Delta p_{\mathrm{t\,is}}}} \tag{N.10}$$

- ***Appendix P. Formulae based on the Q2D rotor approach***

Flow angles [conf. Eqs. (4.11a), (4.11b)]:

$$\alpha_{1\,\mathrm{Q2D}} = \tan^{-1}\left(\frac{R_{1\,\mathrm{Q2D}}}{\hat{\varphi}_{12\,\mathrm{Q2D}}}\right) \tag{P.1a}$$

$$\alpha_{2\,\mathrm{Q2D}} = \tan^{-1}\left(\frac{R_{2\,\mathrm{Q2D}} - \hat{\psi}_{2\,\mathrm{Q2D}} / 2R_{2\,\mathrm{Q2D}}}{\hat{\varphi}_{12\,\mathrm{Q2D}}}\right) \tag{P.1b}$$

Free-stream relative velocity [conf. Eq. (4.12)]:

$$\left(w_\infty / u_{\mathrm{t}}\right)_{\mathrm{Q2D}} = \left\{\hat{\varphi}_{12\,\mathrm{Q2D}}^2 + \left[R_{12} - \hat{\psi}_{2\,\mathrm{Q2D}} / \left(4R_{2\,\mathrm{Q2D}}\right)\right]^2\right\}^{1/2} \tag{P.2}$$

Free-stream flow angle [conf. Eq. (4.13)]:

$$\alpha_{\infty\,\mathrm{Q2D}} = \cos^{-1}\left[\frac{\hat{\varphi}_{12\,\mathrm{Q2D}}}{\left(w_\infty / u_{\mathrm{t}}\right)_{\mathrm{Q2D}}}\right] \tag{P.3}$$

Fundamental cascade equation:

$$C_{\mathrm{L\,Q2D}}\left(\frac{c}{s_{\mathrm{b\,12}}}\right)_{\mathrm{Q2D}}=\frac{2\,\hat{v}_{u2\,\mathrm{Q2D}}}{w_{\infty\,\mathrm{Q2D}}} \tag{P.4a}$$

In dimensionless form:

$$C_{\mathrm{L\,Q2D}}\left(\frac{c}{s_{\mathrm{b\,12}}}\right)_{\mathrm{Q2D}}=\frac{\hat{\psi}_{2\,\mathrm{Q2D}}/R_{2\,\mathrm{Q2D}}}{\left\{\hat{\varphi}_{12\,\mathrm{Q2D}}^{2}+\left[R_{12}-\hat{\psi}_{2\,\mathrm{Q2D}}/\left(4R_{2\,\mathrm{Q2D}}\right)\right]^{2}\right\}} \tag{P.4b}$$

- ***Appendix Q. Comparison of diffusion in Q3D and Q2D approaches***

The ratio of outlet and inlet relative velocities can be expressed as

$$\frac{\hat{w}_2}{\hat{w}_1}=1-\frac{\Delta\hat{w}}{\hat{w}_1} \tag{Q.1}$$

Therefore, justification of

$$\left(\frac{\Delta\hat{w}}{\hat{w}_1}\right)_{\mathrm{Q3D}}<\left(\frac{\Delta\hat{w}}{\hat{w}_1}\right)_{\mathrm{Q2D}} \tag{Q.2}$$

implies the validity of relationship (4.17b). As shown in **Figure Q.1**, the change in tangential relative velocity through the cascade is

$$\frac{\Delta\hat{w}_u}{u_{\mathrm{t}}}=R_1-\left(R_2-\frac{\hat{\psi}_2}{2R_2}\right)=\frac{\hat{\psi}_2}{2R_2}-\left(R_2-R_1\right) \tag{Q.3}$$

For moderate flow deflection, as a brief approximation (see the figure),

$$\frac{\Delta\hat{w}}{u_{\mathrm{t}}}\approx\frac{\Delta\hat{w}_u}{u_{\mathrm{t}}}\sin\alpha_1=\frac{\Delta\hat{w}_u}{u_{\mathrm{t}}}\frac{R_1}{\hat{w}_1/u_{\mathrm{t}}} \tag{Q.4}$$

is applied. Substituting Eq. (Q.3) into Eq. (Q.4), and considering $\left(\hat{w}_1/u_{\mathrm{t}}\right)^2=\hat{\varphi}_{12}^2+R_1^2$, yields

$$\frac{\Delta\hat{w}}{\hat{w}_1}=\underbrace{\frac{1}{\left(\hat{\varphi}_{12}/R_1\right)^2+1}}_{I}\left[\underbrace{\frac{\hat{\psi}_2}{2R_1R_2}}_{II}\quad\underbrace{-\left(\frac{R_2}{R_1}-1\right)}_{III}\right] \tag{Q.5}$$

In what follows, terms I to III marked in Eq. (Q.5) are discussed.

Term I. $R_{1\,\mathrm{Q3D}} < R_{1\,\mathrm{Q2D}}$ ($=R_{12}$). The axial velocity at the outlet increases with span in CVD, on the basis of Eq. (4.9), as far as $\eta_{\mathrm{t}}>\hat{\psi}_2/2R_2^2$, being valid for most applications. This means that $\hat{\varphi}_{2\,\mathrm{Q3D}}>\hat{\varphi}_{2\,\mathrm{Q2D}}$, since $R_{2\,\mathrm{Q3D}}>R_{2\,\mathrm{Q2D}}$ ($=R_{12}$). Furthermore, at the inlet, the axial velocity usually decreases with radius, due to streamline curvature affected by the inlet nose cone, e.g. [**26, 131**]. This results in $\hat{\varphi}_{1\,\mathrm{Q3D}}>\hat{\varphi}_{1\,\mathrm{Q2D}}$, since $R_{1\,\mathrm{Q3D}}<R_{1\,\mathrm{Q2D}}$. As a consequence of the aforementioned trends,

considering Eqs. (J.4b) and (J.4c) in Table J.1, $\hat{\varphi}_{12\,\mathrm{Q3D}} > \hat{\varphi}_{12\,\mathrm{Q2D}}$ is valid. $R_{1\mathrm{Q3D}} < R_{1\mathrm{Q2D}}$ and $\hat{\varphi}_{12\,\mathrm{Q3D}} > \hat{\varphi}_{12\,\mathrm{Q2D}}$ imply that Term I is smaller for the Q3D approach, supporting the trend (Q.2).

Term II. The ratio of this term for the Q3D and Q2D approaches can be written as follows, considering Eq. (4.10),

$$\frac{\left(\hat{\psi}_2/2R_1R_2\right)_{\mathrm{Q3D}}}{\left(\hat{\psi}_2/2R_1R_2\right)_{\mathrm{Q2D}}} = \left(\frac{R_{2\,\mathrm{Q3D}}}{R_{2\,\mathrm{Q2D}}}\right)^{m-1} \left(\frac{R_{1\,\mathrm{Q2D}}}{R_{1\,\mathrm{Q3D}}}\right) \tag{Q.6a}$$

Here, it has been taken into account that $\hat{\psi}_2(\nu_{\mathrm{ht}})$ and ν_{ht}^m are equal in design for the Q2D and Q3D approaches.

By substituting $R_{1\,\mathrm{Q3D}} = R_{12} - \Delta R$ and $R_{2\,\mathrm{Q3D}} = R_{12} + \Delta R$, and considering that $\Delta R << R_{12}$, it can be pointed out that $R_{1\,\mathrm{Q2D}}/R_{1\,\mathrm{Q3D}} \approx R_{2\,\mathrm{Q3D}}/R_{2\,\mathrm{Q2D}}$. Therefore, Eq. (Q.6a) can be written as

$$\frac{\left(\hat{\psi}_2/2R_1R_2\right)_{\mathrm{Q3D}}}{\left(\hat{\psi}_2/2R_1R_2\right)_{\mathrm{Q2D}}} \approx \left(\frac{R_{2\,\mathrm{Q3D}}}{R_{2\,\mathrm{Q2D}}}\right)^{m} \tag{Q.6b}$$

Since $R_{2\,\mathrm{Q3D}}/R_{2\,\mathrm{Q2D}} > 1$, and $m > 0$ for CVD, this ratio is always positive, acting against the trend (Q.2). However, as pointed out in the example at the end of this Appendix, the trends related to Terms I and III, supporting trend (Q.2), dominate. The trends related to Terms I to III, supporting or acting against trend (Q.2), and eventually, the validity of relationship (4.17a), are to be analysed in each particular design assignment.

Term III. This term is zero in the Q2D approach ($R_{1\,\mathrm{Q2D}} = R_{2\,\mathrm{Q2D}} = R_{12}$), and is negative in the Q3D approach ($R_{2\,\mathrm{Q3D}} > R_{1\,\mathrm{Q3D}}$), supporting the trend (Q.2).

Design case study. For the design case study presented in Section 4.5, data summarized in **Table Q.1** are characteristic in the region of midspan radius $R_{12} = 0.838$. The data demonstrate that the trends related to Terms I and III dominate.

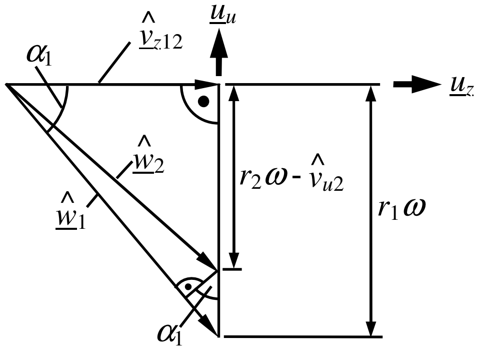

Figure Q.1. *Sketch for explanation of diffusion*

Table Q.1. *Data related to Eq. (Q.5) in the design example*

R_{12}	$R_{1\ Q3D}$	$R_{2\ Q3D}$	$\hat{\varphi}_1$	$[\hat{\varphi}_2(R_2)]_{Q3D}$	$[\hat{\varphi}_2(R_2)]_{Q2D}$	$[\hat{\psi}_2(R_2)]_{Q3D}$	$[\hat{\psi}_2(R_2)]_{Q2D}$
0.838	0.818	0.858	0.500	0.538	0.530	0.615	0.594

	Term I	Term II	Term III	Term II + Term III	$\Delta\hat{w}/\hat{w}_1$
Q3D	0.713	0.438	-0.049	0.389	0.278
Q2D	0.726	0.423	0	0.423	0.307
Ratio $()_{Q3D}/()_{Q2D}$	0.982	1.036	-	0.920	0.904

- ***Appendix R. Research projects related to the thesis work***

Domestic research projects:

- The work relates to the scientific programme of the project "Development of a quality-oriented and harmonized R+D+I strategy and the functional model at BME". The New Széchenyi Plan (Project ID: TÁMOP-4.2.1/B-09/1/KMR-2010-0002) supports this project.
- Concerted investigation of aerodynamic and noise generation mechanisms in highly-loaded axial flow rotor blade rows (Fokozott terhelésű axiális átömlésű járókerék-lapátrácsok aerodinamikai és zajkeltési mechanizmusainak együttes vizsgálata) OTKA (K 83807) – 2011-2013 (principal investigator: János VAD)
- Multi-objective optimisation of axial flow turbomachines of high specific performance. (Fokozott fajlagos teljesítményű axiális átömlésű forgógépek többcélú optimalizálása) OTKA (K 63704) – 2006-2010 (principal investigator: János VAD)
- Development of advanced design methodology for axial flow turbomachinery, with consideration of 3D flow, applying simulation and experimental means. (Axiális átömlésű áramlástechnikai forgógépek korszerű tervezési módszerének kidolgozása a háromdimenziós áramlás figyelembevételével, szimulációs és kísérleti eszközök alkalmazásával) OTKA (T 043493) – 2003-2005 (principal investigator: Ferenc BENCZE)
- Refinement of design methodology and improvement of behaviour from the viewpoint of energetics for axial flow turbomachines. (Axiális átömlésű forgógépek tervezési módszerének pontosítása és energetikai tulajdonságának javítása) OM FKFP (0356/99) – 1999-2001 (principal investigator: Tamás LAJOS)
- Measurement of velocity field and refinement of design method for axial flow turbomachines. (Axiális átömlésű ventilátorok sebességterének mérése és méretezési eljárásának pontosítása) OTKA (T 025361) – 1998-2001 (principal investigator: Ferenc BENCZE)

International research projects:

- Theoretical, numerical and experimental investigation of harmonisation of spanwise distributions of blade sweep angle and blade circulation in design of axial flow turbomachinery rotors. Austrian-Hungarian S&T (TéT) (A-15/03) – 2004-2005 (Austrian / Hungarian principal investigators: H. Jaberg / J.Vad)
- Comparative theoretical, numerical and experimental investigation of axial flow turbomachinery rotors, designed with different optimisation concepts incorporating blade sweep. Austrian-Hungarian S&T (TéT) (A-10/01) – 2002-2003 (Austrian / Hungarian principal investigators: H. Jaberg / J. Vad)
- Comparative fluid mechanical investigation of radial and axial flow turbomachinery under design and off-design circumstances. German-Hungarian S&T (TéT) (D-37/99) – 2000-2001 (German / Hungarian principal investigators: E. Pap / F. Bencze)
- Comparison of three-dimensional flow fields developing in axial flow turbomachines of free vortex and non-free vortex operation. Austrian-Hungarian S&T (TéT) (A-34/98) – 1999-2000 (Austrian / Hungarian principal investigators: H. Jaberg / F. Bencze)
- Investigation of aerodynamic and energetic characteristics of axial flow fans for the improvement of fan design methodology – a concerted application of Laser Doppler Anemometry (LDA) and Computational Fluid Dynamics (CFD). Italian-Hungarian S&T (TéT) (I-28/98) – 1998-2000 (Italian / Hungarian principal investigators: F. Rispoli / F. Bencze)